A&A 557, A131 (2013)
DOI: 10.1051/0004-6361/201321390

Astronomy & Astrophysics

The DiskMass Survey

VII. The distribution of luminous and dark matter in spiral galaxies⋆

Thomas P. K. Martinsson[1,2], Marc A. W. Verheijen[1], Kyle B. Westfall[1,⋆⋆], Matthew A. Bershady[3], David R. Andersen[4], and Rob A. Swaters[5]

[1] Kapteyn Astronomical Institute, University of Groningen, PO Box 800, 9700 AV Groningen, The Netherlands
e-mail: [verheyen;westfall]@astro.rug.nl
[2] Leiden Observatory, Leiden University, PO Box 9513, 2300 RA Leiden, The Netherlands
e-mail: martinsson@strw.leidenuniv.nl
[3] Department of Astronomy, University of Wisconsin, 475 N. Charter St., Madison, WI 53706, USA
e-mail: mab@astro.wisc.edu
[4] NRC Herzberg Institute of Astrophysics, 5071 West Saanich Road, Victoria, British Columbia, Canada V9E 2E7, Canada
e-mail: david.andersen@nrc-cnrc.gc.ca
[5] National Optical Astronomy Observatory, 950 North Cherry Ave., Tucson, AZ 85719, USA
e-mail: swaters@noao.edu

Received 1 March 2013 / Accepted 12 July 2013

ABSTRACT

We present dynamically-determined rotation-curve mass decompositions of 30 spiral galaxies, which were carried out to test the maximum-disk hypothesis and to quantify properties of their dark-matter halos. We used measured vertical velocity dispersions of the disk stars to calculate dynamical mass surface densities ($\Sigma_{\rm dyn}$). By subtracting our observed atomic and inferred molecular gas mass surface densities from $\Sigma_{\rm dyn}$, we derived the stellar mass surface densities (Σ_*), and thus have absolute measurements of all dominant baryonic components of the galaxies. Using K-band surface brightness profiles (I_K), we calculated the K-band mass-to-light ratio of the stellar disks ($\Upsilon_* = \Sigma_*/I_K$) and adopted the radial mean ($\overline{\Upsilon_*}$) for each galaxy to extrapolate Σ_* beyond the outermost kinematic measurement. The derived $\overline{\Upsilon_*}$ of individual galaxies are consistent with all galaxies in the sample having equal Υ_*. We find a sample average and scatter of $\langle\overline{\Upsilon_*}\rangle = 0.31 \pm 0.07$. Rotation curves of the baryonic components were calculated from their deprojected mass surface densities. These were used with circular-speed measurements to derive the structural parameters of the dark-matter halos, modeled as either a pseudo-isothermal sphere (pISO) or a Navarro-Frenk-White (NFW) halo. In addition to our dynamically determined mass decompositions, we also performed alternative rotation-curve decompositions by adopting the traditional maximum-disk hypothesis. However, the galaxies in our sample are submaximal, such that at 2.2 disk scale lengths (h_R) the ratios between the baryonic and total rotation curves ($\mathcal{F}_{\rm b}^{2.2h_R}$) are less than 0.75. We find this ratio to be nearly constant between 1–6h_R within individual galaxies. We find a sample average and scatter of $\langle\mathcal{F}_{\rm b}^{2.2h_R}\rangle = 0.57 \pm 0.07$, with trends of larger $\mathcal{F}_{\rm b}^{2.2h_R}$ for more luminous and higher-surface-brightness galaxies. To enforce these being maximal, we need to scale Υ_* by a factor 3.6 on average. In general, the dark-matter rotation curves are marginally better fit by a pISO than by an NFW halo. For the nominal-Υ_* (submaximal) case, we find that the derived NFW-halo parameters have values consistent with ΛCDM N-body simulations, suggesting that the baryonic matter in our sample of galaxies has only had a minor effect on the dark-matter distribution. In contrast, maximum-Υ_* decompositions yield halo-concentration parameters that are too low compared to the ΛCDM simulations.

Key words. techniques: imaging spectroscopy – galaxies: spiral – galaxies: structure – galaxies: kinematics and dynamics – galaxies: fundamental parameters

1. Introduction

For a spiral galaxy, it should be possible to derive the mass distributions of the different components by decomposing its observed rotation curve into separate contributions from the various baryonic components and a dark-matter halo. However, even though it has now been shown that a more or less flat rotation curve seems to be a general feature of spiral galaxies (e.g., Bosma 1978, 1981a,b; Begeman 1987, 1989; Sofue et al. 1999; Sofue & Rubin 2001), and although the concept of a dark-matter halo is well established and widely accepted[1], there is still a huge uncertainty in the observationally inferred distribution of the dark matter. The main issue is that, since the stellar mass is unknown, the technique of decomposing the observed rotation curve does not put a strong constraint on the detailed shape of the dark-matter-halo density profile. In many cases the observed rotation curve can even be explained by a two-parameter dark-matter-halo model alone, with the disk containing no stellar mass at all. The most commonly used approach to circumvent

⋆ Appendix is available in electronic form at http://www.aanda.org
⋆⋆ National Science Foundation (USA) International Research Fellow.

[1] Here and throughout this work we assume that the Newtonian gravitational theory holds. However, suggestions have been made that Newtonian dynamics need modification for use at low accelerations (e.g., Milgrom 1983; Begeman et al. 1991; Sanders 1996; Sanders & Verheijen 1998).

this problem has been to go to the other extreme by assuming a maximum contribution from the baryons, thereby increasing the mass-to-light ratio of the stellar component (Υ_*) until the rotation curve of the baryons approximates the amplitude of the observed rotation curve in the inner region (the "maximum-disk hypothesis"; van Albada & Sancisi 1986). This approach sets an upper limit on the contribution from the baryons, but without knowledge of Υ_* there is still a severe disk-halo degeneracy, making it impossible to determine the structural properties of the dark-matter halo.

Another approach is to use Υ_* derived from stellar-population-synthesis models; however, these models suffer from large uncertainties since they require many assumptions regarding the star-formation and chemical-enrichment history, the initial mass function (IMF), and accurate accounting for late phases of stellar evolution (Maraston 2005; Conroy et al. 2009). For example, although Kauffmann et al. (2003) find random errors of only 40% from the models, the choice of IMF alone results in a factor of two systematic uncertainty in the stellar mass.

While the maximum-disk hypothesis has been a commonly used refuge in the literature (e.g., van Albada et al. 1985; Kent 1986; Broeils & Courteau 1997), there is evidence that at least some galaxy disks are in fact submaximal, e.g., based on the lack of a surface-brightness dependency in the Tully-Fisher relation (TF; Tully & Fisher 1977) for a wide range of spirals (Zwaan et al. 1995; Courteau & Rix 1999; Courteau et al. 2003). However, observations have so far not lead to a consensus, and the maximality may depend on the galaxy type (Bottema 1993; Weiner et al. 2001; Kranz et al. 2003; Kregel et al. 2005; Byrd et al. 2006; Herrmann & Ciardullo 2009; Dutton et al. 2011, 2013; Barnabè et al. 2012).

One of the main goals of the DiskMass Survey (DMS; Bershady et al. 2010a, hereafter Paper I) is to break the disk-halo degeneracy using stellar and gas kinematics to determine the dynamical mass-to-light ratio of the galaxy disk ($\Upsilon_{\rm dyn}$). For a locally isothermal disk

$$\Upsilon_{\rm dyn} = \frac{\Sigma_{\rm dyn}}{I} = \frac{\sigma_z^2}{\pi G k h_z I}, \quad (1)$$

where $\Sigma_{\rm dyn}$ is the dynamical mass surface density of the disk, I the surface brightness, σ_z the vertical component of the stellar velocity dispersion, G the gravitational constant, k a parameter dependent on the vertical mass distribution, and h_z the disk scale height (van der Kruit & Searle 1981; Bahcall & Casertano 1984). Since I is well known from photometry, and the relation between h_z and the disk scale length (h_R) has been statistically determined from studies of edge-on spiral galaxies (e.g., de Grijs & van der Kruit 1996; Kregel et al. 2002, see also the compilation in Fig. 1 of Bershady et al. 2010b, hereafter Paper II), observations of σ_z give us a direct estimate of $\Upsilon_{\rm dyn}$. The value of k is expected to range between 1.5 to 2 (exponential to isothermal distribution; van der Kruit 1988). In this paper, we will assume an exponential distribution ($k = 1.5$) as a reasonable approximation for the composite (gas+stars) density distribution (Paper II). In the expected range of density distributions discussed by van der Kruit (1988), our adopted value of k will effectively maximize the measurement of $\Sigma_{\rm dyn}$ and $\Upsilon_{\rm dyn}$.

The strategy of measuring the stellar velocity dispersion to obtain the dynamical mass surface density has been attempted before (van der Kruit & Freeman 1984, 1986; Bottema 1993; Kregel et al. 2005). These studies showed that the ratio of the maximum amplitude of the disk's rotation curve (calculated from the observed velocity dispersion) and the maximum of the observed rotation speed ($V_{\rm max}$) was much lower than expected for a maximum disk. Bottema (1993) found that disks contribute only 63 ± 10% to the observed rotation speed. Kregel et al. (2005) found an even smaller average disk contribution of 58 ± 5%, with a 1σ scatter of 18% when including two outliers. Excluding the outliers, they find an average disk contribution of 53 ± 4%, with a 1σ scatter of 15%. These results are significantly lower than the 85 ± 10% which is typical for a maximum-disk case (Sackett 1997). In Bershady et al. (2011, hereafter Paper V), we followed the approach of using the relation between the central σ_z of the disk and $V_{\rm max}$, and found that disks contribute only 47 ± 8% of the observed rotation speed; even lower than what was found by the earlier studies, but consistent within the errors. We also found that the disk contribution depends on color, absolute K-band magnitude, and $V_{\rm max}$, such that redder, more luminous, and faster-rotating galaxies have baryonic disks that make a relatively larger contribution to their observed rotation speeds.

With a measured distribution of the baryonic mass, together with the observed rotation speed, it is possible to derive the density distribution of the dark matter. While the flatness of the outer part of rotation curves suggests a halo with a dark-matter density distribution declining as $\rho \propto R^{-2}$, the inner slope is still debated (see, e.g., de Blok 2010). The difficulty in determining the inner density distribution of the dark matter arises mainly due the uncertainty in the baryonic mass distribution. From numerical N-body simulations (e.g., Navarro et al. 1997) the inner density profiles and concentrations of the dark-matter halos are predicted in the absence of baryons. It is argued that the baryons in the disk will tend to contract the halo while it is forming (e.g., Blumenthal et al. 1986; Gnedin et al. 2004). However, several processes may occur that could also expand the halo, such as dynamical friction between the halo and infalling galaxies (e.g., El-Zant et al. 2001), or mass outflows from central starbursts and active galactic nuclei (Read & Gilmore 2005; Governato et al. 2012; Pontzen & Governato 2012).

In this paper, we decompose the rotation curves of 30 spiral galaxies, using stellar kinematics from PPak (Verheijen et al. 2004; Kelz et al. 2006) and ionized gas kinematics from SparsePak (Bershady et al. 2004, 2005), as well as 21-cm radio synthesis data from the WSRT, GMRT and VLA, near-infrared (NIR) photometry from the Two-Micron All-Sky Survey (2MASS; Skrutskie et al. 2006) and MIPS 24-μm imaging from the *Spitzer* Space Telescope. The paper is organized in the following way: Sect. 2 describes the sample and summarizes the used data. In Sect. 3, we derive mass surface densities of the atomic and molecular gas, and show how our stellar kinematic measurements from PPak (Martinsson et al. 2013, hereafter Paper VI) provide mass surface densities of the stars. We further investigate relative mass fractions of the baryons. In Sect. 4 the observed HI+Hα rotation curves are combined. In Sect. 5 we calculate the baryonic rotation curves, derive measured dark-matter rotation curves and fit a pseudo-isothermal sphere or a NFW halo to these rotation curves. We also perform alternative rotation-curve decompositions, using maximum-Υ_* solutions. From the observed HI+Hα rotation curves and the calculated baryonic rotation curves, we derive the baryonic mass fractions as a function of radius and quantify the baryonic maximality in Sect. 6. In Sect. 7 we investigate how well the measured dark-matter rotation curves are fitted, and compare the NFW parameters with results from numerical N-body simulations. Section 8 contains a discussion on what we have found in this work, which is finally summarized in Sect. 9. Throughout this paper we adopt the Hubble parameter $H_0 = 73$ km s^{-1} Mpc^{-1}.

2. Observational data

The data used in this paper are presented in more detail elsewhere. The following subsections briefly summarize these data.

2.1. Galaxy sample

The complete DMS sample is described in Paper I. Here, we use the subsample of 30 galaxies observed with the PPak IFU (Paper VI)[2]. We refer to these galaxies as the PPak sample. Observed properties of the galaxies in the PPak sample, such as distances, colors, coordinates and disk orientations, can be found in Tables 1 and 5 of Paper VI. In summary, these galaxies cover a range in morphological type from Sa to Im with 22 galaxies being Sc or later; absolute K-magnitudes (M_K) range from –21.0 to –25.4; $B-K$ colors are between 2.7 and 4.2; and the central disk face-on K-band surface brightness ($\mu^i_{0,K}$) ranges from 19.9 to 16.0 mag arcsec^{-2}. The galaxies have been selected to be close to face-on, and cover a range in inclination from 6° to 45°.

2.2. Near-infrared photometry

A description of our re-analysis of 2MASS NIR photometry of the galaxies in our sample is presented in Paper VI. These data were used to produce pseudo-K-band surface brightness profiles, $\mu_K(R)$, derived by combining J-, H- and K-band images. The bulge/disk decomposition and the corrections to the bulge and disk surface brightness (face-on, Galactic-extinction, and k-corrections) resulted in corrected bulge ($\mu_{K,\rm bulge}$) and disk ($\mu^i_{K,\rm disk}$) radial surface brightness profiles. We defined the bulge radius ($R_{\rm bulge}$) to be the radius where the light from the bulge contributes 10% to the light at that radius. The NIR surface brightness will be used to trace the stellar mass of the galaxy (Sect. 3).

As described in Paper VI, we have derived h_R in an iterative way, fitting an exponential function to the observed K-band surface brightness profile between 1–4h_R. Using Eq. (1) in Paper II, we calculate h_z from h_R with a systematic error of 25%. The derived h_z is used for our conversion from σ_z to $\Sigma_{\rm dyn}$ (Eq. (1)). Table 1 contains the derived h_R and h_z for each target galaxy. Other derived parameters, such as the fitted scale length in arcsec, central face-on-corrected surface brightness of the disk ($\mu^i_{0,K}$), bulge-to-disk ratio (B/D), and the absolute K-band magnitude (M_K), are tabulated in Tables 1 and 5 of Paper VI.

2.3. Stellar and ionized-gas kinematics

Paper VI also presented the reduction and analysis of the stellar and ionized-gas ([OIII]λ5007 Å) kinematics from optical spectroscopy taken with PPak, where the stellar kinematics were derived as described in Westfall et al. (2011a). In the current paper, we will not use any of the derived [OIII] kinematics; instead we will rely on our Hα data taken with SparsePak on the WIYN 3.5 m telescope[3]. The reason why we exclude the [OIII] kinematics is that, empirically, it show large scatter in the velocity fields, likely due to astrophysical properties of the gas such as local outflows associated with star-forming regions, and deviations from circular orbits. Generally, the [OIII] data also have a lower signal-to-noise ratio (S/N) in the line compared to the Hα data. Thus, the [OIII] data suffer more severely from both systematic and random errors in the characterization of the gas rotation curve.

The SparsePak integral-field spectroscopy was obtained in the Hα region for all galaxies in the PPak sample using the setup as described in Table 1 of Paper I. Typically, a three-pointing dither pattern was followed, designed to fully sample the 72″×71″ field-of-view of SparsePak. The reduction of these data, such as basic data reduction, spectral extraction and wavelength calibration, follows methods described in Andersen et al. (2006), and will be described in a forthcoming paper.

The Hα kinematics are measured in a similar way as the [OIII] kinematics (Paper VI), following Andersen et al. (2006, 2008), with both single and double Gaussian line profiles fitted in a 20 Å window centered around each line. Velocities are calculated using the wavelengths of the Gaussian centroids. Of all fitted line profiles, 27% are better fit by a double Gaussian profile (Andersen et al. 2008); in these cases, however, a single component is used to measure the line-of-sight velocity. The measured velocities are used in Sect. 4.1 to derive Hα rotation curves by fitting tilted rings to the data.

2.4. 24-μm Spitzer photometry

For the characterization of the molecular-gas content, we use 24-μm photometry obtained with *Spitzer*. The general motivation and survey strategy for our *Spitzer* observations is provided in Paper I. Images at 4.5, 8, 24, and 70 μm were obtained for all galaxies in the PPak Sample. Here, we will only use the 24-μm MIPS observations to infer the CO surface-brightness distribution from the 24-μm flux, motivated by the well-correlated relations between CO and infrared emission (e.g., Young & Scoville 1991; Paladino et al. 2006; Regan et al. 2006; Bendo et al. 2010). The inferred CO surface brightness follows from the empirical relation derived by Westfall et al. (2011b, hereafter Paper IV) based on the CO and 24-μm data provided by Leroy et al. (2008).

Table 1. Scale lengths and scale heights.

UGC	h_R (kpc)	h_z (kpc)	UGC	h_R (kpc)	h_z (kpc)
448	3.9 ± 0.2	0.46 ± 0.10	4368	3.2 ± 0.3	0.41 ± 0.10
463	3.8 ± 0.2	0.45 ± 0.10	4380	5.0 ± 0.2	0.54 ± 0.12
1081	3.1 ± 0.2	0.40 ± 0.09	4458	9.0 ± 0.4	0.79 ± 0.17
1087	3.2 ± 0.2	0.41 ± 0.09	4555	4.1 ± 0.2	0.48 ± 0.11
1529	3.6 ± 0.1	0.44 ± 0.10	4622	7.6 ± 0.5	0.70 ± 0.16
1635	2.9 ± 0.2	0.39 ± 0.09	6903	4.2 ± 0.4	0.49 ± 0.11
1862	1.4 ± 0.2	0.24 ± 0.06	6918	1.2 ± 0.1	0.21 ± 0.05
1908	4.9 ± 0.2	0.53 ± 0.12	7244	3.9 ± 0.4	0.46 ± 0.11
3091	3.6 ± 0.2	0.44 ± 0.10	7917	8.5 ± 0.4	0.76 ± 0.17
3140	3.5 ± 0.2	0.43 ± 0.10	8196	4.9 ± 0.1	0.53 ± 0.12
3701	3.6 ± 0.4	0.44 ± 0.11	9177	7.0 ± 0.3	0.67 ± 0.15
3997	5.5 ± 0.5	0.58 ± 0.14	9837	5.8 ± 0.4	0.60 ± 0.14
4036	4.3 ± 0.4	0.49 ± 0.12	9965	3.5 ± 0.2	0.44 ± 0.10
4107	3.2 ± 0.2	0.41 ± 0.09	11 318	4.5 ± 0.2	0.51 ± 0.11
4256	4.7 ± 0.2	0.52 ± 0.12	12 391	3.9 ± 0.2	0.46 ± 0.10

Notes. Table containing measured stellar-disk scale lengths (h_R) and inferred stellar-disk scale heights (h_z). The conversion from arcsec to kpc is done using distances tabulated in Paper VI.

[2] Based on observations collected at the Centro Astronómico Hispano Alemán (CAHA) at Calar Alto, operated jointly by the Max-Planck Institut für Astronomie and the Instituto de Astrofísica de Andalucía (CSIC).

[3] The WIYN Observatory, a joint facility of the University of Wisconsin-Madison, Indiana University, Yale University, and the National Optical Astronomy Observatories.

We obtained reliable 24-μm surface photometry and reached $S/N = 3$ per spatial resolution element at $3h_R$, matching the extent of the kinematic IFU measurements. Images of the galaxies at 24 μm can be found in Fig. 9 of Paper I. More details on the reduction will be provided in a forthcoming paper.

2.5. 21-cm radio synthesis imaging

In Martinsson (2011), we presented the reduction and results from our 21-cm radio synthesis observations of 28 galaxies, of which 24 are part of the PPak sample. The observations were obtained using the VLA, WSRT and GMRT arrays, with three galaxies observed by both the VLA and WSRT. The data have been smoothed to ∼15″ angular resolution and ∼10 km s^{-1} velocity resolution, giving typical column-density sensitivities of 2–5 $\times 10^{20}$ atoms cm^{-2}. Here, we will use the derived HI mass surface densities to estimate the amount of atomic gas in the disk (Sect. 3.1), and the measured rotation speed of the HI gas to obtain extended rotation curves (Sect. 4.1).

3. Baryonic mass distributions

This section describes how the mass surface densities of the baryonic components are derived, closely following the analysis as outlined in Paper IV. The mass surface densities will be used in Sect. 5.1 to calculate the baryonic rotation curves. While the atomic gas mass surface density ($\Sigma_{\rm atom}$) is observed directly from our HI observations, the molecular gas mass surface density ($\Sigma_{\rm mol}$) is derived indirectly from 24-μm *Spitzer* observations. The stellar-kinematic observations of σ_z are used to calculate dynamical mass surface densities ($\Sigma_{\rm dyn}$), from which we obtain the stellar mass surface densities (Σ_*) by subtracting the gas mass contributions. From the derived Σ_* and $\mu^i_{K,\rm disk}$, we calculate the average stellar mass-to-light ratio of the galaxy disk ($\overline{\Upsilon_*}$). We assign the same Υ_* to the bulge and the disk, and calculate the radial mass surface density profiles of the stellar disk ($\Sigma_*^{\rm disk}$) and bulge ($\Sigma_*^{\rm bulge}$) separately, as well as their total masses, using radial surface brightness profiles (Sect. 2.2) of the disk and bulge, respectively. The total masses of the various baryonic components are tabulated in Table 3. At the end of this section, we include an investigation of the masses of the various dynamical components in relation to each other and to global photometric and kinematic properties of the galaxies.

3.1. Atomic gas mass surface density

From our 21-cm radio synthesis observations (Sect. 2.5; Martinsson 2011), we have measured the HI mass surface densities ($\Sigma_{\rm HI}$) for 28 galaxies, of which 24 galaxies are also part of the PPak sample. We found that the radial $\Sigma_{\rm HI}$ profiles of these galaxies are well fit with a Gaussian function,

$$\Sigma_{\rm HI}(R) = \Sigma_{\rm HI}^{\rm max} \exp\left[-\frac{(R - R_{\Sigma,\rm max})^2}{2\sigma_\Sigma^2}\right], \quad (2)$$

with $R_{\Sigma,\rm max}$ being the radius at which the profile peaks, σ_Σ the width of the profile, and $\Sigma_{\rm HI}^{\rm max}$ the peak density. The tightest fit is found when normalizing the radius with the HI radius, $R_{\rm HI}$, defined as the radius where $\Sigma_{\rm HI} = 1\ M_\odot$ pc^{-2}. In Martinsson (2011), we also found another tight relation between the total HI mass ($\mathcal{M}_{\rm HI}$) and the HI diameter ($D_{\rm HI} = 2R_{\rm HI}$),

$$\log(\mathcal{M}_{\rm HI}) = 1.72 \log(D_{\rm HI}) + 6.92, \quad (3)$$

Table 2. Modeled $\Sigma_{\rm HI}$.

UGC	Distance (Mpc)	$\int S_{\rm HI} dV$ (Jy km s^{-1})	$\mathcal{M}_{\rm HI}$ ($10^9\ M_\odot$)	$D_{\rm HI}$ (kpc)	$\Sigma_{\rm HI}^{\rm max}$ ($M_\odot$ pc^{-2})
1081[1]	41.8	6.7	2.8	29.5	5.9
1529[1]	61.6	4.4	3.9	36.1	5.6
1862[2]	18.4	3.4	0.3	7.8	8.2
1908[1]	110.0	5.6	16.0	80.4	4.6
3091[3]	73.8	4.2	5.4	43.2	5.3
12 391[1]	66.8	16.4	17.3	82.0	4.5

Notes. Distances are taken from Paper I. Integrated HI fluxes ($\int S_{\rm HI} dV$) are from tabulated values in NED, with three different sources; [(1)] (RC3; de Vaucouleurs et al. 1991); [(2)] (HIPASS; Doyle et al. 2005); [(3)] (Andersen et al. 2006). The total HI mass ($\mathcal{M}_{\rm HI}$), HI diameter ($D_{\rm HI}$) and maximum HI mass surface density ($\Sigma_{\rm HI}^{\rm max}$) are calculated using relations derived in Martinsson (2011).

where $\mathcal{M}_{\rm HI}$ is the mass in units of solar masses and $D_{\rm HI}$ is measured in kpc.

We have direct measurements of $\Sigma_{\rm HI}$ for 24 out of 30 galaxies in this paper. For the remaining six galaxies lacking $\Sigma_{\rm HI}$ measurements, we use our results above to model their $\Sigma_{\rm HI}$ profiles. We calculate $\mathcal{M}_{\rm HI}$ from literature values of the flux from single dish HI observations taken from the NASA/IPAC Extragalactic Database[4] (NED). These $\mathcal{M}_{\rm HI}$ are used in Eq. (3) to calculate $R_{\rm HI}$. We then use Eq. (2), with parameter values found from averaging all 28 galaxies ($R_{\Sigma,\rm max} = 0.39\ R_{\rm HI}$, $\sigma_\Sigma = 0.35\ R_{\rm HI}$), to calculate $\Sigma_{\rm HI}(R)$, where the normalization constant $\Sigma_{\rm HI}^{\rm max}$ is found by calibrating the $\Sigma_{\rm HI}$ profile to our estimated $\mathcal{M}_{\rm HI}$. The calculated $\Sigma_{\rm HI}^{\rm max}$ (Table 2) are typical of the values found for other galaxies in our sample.

We test how the use of Gaussian fits instead of actual $\Sigma_{\rm HI}$ measurements on these 6 galaxies affects our derived results in this paper by recalculating $\overline{\Upsilon_*}$ (Sect. 3.4) and the baryonic maximality at $2.2h_R$ ($\mathcal{F}_{\rm b}^{2.2h_R}$; Sect. 6) for the other 24 galaxies, using Gaussian fits based on their total HI fluxes (taken from Martinsson 2011). The effects appear to be small, with average absolute differences on $\overline{\Upsilon_*}$ and $\mathcal{F}_{\rm b}^{2.2h_R}$ from using the measured $\Sigma_{\rm HI}$ profiles of 4% and 2%, respectively. The differences on individual galaxies are always well within the errors.

To calculate the atomic gas mass surface density, we follow earlier papers in this series (Paper I; Paper II; Paper IV), and multiply $\Sigma_{\rm HI}$ by a factor 1.4 to account for the helium and metal fraction; $\Sigma_{\rm atom} = 1.4\Sigma_{\rm HI}$.

3.2. Molecular gas mass surface density

The mass surface density of the molecular gas ($\Sigma_{\rm mol}$) is inferred from our 24-μm *Spitzer* imaging (Sect. 2.4), as described in Paper IV. This is done in three steps: first, we derive the ^{12}CO($J = 1 \rightarrow 0$) column density ($I_{\rm CO}\Delta V$) from the 24-μm surface brightness using Eq. (1) in Paper IV, converting the sky-subtracted 24-μm image to a CO column-density map. This conversion is expected to provide an estimate for $I_{\rm CO}\Delta V$ to within ∼30% (Paper IV). Subsequently, we calculate the molecular hydrogen (H_2) mass surface density (Σ_{H_2}) from Eq. (2) in Paper IV adopting the same conversion factor, $X_{\rm CO} = (2.7 \pm 0.9) \times 10^{20}$ cm^{-2} (K km s^{-1})$^{-1}$, calculated from combining the

[4] Operated by the Jet Propulsion Laboratory, California Institute of Technology, under contract with the National Aeronautics and Space Administration.

Galactic measurement of X_{CO} from Dame et al. (2001) with the measurements for M 31 and M 33 from Bolatto et al. (2008). Finally, we multiply by a factor 1.4 to add helium and metals to the molecular gas density; $\Sigma_{mol} = 1.4\Sigma_{H_2}$.

The limitations in estimating the molecular-gas content from the observed 24-μm emission is discussed in more detail in Paper IV. Here we note that the estimated systematic errors are fairly large ($\delta\Sigma_{H_2}/\Sigma_{H_2} = 42\%$) and often an important error contributor to the stellar mass-to-light ratios calculated below.

3.3. Dynamical and stellar disk mass surface densities

As mentioned in Sect. 1, the stellar velocity dispersion is a direct indicator of the local mass surface density. In particular, Eq. (1) directly relates σ_z and Σ_{dyn}. The observed line-of-sight velocity dispersions (σ_{LOS}) were presented in Paper VI. These were deprojected into the three components ($\sigma_R, \sigma_\theta, \sigma_z$) of the stellar velocity ellipsoid (SVE), using the derived disk orientations from Paper VI and an SVE shape as justified in Paper II with $\alpha \equiv \sigma_z/\sigma_R = 0.6 \pm 0.15$ and $\beta \equiv \sigma_\theta/\sigma_R = 0.7 \pm 0.04$ at all radii for all galaxies.

From Eq. (1), we calculate the total dynamical mass surface density of the disk. In this paper, we assume a disk with a single scale height and an exponential vertical density distribution (van der Kruit 1988). These assumptions on the structure of the disk have their limitations, especially in the very center of the galaxy where a non-negligible bulge or a bar may be present, and in the outer part of the disk, which could be affected by the dark-matter halo or may be flared (e.g., de Grijs & Peletier 1997). However, in our analysis we exclude any kinematic measurements inside the bulge region, and measurements in the outer disk will be heavily down-weighted due to larger measurement errors. More discussion on the effects of possible systematic errors is presented in Sect. 8.

The measured stellar mass surface density (Σ_*) is derived by subtracting the atomic and molecular gas mass surface densities from Σ_{dyn},

$$\Sigma_* = \Sigma_{dyn} - \Sigma_{atom} - \Sigma_{mol}. \quad (4)$$

We assume that any dark matter in the disk is distributed in the same way as the stars, and is effectively incorporated into Σ_*.

In the following subsection, we calculate the average stellar mass-to-light ratios of the disks and use these together with the surface brightness to calculate Σ_*. We do this to be able to separate the bulge and disk, which have different density distributions and therefore need to be treated differently when modeling their rotation curves, and to calculate Σ_* profiles that reach further out in radius, beyond our stellar-kinematic measurements. The measured and calculated Σ_* profiles are provided in the Atlas (Appendix A.3).

3.4. Mass-to-light ratios

We calculate dynamical (Υ_{dyn}) and stellar (Υ_*) mass-to-light ratios using our measurements of Σ_{dyn} and Σ_*, respectively; both are calculated in the K-band using $\mu^i_{K,disk}$. Error-weighted radial averages ($\overline{\Upsilon_{dyn}}$ and $\overline{\Upsilon_*}$) are calculated after excluding radial regions where our dynamical and/or structural assumptions are less robust. In particular, we exclude data within $R = R_{bulge}$, and $R = 2\farcs5$ if no bulge is apparent. For UGC 7917, we extend the excluded region to $1h_R$ due to the presence of a bar. For UGC 4458, R_{bulge} is larger than the field-of-view of the PPak IFU, and we shorten the radius to be able to include the outermost measurement. At this radius, the bulge contributes 21% to the light. For each galaxy, the excluded regions are indicated by gray shaded areas in the Atlas. For UGC 8196, our analysis gives us non-physical results when calculating the baryon maximality (see Sect. 6), possibly due to an erroneous measurement of Υ_{dyn}. We therefore exclude this galaxy from all our results in this paper related to Υ_{dyn}.

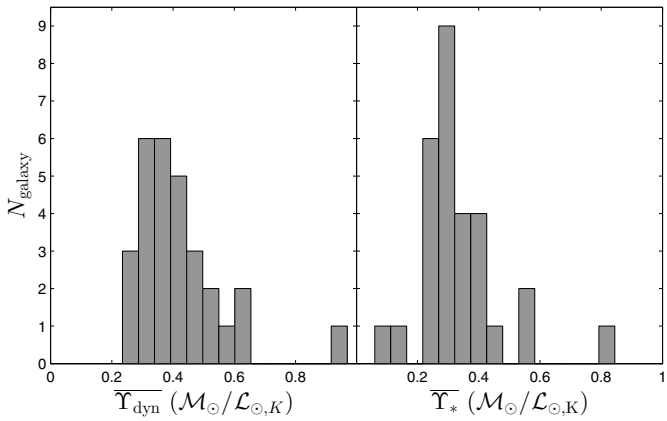

Fig. 1. Distributions of radially-averaged dynamical (*left*) and stellar (*right*) mass-to-light ratios.

Figure 1 shows the distributions of $\overline{\Upsilon_{dyn}}$ and $\overline{\Upsilon_*}$. We find the weighted radial averages and scatter of the sample to be $\langle\overline{\Upsilon_{dyn}}\rangle = 0.39 \pm 0.08\ M_\odot/L_{\odot,K}$ and $\langle\overline{\Upsilon_*}\rangle = 0.31 \pm 0.07\ M_\odot/L_{\odot,K}$. The effective radius at which $\overline{\Upsilon_*}$ is measured (R_Υ; calculated using the same weights as used for $\overline{\Upsilon_*}$) has a weighted sample average and scatter of $\langle R_\Upsilon\rangle = 1.0 \pm 0.3h_R$. The calculated $\overline{\Upsilon_*}$ and R_Υ of the individual galaxies are tabulated in Table 6.

The radially-averaged mass-to-light ratios are weighted more towards measurements in the inner region of the galaxy due to increasing errors with radius. Even if the galaxies have constant Υ_* with radius, Υ_{dyn} will still vary if the radial distribution of the gas is different from that of the stars. If there is relatively more gas further out in the disk than in the inner region (as seen in Fig. 3), the error-weighted mean $\overline{\Upsilon_{dyn}}$ will be lower than the total baryonic mass-to-light ratio $\Upsilon_b = \mathcal{M}_b/\mathcal{L}_K$, which is calculated from the total integrated baryonic mass ($\mathcal{M}_b$; Table 3) and the total K-band luminosity ($\mathcal{L}_K$). Figure 2 shows the baryonic and stellar mass as a function of $\mathcal{L}_K$ and demonstrates that $\mathcal{M}_b$ tends to be larger than what is expected from $\langle\overline{\Upsilon_{dyn}}\rangle$. In detail, we find $\langle\Upsilon_b\rangle = 0.49\ M_\odot/L_{\odot,K} = 1.3 \times \langle\overline{\Upsilon_{dyn}}\rangle$ as expected given the generally larger radial extent of the HI disks (Martinsson 2011).

In many galaxies, we find that Υ_* increases toward larger radii (see UGC 4107, UGC 4368 & UGC 9965 in the Atlas). Three possible explanations for this are:

1. The mass-to-light ratio of the stellar population could in fact be rising at larger radii. Even though color gradients are often seen in spiral galaxies (e.g., de Jong 1996), these are usually small and do not sufficiently explain the increase in Υ_* within the context of stellar-population variations (see discussion on UGC 463 in Paper IV).
2. There could be unknown systematic instrumental errors, such that the measurement of the observed velocity dispersion "hit the floor", giving systematically larger measurements of σ_{LOS}. Indeed, the skewed (non-Gaussian) shape of the velocity-dispersion error distribution for our data may

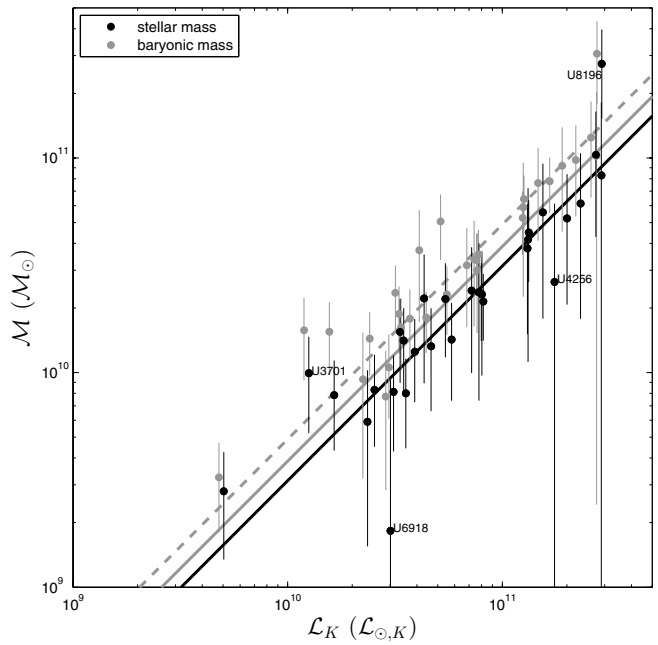

Fig. 2. Mass ($\mathcal{M}$) versus luminosity ($\mathcal{L}_K$). Total baryonic mass (stars+gas; gray symbols, slightly offset in $\mathcal{L}_K$ for clarity) and stellar mass (disk+bulge; black symbols) as a function of luminosity. The solid lines indicate the average measured $\langle\overline{\Upsilon_{\rm dyn}}\rangle$ (gray) and $\langle\overline{\Upsilon_*}\rangle$ (black). The average ratio $\mathcal{M}_{\rm b}/\mathcal{L}_K$ of the sample ($\langle\Upsilon_{\rm b}\rangle$; see text) is indicated with a gray dashed line.

indicate the presence of such an effect. However, with our relatively high velocity resolution ($\sigma_{\rm inst} \approx 16.6 \pm 1.4$ km s^{-1}; Paper VI) and a rather conservative rejection cut ($\delta\sigma_{\rm LOS} \geq 8$ km s^{-1}), we do not expect this to happen at the level where we see the increasing Υ_* ($\sigma_{\rm LOS} > 20$ km s^{-1}). Moreover, σ_z often follows an exponential decline well, while changes in the light profile are the primary reason for the increased Υ_* (e.g., UGC 1862).

3. Our assumptions for calculating $\Sigma_{\rm dyn}$ using Eq. (1) may not be valid at larger radii. There are several reasons why we could get larger σ_z values than what would be expected from the local mass surface density of the disk. If the stellar disk is flaring at larger radii, our assumption of a constant scale height no longer holds, resulting in an overestimate of $\Sigma_{\rm dyn}$. The dark-matter halo could also have an effect on the stellar velocity dispersions, which might become more important at larger radii.

In this paper, we have simply assumed a constant Υ_*, calculated using all measurements outside the bulge region. However, since the errors increase with radius, our error-weighted mean $\overline{\Upsilon_*}$ hinges on measurements in the inner, high S/N region of each galaxy. The variation of Υ_* (within each galaxy and among different galaxies) are interesting in the context of star formation and the stellar IMF. Here, measurements of Υ_* often have large systematic errors, partly due to the uncertain subtraction of the molecular gas from $\Sigma_{\rm dyn}$. However, even though we see some scatter in Fig. 2, the measured $\overline{\Upsilon_*}$ are in general consistent with being equal for all galaxies. A detailed discussion on mass-to-light ratios in the context of stellar populations and star formation, including an investigation of trends with other global properties of the disk such as luminosity, surface brightness, color, or scale length, will be presented in a forthcoming paper.

Table 3. Total masses of the baryonic components.

UGC	$\log(\mathcal{M}_*^{\rm disk})$ ($M_\odot$)	$\log(\mathcal{M}_*^{\rm bulge})$ ($M_\odot$)	$\log(\mathcal{M}_{\rm atom})$ ($M_\odot$)	$\log(\mathcal{M}_{\rm mol})$ ($M_\odot$)	$\log(\mathcal{M}_{\rm b})$ ($M_\odot$)
448	$10.25^{+0.23}_{-0.51}$	$9.76^{+0.23}_{-0.51}$	$9.88^{+0.04}_{-0.05}$	$9.39^{+0.15}_{-0.23}$	$10.53^{+0.18}_{-0.31}$
463	$10.54^{+0.21}_{-0.41}$	$9.35^{+0.21}_{-0.41}$	$9.57^{+0.04}_{-0.05}$	$10.04^{+0.15}_{-0.23}$	$10.72^{+0.12}_{-0.17}$
1081	$10.12^{+0.16}_{-0.24}$	$8.81^{+0.16}_{-0.24}$	$9.59^{+0.04}_{-0.05}$	$8.89^{+0.15}_{-0.23}$	$10.27^{+0.13}_{-0.18}$
1087	$10.08^{+0.16}_{-0.25}$	$8.64^{+0.16}_{-0.25}$	$9.67^{+0.04}_{-0.05}$	$8.84^{+0.15}_{-0.23}$	$10.25^{+0.14}_{-0.20}$
1529	$10.34^{+0.20}_{-0.39}$	$8.98^{+0.20}_{-0.39}$	$9.74^{+0.04}_{-0.05}$	$9.12^{+0.15}_{-0.23}$	$10.47^{+0.17}_{-0.29}$
1635	$9.88^{+0.17}_{-0.29}$	$8.74^{+0.17}_{-0.29}$	$9.32^{+0.04}_{-0.05}$	$8.57^{+0.15}_{-0.23}$	$10.03^{+0.15}_{-0.24}$
1862	$9.45^{+0.20}_{-0.37}$	–	$8.58^{+0.04}_{-0.05}$	$7.85^{+0.15}_{-0.24}$	$9.51^{+0.16}_{-0.26}$
1908	$10.74^{+0.23}_{-0.54}$	$9.68^{+0.23}_{-0.54}$	$10.35^{+0.04}_{-0.05}$	$10.15^{+0.15}_{-0.23}$	$10.99^{+0.16}_{-0.26}$
3091	$9.90^{+0.17}_{-0.28}$	–	$9.88^{+0.04}_{-0.05}$	$8.85^{+0.15}_{-0.23}$	$10.21^{+0.14}_{-0.20}$
3140	$10.59^{+0.15}_{-0.24}$	$9.65^{+0.15}_{-0.24}$	$10.11^{+0.04}_{-0.05}$	$9.82^{+0.15}_{-0.23}$	$10.80^{+0.11}_{-0.14}$
3701	$10.00^{+0.18}_{-0.31}$	$8.69^{+0.18}_{-0.31}$	$9.75^{+0.04}_{-0.05}$	$8.28^{+0.15}_{-0.24}$	$10.21^{+0.15}_{-0.23}$
3997	$10.16^{+0.17}_{-0.27}$	$8.53^{+0.17}_{-0.27}$	$9.88^{+0.04}_{-0.05}$	$8.74^{+0.15}_{-0.22}$	$10.36^{+0.13}_{-0.18}$
4036	$10.35^{+0.15}_{-0.23}$	$8.92^{+0.15}_{-0.23}$	$9.88^{+0.04}_{-0.05}$	$9.42^{+0.15}_{-0.23}$	$10.52^{+0.12}_{-0.17}$
4107	$10.10^{+0.18}_{-0.31}$	$8.65^{+0.18}_{-0.31}$	$9.43^{+0.04}_{-0.05}$	$9.32^{+0.15}_{-0.23}$	$10.25^{+0.12}_{-0.16}$
4256	$10.38^{+0.36}_{-10.38}$	$9.29^{+0.36}_{-9.29}$	$10.33^{+0.04}_{-0.05}$	$10.48^{+0.15}_{-0.23}$	$10.89^{+0.11}_{-0.15}$
4368	$10.37^{+0.21}_{-0.41}$	$9.21^{+0.21}_{-0.41}$	$10.13^{+0.04}_{-0.05}$	$9.17^{+0.15}_{-0.23}$	$10.60^{+0.19}_{-0.33}$
4380	$10.32^{+0.13}_{-0.20}$	$8.86^{+0.13}_{-0.20}$	$10.08^{+0.04}_{-0.05}$	$9.29^{+0.15}_{-0.23}$	$10.56^{+0.12}_{-0.16}$
4458	$10.81^{+0.20}_{-0.39}$	$10.67^{+0.20}_{-0.39}$	$10.26^{+0.04}_{-0.05}$	$9.45^{+0.15}_{-0.23}$	$11.13^{+0.17}_{-0.28}$
4555	$10.39^{+0.20}_{-0.39}$	$8.96^{+0.20}_{-0.39}$	$9.71^{+0.04}_{-0.05}$	$9.39^{+0.15}_{-0.23}$	$10.51^{+0.17}_{-0.29}$
4622	$10.69^{+0.21}_{-0.41}$	$9.89^{+0.21}_{-0.41}$	$10.55^{+0.04}_{-0.05}$	$9.65^{+0.15}_{-0.23}$	$10.98^{+0.18}_{-0.31}$
6903	$9.73^{+0.25}_{-0.62}$	$8.03^{+0.25}_{-0.62}$	$9.49^{+0.04}_{-0.05}$	$8.48^{+0.15}_{-0.22}$	$9.96^{+0.22}_{-0.46}$
6918	$9.23^{+0.70}_{-9.23}$	$8.04^{+0.70}_{-8.04}$	$9.37^{+0.04}_{-0.05}$	$9.55^{+0.15}_{-0.23}$	$9.89^{+0.21}_{-0.44}$
7244	$9.83^{+0.17}_{-0.29}$	–	$9.86^{+0.04}_{-0.05}$	$8.68^{+0.14}_{-0.22}$	$10.16^{+0.14}_{-0.20}$
7917	$10.87^{+0.34}_{-10.87}$	$10.01^{+0.34}_{-10.01}$	$10.14^{+0.04}_{-0.05}$	$9.73^{+0.15}_{-0.23}$	$11.01^{+0.30}_{-1.62}$
8196	$11.35^{+0.16}_{-0.26}$	$10.73^{+0.16}_{-0.26}$	$10.45^{+0.04}_{-0.05}$	$9.56^{+0.15}_{-0.23}$	$11.48^{+0.15}_{-0.23}$
9177	$10.64^{+0.24}_{-0.58}$	$9.55^{+0.24}_{-0.58}$	$10.15^{+0.04}_{-0.05}$	$9.45^{+0.15}_{-0.23}$	$10.81^{+0.21}_{-0.42}$
9837	$9.87^{+0.17}_{-0.29}$	$8.35^{+0.17}_{-0.29}$	$9.75^{+0.04}_{-0.05}$	$8.65^{+0.15}_{-0.24}$	$10.15^{+0.12}_{-0.17}$
9965	$10.16^{+0.17}_{-0.29}$	–	$9.79^{+0.04}_{-0.05}$	$9.44^{+0.15}_{-0.23}$	$10.37^{+0.13}_{-0.19}$
11318	$10.60^{+0.23}_{-0.50}$	$9.69^{+0.23}_{-0.50}$	$10.05^{+0.04}_{-0.05}$	$9.97^{+0.15}_{-0.23}$	$10.81^{+0.16}_{-0.27}$
12391	$10.33^{+0.17}_{-0.28}$	$8.98^{+0.17}_{-0.28}$	$10.38^{+0.04}_{-0.05}$	$9.64^{+0.15}_{-0.23}$	$10.71^{+0.13}_{-0.18}$

Notes. Calculated masses of the stellar disk ($\mathcal{M}_*^{\rm disk}$), stellar bulge ($\mathcal{M}_*^{\rm bulge}$), atomic gas ($\mathcal{M}_{\rm atom}$), molecular gas ($\mathcal{M}_{\rm mol}$), and total baryonic mass of the galaxies ($\mathcal{M}_{\rm b}$).

For all subsequent analysis, we calculate the radial mass surface density profiles of the stellar disk ($\Sigma_*^{\rm disk}$) and bulge ($\Sigma_*^{\rm bulge}$) based on the disk and bulge surface brightness profiles (Sect. 2.2) and a single $\overline{\Upsilon_*}$ calculated for each galaxy.

3.5. Baryonic mass surface density profiles and total mass fractions

The mass surface densities of the individual baryonic components ($\Sigma_{\rm atom}$, $\Sigma_{\rm mol}$, $\Sigma_*^{\rm disk}$, $\Sigma_*^{\rm bulge}$) are plotted out to 50″ for every galaxy in the Atlas. For a majority of the galaxies in our sample, the total baryonic mass surface density is dominated by the

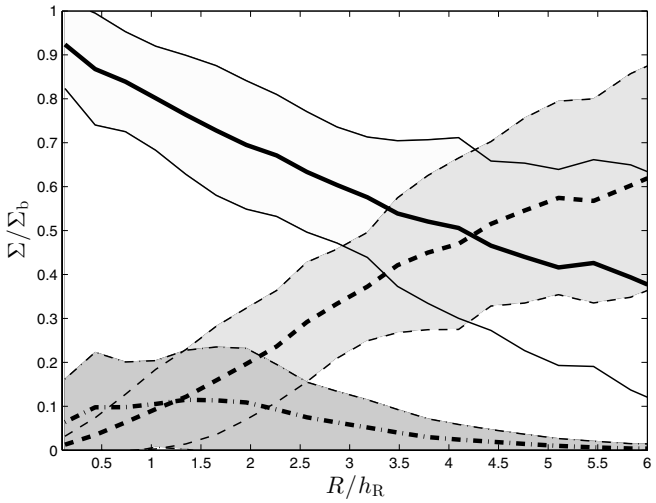

Fig. 3. Relative fraction of stellar, atomic-gas, and molecular-gas mass surface densities as a function of radius. The solid thick and thin lines show the average Σ_*/Σ_b and 1σ scatter, respectively. The dashed thick and thin lines (enclosing the light gray area) and the dashed-dotted thick and thin lines (enclosing the dark gray area) show the average Σ_{atom}/Σ_b and Σ_{mol}/Σ_b, respectively, again with the thin lines indicating 1σ scatter.

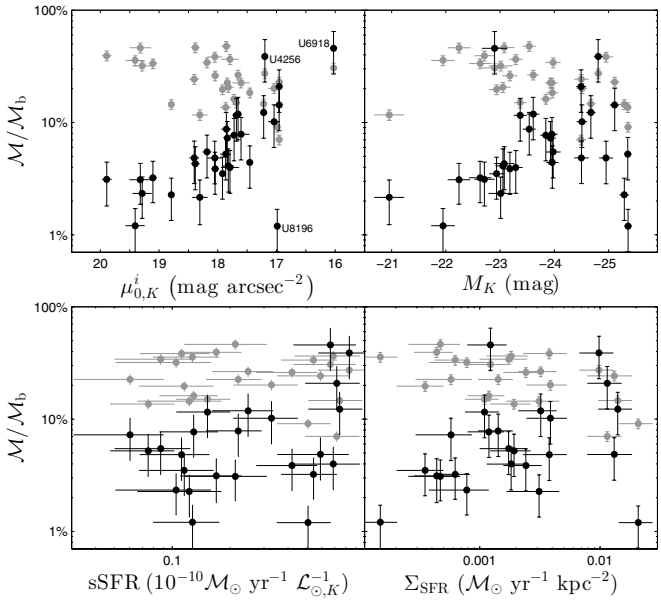

Fig. 4. Molecular ($\mathcal{M}_{mol}/\mathcal{M}_b$; black symbols) and atomic ($\mathcal{M}_{atom}/\mathcal{M}_b$; gray symbols) gas-mass fractions as a function of $\mu^i_{0,K}$, M_K, sSFR and Σ_{SFR}.

stellar component over most of this radial range. However, some galaxies have a relatively large molecular-gas content distributed in a way similar to the stars; 12 galaxies have a molecular gas mass larger than 10% of the stellar mass, of which 8 galaxies have a molecular-gas content larger than 10% of the total baryonic mass. Two galaxies (UGC 4256 and UGC 6918) even have a larger molecular gas mass than stellar mass, although it should be noted that these two galaxies have the lowest Υ_* in the sample, with large uncertainties in both the molecular and stellar mass.

Σ_{mol} is often higher than Σ_{atom} out to $\sim$1–2h_R. In the outer parts of the disk, the atomic gas starts to dominate the mass surface density of the baryonic matter. Figure 3 shows the average fraction in mass surface density of the stars, atomic gas, and molecular gas. In the center, typically more than 90% of the baryonic matter is in stars, while the relative amount of atomic gas is steadily increasing with radius. On average, at about $4h_R$, the relative amount of gas and stars are comparable. The atomic gas then typically dominates the baryonic mass surface density at $R \gtrsim 4h_R$.

Figure 4 demonstrates that the molecular gas mass fraction (indicated with black symbols) is rather well correlated with the central surface brightness of the disk; the galaxy disks in our sample with higher surface brightness also have higher molecular gas mass fraction. More luminous galaxies also tend to have larger molecular gas mass fractions, but with large scatter, especially for high-luminosity galaxies. We see no correlation with the specific star-formation rate (sSFR; calculated from the 21-cm continuum flux in Martinsson 2011), but note that the two galaxies with the largest molecular-gas fraction (UGC 4256 and UGC 6918) are among the galaxies with the largest sSFR. There is also a weak trend of increased SFR density (Σ_{SFR}; Martinsson 2011) for galaxies with larger molecular-gas fractions. However, it should be noted again that the molecular-gas content is an indirect estimate from the 24-μm emission.

The atomic gas mass fractions (indicated in Fig. 4 with gray symbols) are in general larger than the molecular gas mass fractions. Correlations with $\mu^i_{0,K}$, M_K, sSFR and Σ_{SFR} are weak and have opposite sign to correlations found for the molecular gas mass fraction, resulting in total gas mass fractions that are consistent with having no correlations with $\mu^i_{0,K}$, M_K, sSFR or Σ_{SFR}.

3.5.1. Comparison to literature

To be able to compare our gas-mass fractions with the literature, we will below compare the atomic and molecular gas masses with the derived stellar masses instead of the total baryonic masses. It should however be noted that these measurements have larger uncertainties due to the additional uncertainties on the stellar masses.

Recent studies of the gas content in galaxies using CO and HI observations (Leroy et al. 2009; Saintonge et al. 2011) have found a molecular gas mass content that is typically 3–10% of the stellar mass. For the galaxies in our sample, we find that more than one third have a molecular gas mass larger than 10% of the stellar mass. This is larger than found by Leroy et al. (2009) or Saintonge et al. (2011), probably because of differences in the way the stellar mass is determined (see below). However, this could also be due to differences in the samples, as the molecular gas-mass fraction seems to correlate with some global galaxy parameters (Fig. 4).

Figure 5 shows the distributions of $R_{mol} = \mathcal{M}_{mol}/\mathcal{M}_{atom}$, $f_{mol} = \mathcal{M}_{mol}/\mathcal{M}_*$ and $f_{atom} = \mathcal{M}_{atom}/\mathcal{M}_*$. We calculate the geometric means and scatter to be $\langle R_{mol}\rangle = 0.25^{+0.44}_{-0.16}$, $\langle f_{mol}\rangle = 0.10^{+0.17}_{-0.06}$, and $\langle f_{atom}\rangle = 0.38^{+0.36}_{-0.18}$. The values for individual galaxies cover two orders of magnitudes for ratios including the molecular gas ($0.03 < R_{mol} < 2.98, 0.02 < f_{mol} < 1.93$) and one order of magnitude for the atomic gas mass fraction ($0.10 < f_{atom} < 1.30$). These averages and scatters are similar to what was found by Leroy et al. (2009) and Saintonge et al. (2011). After correcting for differences in adopted X_{CO} values, these studies find average R_{mol} that are comparable to what we find, with similar scatter. They find gas-mass fractions (f_{atom} and f_{mol}) that are $\sim$30–60% lower than what we report. The reason for this systematically lower gas-mass fractions are likely partly due to the differences in how the stellar masses

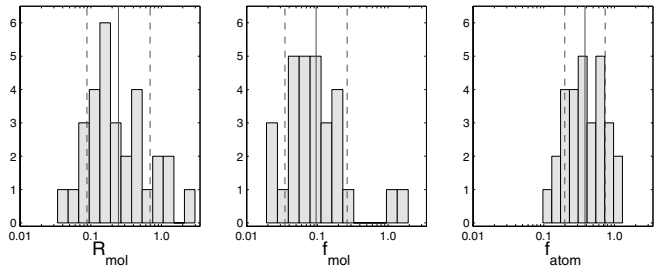

Fig. 5. Gas-mass fractions. The vertical solid and dashed lines indicate the mean and one standard deviation from the mean, respectively.

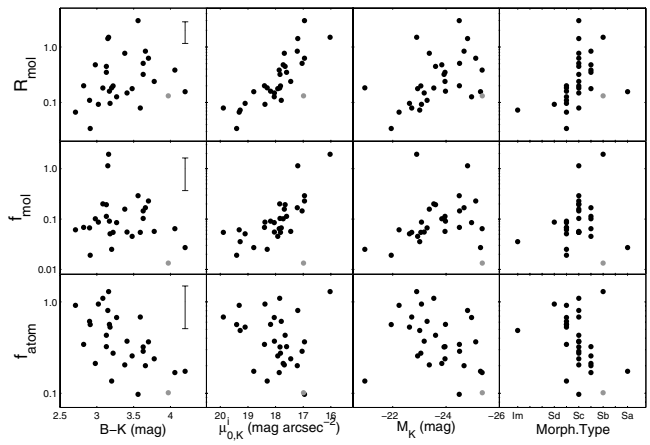

Fig. 6. Relations between gas-mass fractions and other global properties of the galaxies. The errorbars in the upper-right corners of the panels in the left column indicate typical (mostly systematic) errors. UGC 8196 is marked with a gray symbol.

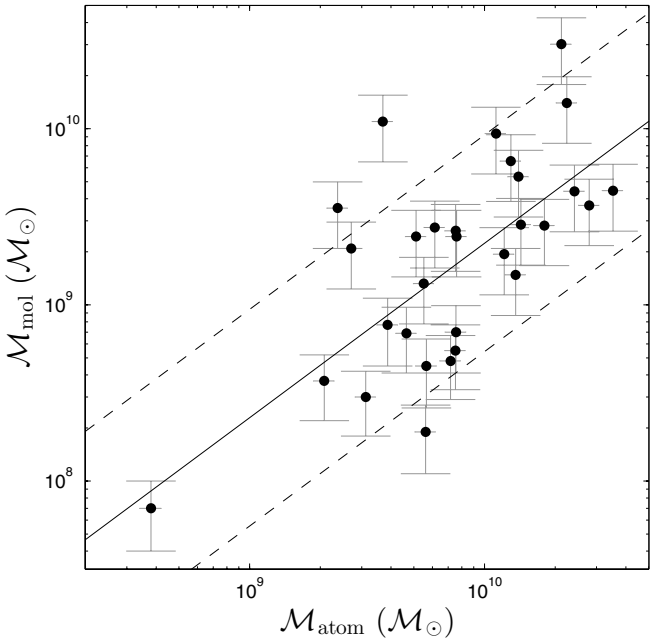

Fig. 7. $\mathcal{M}_{\rm mol}$ versus $\mathcal{M}_{\rm atom}$. The solid and two dashed lines show the fit from Saintonge et al. (2011); $\log \mathcal{M}_{\rm mol} = 0.99(\log \mathcal{M}_{\rm atom}) - 0.42 \pm 1.5\sigma$, where $\sigma = 0.41$ dex and $\mathcal{M}_{\rm mol}$ has been corrected for a 35% difference in the adopted $X_{\rm CO}$ value.

are determined. While we measure the stellar masses dynamically, Leroy et al. (2009) assume a constant $\Upsilon_* = 0.5$, which is ~60% larger than our mean Υ_* (Sect. 3.4), and Saintonge et al. (2011) calculate their stellar masses from spectral energy distribution (SED) fitting techniques. These could have factors of 2–3 systematic errors (e.g., Kauffmann et al. 2003; Paper V); however, the discrepancies we find here are smaller than that.

The equivalents to our two extreme cases UGC 4256 and UGC 6918 (with $f_{\rm mol}$ equal to 1.1 and 1.9, both with low Υ_*) cannot be found in these two studies; Leroy et al. (2009) and Saintonge et al. (2011) find a highest measurement of 0.25 and 0.20, respectively. However, our extreme case UGC 463 with a $R_{\rm mol} = 2.98$, can be compared to the extreme cases of 1.13 in Leroy et al. (2009) and 4.09 in Saintonge et al. (2011).

Figure 6 shows relations between the mass fractions and color, surface brightness, absolute magnitude and morphological type. For $R_{\rm mol}$ we see trends with all four properties; redder, more luminous, higher surface brightness, and earlier-type galaxies have a larger fraction of molecular gas compared to the amount of atomic gas. Saintonge et al. (2011) find similar, though weaker, trends with $R_{\rm mol}$, but the correlations with $f_{\rm mol}$ are somewhat different, especially compared to the surface brightness. While they find a weak negative trend with effective stellar surface density, we find a rather strong positive trend with the disk central surface brightness. However, note that the stellar surface density in Saintonge et al. (2011) and our $\mu^i_{0,K}$ are defined and measured in very different ways. In accordance with Catinella et al. (2010), $f_{\rm atom}$ is correlated with color, surface brightness and luminosity. We also find that the late-type galaxies in our sample tend to have larger $f_{\rm atom}$. We note that $f_{\rm mol}$ and $f_{\rm atom}$ have consistently opposite trends with $\mu^i_{0,K}$ and M_K; higher-surface-brightness and more luminous galaxies have larger $f_{\rm mol}$, while the opposite is true for $f_{\rm atom}$. This implies a trend in conversion rate of HI to H_2 and/or in star-formation efficiency.

Assuming that molecular gas forms out of clouds of atomic gas, one might expect a tight correlation between $\mathcal{M}_{\rm atom}$ and $\mathcal{M}_{\rm mol}$. However, as shown by Saintonge et al. (2011) and from our own measured $R_{\rm mol}$, there is a large scatter in this relation. Figure 7 shows $\mathcal{M}_{\rm mol}$ versus $\mathcal{M}_{\rm atom}$. After accounting for the offset due to our adopted $X_{\rm CO}$ value, we find that our galaxies follow the relation from Saintonge et al. (2011) rather well and with similar scatter.

4. Observed rotation curves and their shapes

4.1. Combined Hα and HI rotation curves

The rotational velocities of the galaxy disks were measured in Paper VI (stellar and [OIII] gas) and in Martinsson (2011) (HI gas). Here, we exclude the stellar rotation curves, which are affected by asymmetric drift, as well as the [OIII] rotation curves (see Sect. 2.3). Instead, we combine our HI rotation curves with Hα rotation curves, derived from data taken with the SparsePak IFU (Sect. 2.3). We use the available Hα kinematics to create Hα rotation curves by azimuthally averaging velocity measurements in 5″ broad concentric tilted rings, sampled at radii $R_j = 2.5'' + j \times 5''$ (where $j = 0, 1, 2, ...$), complementing the HI velocities sampled at radii $R_j = 5'' + j \times 10''$. The Hα rotation curves are derived in the same way as the stellar and [OIII] rotation curves, as described in Paper VI. Due to uncertainties in the instrumental position angle of the SparsePak instrument, we let the position angle be a free parameter while fitting the Hα rotation curve. The differences in the derived position angles between the Hα and HI velocity fields are however small (see Fig. 5.8 in Martinsson 2011) and generally consistent

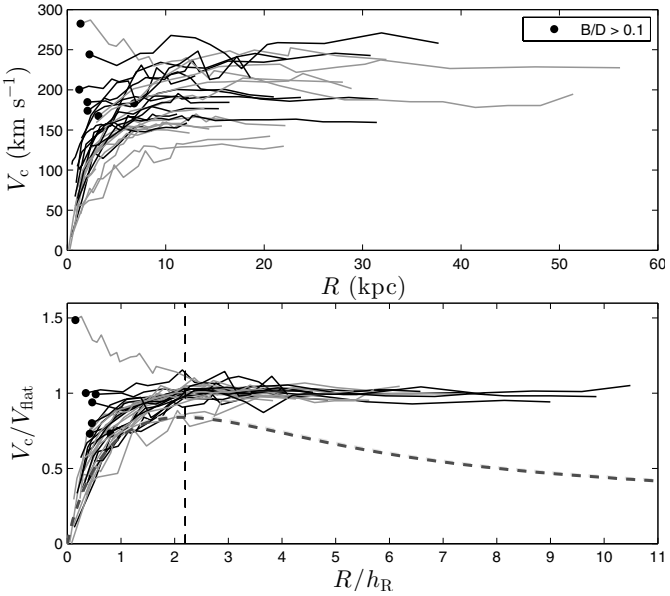

Fig. 8. Observed rotation curves. *Top*: radius in kpc and amplitude in km s^{-1}. *Bottom*: radius scaled by h_R and amplitude scaled by the rotational velocity of the flat part of the rotation curve (V_{flat}). Galaxies with $B/D > 0.1$ have their first velocity measurement marked by a filled circle. In both panels, black and gray lines indicate high and low surface brightness, respectively. The thick, dashed line in the *bottom panel* indicates the rotation curve of a thin exponential disk with $V_{max} = 0.85V_c$. $R = 2.2h_R$ is indicated with a vertical dashed line.

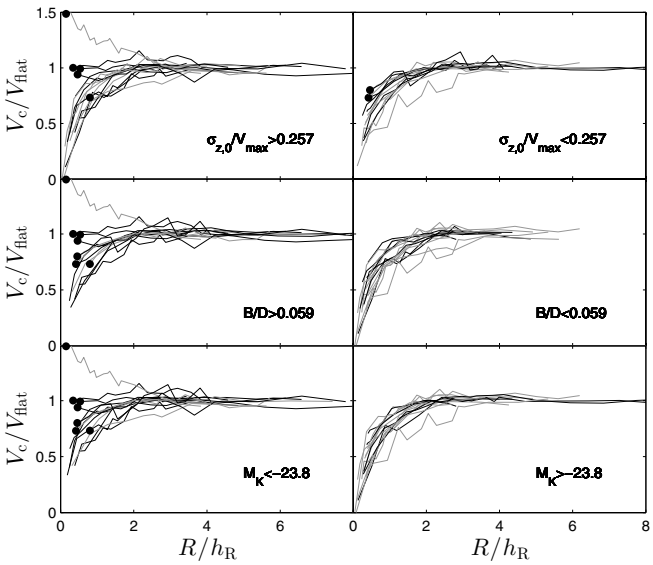

Fig. 9. Observed rotation curves, divided into bins of high and low $\sigma_{z,0}/V_{max}^{OIII}$ (*top row*), B/D (*middle row*), and M_K (*bottom row*). Lines are coded as in Fig. 8.

with no offset, with an average absolute measured difference of 1.°8 and a maximum difference of 5°.

Also, the adopted center of the galaxy might be slightly different between the two data sets. While the HI rotation velocities are measured using the morphological center obtained from fitting reconstructed continuum images of the PPak data to optical DSS and SDSS images (Paper VI), the Hα rotation curves are derived using the fitted kinematic center. We expect the differences between the morphological and best-fitted kinematic centers to be less than 2″ (Paper VI), and mostly dependent on the regularity of the Hα velocity fields. The inclinations of the disks have been fixed to the inverse Tully-Fisher inclinations (i_{TF}; Rix & Zaritsky 1995; Verheijen 2001) as derived in Paper VI. The combined HI and Hα rotation curves are shown for each galaxy in the Atlas with open and solid symbols, respectively.

The velocities of the Hα and HI gas are expected to be nearly identical with only minimal variations due to small differences in asymmetric drift. Indeed, the derived Hα and HI rotation curves are typically in excellent agreement. However, for some galaxies (UGC 3140, UGC 3997, UGC 4256, UGC 7244; see Atlas), we note that the derived Hα and HI rotation curves have slightly different shapes. We do not believe these differences to be physical, but likely the result of systematic errors in deriving the two rotation curves independently, e.g., due to the small differences in center and position angle mentioned above. In one extreme case (UGC 7244), the difference arises due to a large kinematic asymmetry between the receding and approaching side of the galaxy, with the rotation curve rising much steeper on the receding side than on the approaching side. This is reflected in the large errorbars on the HI velocities, where the errors are dominated by the difference between the receding and approaching side of the rotation curve (see Martinsson 2011). Curiously, we do not find the same asymmetry in the Hα kinematics, which follow a more shallow shape on both the receding and approaching side.

4.2. The shapes of the observed rotation curves

The combined HI+Hα rotation curves are shown together in Fig. 8. As seen in this figure, galaxies with a higher bulge-to-disk ratio ($B/D > 0.1$) have a steeper rise in their rotation curves, indicating a higher central concentration of mass. In the bottom panel we see that all rotation curves are fairly self-similar, and that they have reached the flat part by $3h_R$. No difference can be seen in the shape of the scaled rotation curves between low ($17.84 < \mu^i_{0,K} < 19.89$) and high ($16.03 < \mu^i_{0,K} < 17.84$) surface brightness galaxies. The dashed dark gray line in the bottom panel shows the rotation curve of a thin exponential disk which has a maximum rotation speed that is 85% of the observed circular speed at its maximum[5], the fraction a maximum disk would have (Sackett 1997). As expected, even though the stellar disk often displays a close-to-exponential decline, we find that the observed rotation curves depart from the exponential-disk case, both at small and large radii. This is due to the presence of additional mass components, such as the bulge and the dark-matter halo.

In Fig. 9, we divide the rotation curves into bins of high and low dispersion/velocity ratio ($\sigma_{z,0}/V_{max}$; an indicator of the disk maximality (Paper V)), bulge/disk ratio (B/D) and absolute magnitude (M_K). In the upper row of Fig. 9 we see that galaxies with the steepest inner rise of the rotation curve tend to have a higher $\sigma_{z,0}/V_{max}$ ratio. The separation in B/D (middle row) shows the same, but even clearer, and in the bottom row we see it again (low-luminosity galaxies have often smaller bulges and tend to have a smaller $\sigma_{z,0}/V_{max}$ ratio).

5. Rotation-curve mass decompositions

This section describes how we decompose the observed rotation curves presented in the previous section into their baryonic components (Sect. 5.1) and a parametrized dark-matter-halo component (Sect. 5.2). We define two cases with different scaling of

[5] In this paper we use $R^{disk}_{max} \equiv 2.2h_R$, the radius at which the circular speed peaks for a razor-thin, radially exponential disk.

the stellar rotation curve; Case I (Sect. 5.3) assumes our nominal $\overline{\Upsilon_*}$ measurements, while Case II (Sect. 5.4) scales $\overline{\Upsilon_*}$ by a galaxy-dependent factor f_* to satisfy the maximum-disk hypothesis. These cases are divided into Cases Ia and IIa, which have a parameterized dark-matter halo modeled as a spherical pseudo-isothermal sphere (pISO; e.g., Ostriker & Caldwell 1979; Schmidt 1985; Kent 1986), and Cases Ib and IIb which instead include a Navarro-Frenk-White (NFW; Navarro et al. 1997) dark-matter-halo model. In Sect. 5.5 we compare how well the different cases fit the observed rotation curves, with the results discussed further in Sect. 8.

5.1. Rotation curves of the baryonic components

The rotation curves of the various baryonic components are calculated from their radial mass surface density profiles and an assigned three-dimensional axisymmetric density distribution using the task ROTMOD in GIPSY[6] (van der Hulst et al. 1992; Vogelaar & Terlouw 2001). The shape of the stellar rotation curve follows from the light profile of the galaxy, while the amplitude is set by $\sqrt{\Upsilon_*}$. We adopt an exponential vertical distribution for the stellar disk with a constant scale height h_z, as calculated in Sect. 2.2 and presented in Table 1. For the stellar bulge, we assume a spherical density distribution. The atomic and molecular gas are assumed to be distributed in razor-thin disks.

Non-exponential features in the disk light profile result in "bumps" in the rotation curve and a peak that does not necessarily occur at $2.2h_R$. Due to the ring-like distribution of the HI gas, a "negative" rotation speed[7] of the atomic-gas rotation curve is often found in the inner part of the galaxy. This arises due to the outward force from the atomic gas; the HI disk is not counter-rotating in the center. The derived rotation curves are shown for individual galaxies in the Atlas.

The total gravitational potential can be considered as being composed from independent and separable density distributions. This allows us to add the calculated circular velocities of the stellar disk ($V_{\rm disk,*}$), stellar bulge ($V_{\rm bulge,*}$), atomic gas ($V_{\rm atom}$) and molecular gas ($V_{\rm mol}$) in quadrature to obtain the total baryonic rotation curve

$$V_{\rm b} = \left[V^2_{\rm disk,*} + V^2_{\rm bulge,*} + V^2_{\rm atom} + V^2_{\rm mol}\right]^{1/2}. \quad (5)$$

5.2. Parameterized rotation curves of the dark-matter halos

Although we have now calculated the rotation curves of all dynamically important baryonic components, and we can therefore, together with our observed rotation curves, directly determine the rotation curves of the dark-matter halos, we will also perform rotation-curve mass decompositions using two different parameterizations of the dark-matter halo; either using a pISO or a NFW halo model.

The pISO-halo is parameterized by its central density (ρ_0) and its core radius ($R_{\rm C}$), with a rotation curve following from

$$V^{\rm pISO}_{\rm DM}(R) = \sqrt{4\pi G\rho_0 R^2_{\rm C}\left[1 - \frac{R_{\rm C}}{R}\arctan\left(\frac{R}{R_{\rm C}}\right)\right]}. \quad (6)$$

[6] Groningen Image Processing SYstem.

[7] In fact, it is the square of the rotation speed that is negative. The rotation velocity itself is imaginary, but is by convention denoted as negative.

The NFW halo is parameterized by its mass ($\mathcal{M}^{\rm halo}_{200}$) within the virial radius (R_{200}; defined as the radius of a sphere of mean interior density 200 times the critical density $\rho_{\rm crit} = 3H_0^2/8\pi G$) and its concentration (C) as defined in Navarro et al. (1997). The rotation curve is given by

$$\frac{V^{\rm NFW}_{\rm DM}(R)}{V_{200}} = \sqrt{\frac{1}{X}\frac{\ln(1+CX) - (CX)/(1+CX)}{\ln(1+C) - C/(1+C)}}, \quad (7)$$

where V_{200} is the circular velocity at R_{200} and $X = R/R_{200}$.

The pISO is an ad hoc form of the density distribution, fitted to the observed rotation curves to describe the dark-matter distribution. The NFW halo, on the other hand, is a prediction from dark-matter-only simulations, and therefore predicts how the halo looked like prior to the galaxy forming in it. In principal, the baryons in the forming galaxy could affect the distribution of the dark matter. However, as discussed in Sect. 8.3, several processes may occur that could both contract and expand the halo, and even effectively leaving it unmodified.

5.3. Unique rotation-curve mass decompositions (Case I)

Using the baryonic rotation curves derived in Sect. 5.1, we determine the dark-matter distribution in our galaxy sample taking an approach similar to traditional rotation-curve mass decompositions (e.g., van Albada et al. 1985; Carignan & Freeman 1985; Begeman et al. 1991). Assuming the Hα and HI rotation curves trace the circular speed ($V_{\rm c}$) of the composite potential, the circular speed of the dark-matter component ($V_{\rm DM}$) is calculated from

$$V^2_{\rm DM} = V^2_{\rm c} - V^2_{\rm b}. \quad (8)$$

Therefore, our data provide $V_{\rm DM}$ directly such that we calculate a unique, dynamically constrained, non-parametric dark-matter rotation curve for each galaxy in our sample.

The derived $V_{\rm DM}$, calculated from Eq. (8), are plotted in the Atlas figures. In Fig. 10 we plot the baryonic ($V_{\rm b}$), dark matter ($V_{\rm DM}$) and observed total rotation curves ($V_{\rm c}$) in the same figure. What can already be noted from this figure is that the contribution from the dark-matter rotation curve to the observed total rotation curve is in general dominant at most radii. This is not unexpected given the result in Paper V (and Sect. 6 of this paper), where we found that these galaxies are submaximal.

We use the GIPSY task ROTMAS to model the dark-matter rotation curves via a pISO or NFW-halo parameterization. The baryonic and dark-matter rotation curves are added together in quadrature into a total rotation curve, matching the observed rotation curve using a minimum χ^2-fitting routine. Since all baryonic components are fixed, this is basically only fitting the two-parameter dark-matter-halo models to the measured dark-matter rotation curve. Each fitted halo is plotted in the Atlas and the fitted parameters are provided in Table 6.

5.4. Maximum-Υ_* rotation-curve decompositions (Case II)

Traditionally, without an independent measurement of Υ_*, rotation-curve mass decompositions have often been performed with the assumption of a maximum contribution from the stellar disk and bulge to the total potential (e.g., van Albada et al. 1985; Kent 1986; Broeils & Courteau 1997). This approach sets a lower limit to the contribution of the dark matter, often with the result that no dark matter is needed in the inner part of the galaxy. For comparison, we consider a maximum-Υ_* case here

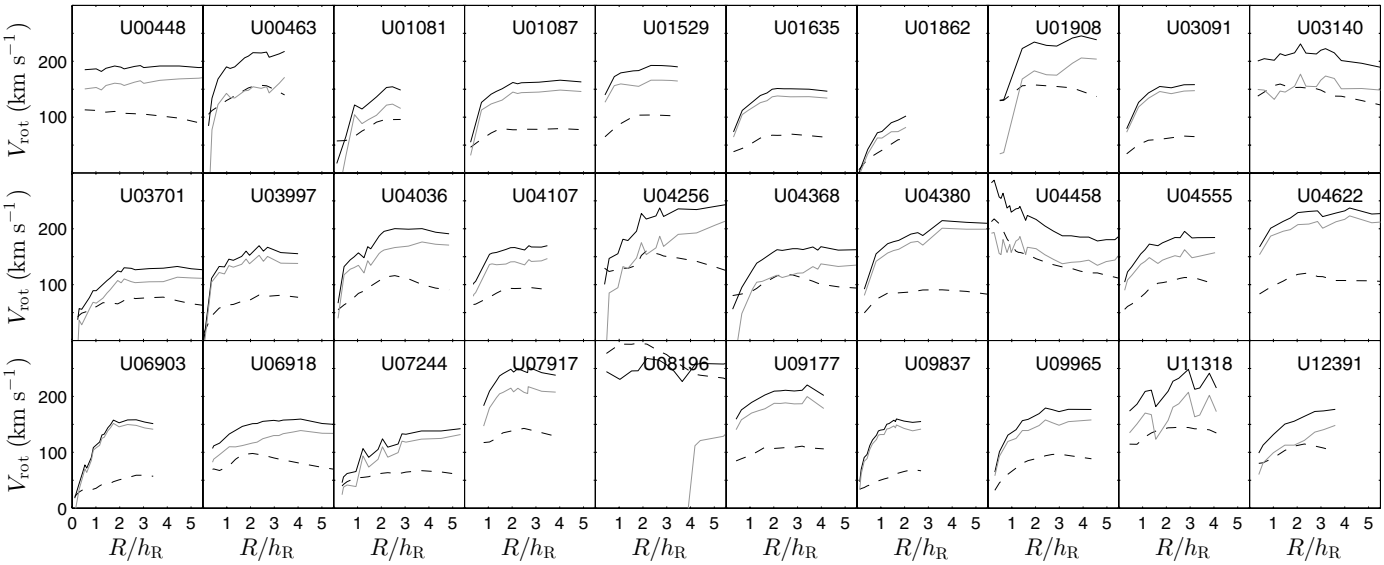

Fig. 10. Rotation curves: observed (solid black), baryonic (dashed black) and dark matter (solid gray).

as well. The fitting is performed using a pISO or NFW halo with $\overline{\Upsilon_*}$ scaled up by a factor f_* (listed in Table 6). This factor, which is usually (but not always exactly) the same for the NFW and pISO halo models, is forced to be as high as allowed by the observed rotation curve, which effectively sets $V_{\rm b}$ close to $V_{\rm c}$ in the inner region of the galaxies. As for Case I, we enforce $\overline{\Upsilon_*}$ of the stellar bulge and disk to be equal.

To enforce these galaxies to be maximal, $\overline{\Upsilon_*}$ must on average be 3.6 times what was measured in Sect. 3.4, with a range in f_* from 1.6 (UGC 7244)[8] to 8.1 (UGC 6903), and with 70% of the galaxies having values of f_* between 2.1 and 4.6. A detailed discussion on this difference between our measured Υ_* and what is found for the maximum-Υ_* cases, and the effects of our results on stellar-population models, will be the subject of a forthcoming paper. We find the ratio between the maximum-Υ_* baryonic rotation curve and the measured total rotation curve at $R = 2.2h_R$ ($\mathcal{F}_{\rm b,max}^{2.2h_R}$) to range between 0.66 (UGC 7244) and 1.03 (UGC 4622), with an average value of 0.92 ± 0.08 (std)[9]. As expected (see Sect. 8.1), this is somewhat higher than the 0.85 ± 0.10 found by Sackett (1997). Table 4 includes $\mathcal{F}_{\rm b,max}^{2.2h_R}$ for the individual galaxies.

5.5. Comparison of χ^2 for the various cases

Here we make a relative comparison between the quality of the decompositions of the modeled dark-matter+baryonic rotation curves to the observed rotation curves when using either our nominal-Υ_* (submaximal) case (Case I; Sect. 5.3) or the maximal-Υ_* case (Case II; Sect. 5.4). For both cases, we have used two different models (pISO and NFW) for the dark-matter halo. We calculate the χ^2 values from a weighted quadrature sum of the differences between the observed and modeled rotation velocities. Due to complex and non-Gaussian errors we will not consider the reduced χ^2 values, but instead look at relative values.

We find that the nominal-Υ_* fits produce significantly better χ^2 results than the maximum-Υ_* fits. The nominal-Υ_* case with a pISO dark-matter halo (Case Ia) gives on average the best fit with the lowest χ^2. The average relative difference in χ^2 between Case Ia ($\chi^2_{\rm pISO}$) and Case Ib ($\chi^2_{\rm NFW}$), normalized to $\chi^2_{\rm pISO}$, is $(\chi^2_{\rm NFW} - \chi^2_{\rm pISO})/\chi^2_{\rm pISO} = 0.46$. For the maximum-$\Upsilon_*$ cases (Case IIa,b) we find the relative differences in χ^2 compared to Case Ia to be $(\chi^2_{\rm pISO,II} - \chi^2_{\rm pISO})/\chi^2_{\rm pISO} = 1.42$ and $(\chi^2_{\rm NFW,II} - \chi^2_{\rm pISO})/\chi^2_{\rm pISO} = 2.36$.

Figure 11 shows the distribution of relative differences between the pISO and NFW-halo models (nominal-Υ_* and maximum-Υ_* case separately). Even though Case Ia on average results in a slightly better fit than Case Ib, and Case IIa is a better fit than Case IIb, the differences are not significant as indicated by the relative χ^2-values. This inability to differentiate between a pISO and a NFW-halo parameterization of the observed data was also seen for luminous galaxies in THINGS (de Blok et al. 2008). However, for low-luminosity galaxies, they find that a pISO parameterization better fits the data.

We find no strong correlations between how well the different models fit the data and global properties of the galaxies (see Martinsson 2011).

Table 4. Baryonic mass fraction at $R = 2.2h_R$.

UGC	$\mathcal{F}_{\rm b}^{2.2h_R}$	$\mathcal{F}_{\rm b,max}^{2.2h_R}$	UGC	$\mathcal{F}_{\rm b}^{2.2h_R}$	$\mathcal{F}_{\rm b,max}^{2.2h_R}$
448	0.57 ± 0.09	0.94	4368	0.72 ± 0.06	1.01
463	0.72 ± 0.11	0.96	4380	0.46 ± 0.08	0.88
1081	0.63 ± 0.06	0.89	4458	0.68 ± 0.21	0.90
1087	0.48 ± 0.08	0.85	4555	0.59 ± 0.07	0.97
1529	0.55 ± 0.06	0.98	4622	0.52 ± 0.12	1.03
1635	0.45 ± 0.07	0.88	6903	0.34 ± 0.17	0.80
1862	0.60 ± 0.06	0.91	6918	0.64 ± 0.17	0.97
1908	0.68 ± 0.10	0.88	7244	0.56 ± 0.14	0.66
3091	0.41 ± 0.10	0.93	7917	0.56 ± 0.07	0.97
3140	0.68 ± 0.09	0.92	8196	1.09 ± 0.05	1.09
3701	0.55 ± 0.14	0.79	9177	0.51 ± 0.09	1.03
3997	0.48 ± 0.12	0.95	9837	0.44 ± 0.08	0.89
4036	0.58 ± 0.08	0.96	9965	0.53 ± 0.09	0.94
4107	0.56 ± 0.09	1.00	11 318	0.66 ± 0.10	1.03
4256	0.73 ± 0.16	0.93	12 391	0.70 ± 0.09	0.94

[8] When excluding UGC 8196; see Sect. 6.
[9] As in Sect. 6, we exclude UGC 1862.

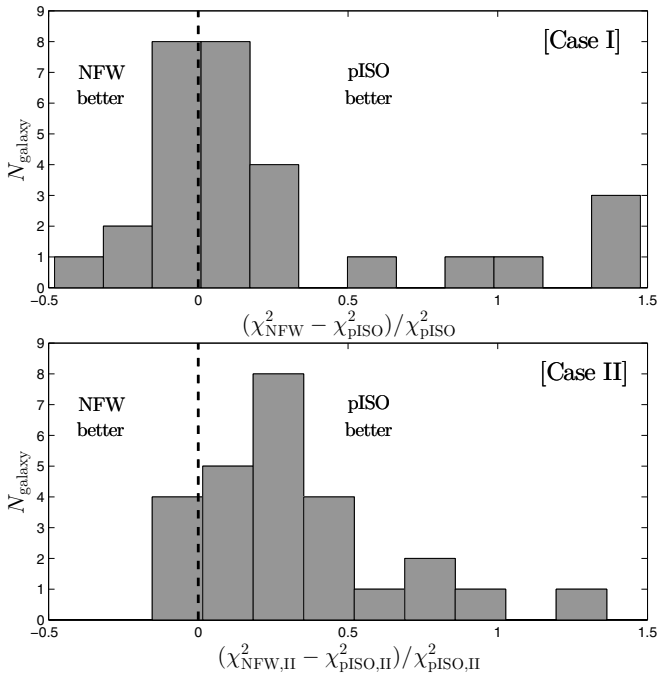

Fig. 11. Relative difference in calculated χ^2 between the fits using NFW and pISO dark-matter halos. Upper and lower row show the differences in the nominal-Υ_* and maximum-Υ_* case, respectively.

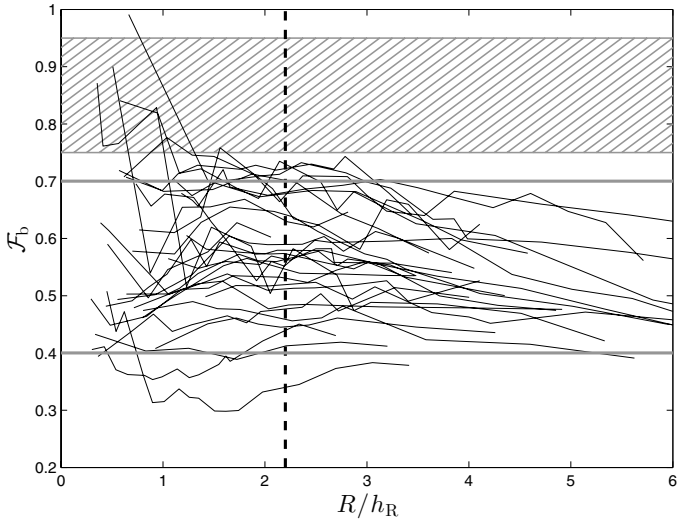

Fig. 12. Baryonic mass fraction of all galaxies except UGC 8196 as a function of radius. As in Fig. 13, the shaded area shows $0.75 \leq \mathcal{F}_{\rm b} \leq 0.95$, the vertical dashed line $R = 2.2h_R$, and we exclude measurements within $R = R_{\rm bulge}$. The two thick gray horizontal lines indicate the range $\mathcal{F}_{\rm b} = 0.4$–$0.7$.

6. The dynamical importance of the baryons

In this section we investigate the ratio $\mathcal{F}_{\rm b} = V_{\rm b}/V_{\rm c}$, or the "baryonic maximality", for the galaxies in our sample. This ratio is a measure of the dynamical importance of the baryons in the galaxy. We calculate $\mathcal{F}_{\rm b}$ as a function of radius for all galaxies. These are plotted together in Fig. 12 and separately in Fig. 13.

We find that the galaxies have a rather constant value of $\mathcal{F}_{\rm b}$ with radius, ranging in amplitude between ~0.4–0.7 for the sample of galaxies (Fig. 12). The constancy of $\mathcal{F}_{\rm b}$ arises due to an increasing contribution from the atomic gas at larger radii where the contribution from the stellar disk is declining (Fig. 3). This result has a consequence for the measurement of the maximality: with the assessment of the maximality of a galaxy using $\mathcal{F}_{\rm b}$, it is of less importance to measure exactly at the radius $R^{\rm disk}_{\rm max} \approx 2.2h_R$ where the rotation curve of the stellar disk peaks.

In Fig. 14, we plot the measured $\mathcal{F}_{\rm b}$ at $R = 2.2h_R$ ($\mathcal{F}_{\rm b}^{2.2h_R}$; tabulated in Table 4) versus $B-K$ color, absolute K-band magnitude, and central disk surface brightness. We confirm the result in Paper V that all our galaxies are submaximal, with a range in $\mathcal{F}_{\rm b}^{2.2h_R}$ of 0.34–0.73, equivalent to ~10–50% of the total mass within $2.2h_R$ being baryonic. On average, after rejecting UGC 1862 which has no measurement of $V_{\rm c}$ at $2.2h_R$, $\langle \mathcal{F}_{\rm b}^{2.2h_R} \rangle$ =0.57±0.07 (std). This result is consistent with what was found by Bottema (1993) and Kregel et al. (2005), and based on the correlations with M_K and $\mu^i_{0,K}$ seen in Fig. 14, we conclude that small differences in the mean may be due to differences in the galaxy samples. However, also note that both Bottema (1993) and Kregel et al. (2005) measured the disk mass fraction, excluding the contribution from the stellar bulge (see discussion in Sect. 8.1).

In Paper V we found that more luminous and redder galaxies are closer to be maximal, but with little dependence on both central surface brightness and morphology. Here, we again find a weak trend of larger $\mathcal{F}_{\rm b}^{2.2h_R}$ for more luminous galaxies, but also for galaxies with higher central disk surface brightness. Weighted linear fits give $\mathcal{F}_{\rm b}^{2.2h_R} = (0.58 \pm 0.09) - (0.04 \pm 0.02)(M_K + 24)$ and $\mathcal{F}_{\rm b}^{2.2h_R} = (0.56 \pm 0.09) - (0.08 \pm 0.03)(\mu^i_{0,K} - 18)$. Unlike the result in Paper V we find no correlation with color, and in contrast to Herrmann & Ciardullo (2009), who had a similar range of morphologies, we find little dependence on morphological type.

As can be seen in Fig. 13, UGC 8196 appears to be "supermaximal", $V_{\rm b} > V_{\rm c}$, which is a non-physical result. This might be either due to an overestimation of Υ_* or an underestimation of $V_{\rm c}$. The derived Υ_* is indeed the highest in the sample. An overestimation of Υ_* could be due to an incorrect assumption about the SVE (α), the thickness of the disk (h_z), or its vertical mass distribution (k). As seen in the Atlas, the measured σ_z of UGC 8196 is extremely high for a disk in the inner region compared to the other disks in our sample, and instead more comparable to other bulges. This could be an indication that we are not measuring the velocity dispersion of the disk and that Eq. (1) is therefore invalid. If we extend $R_{\rm bulge}$ out to 15″, excluding the measurement at this radius, we find a Υ_* that is only 80% of the adopted value, resulting in $\mathcal{F}_{\rm b} = 0.98$ at $2.2h_R$; much higher than all other galaxies, but physically possible. UGC 8196 has a rather low inclination of 16.°1. If this inclination is instead 2.°7 lower (3σ), this would result in a rotation curve with a larger amplitude, making the Υ_* and $\mathcal{F}_{\rm b}$ estimates physically possible, and resulting in $\mathcal{F}_{\rm b} = 0.91 \pm 0.05$ at $2.2h_R$. However, due to the uncertainties in what is causing the non-physical result, we have decided to exclude UGC 8196 from our analysis and results.

7. The dark-matter-halo rotation curve

From our unique rotation-curve mass decompositions in Sect. 5.3, we have measured the dark-matter rotation curves for all galaxies. In this section, we will investigate the shape of these dark-matter rotation curves, and look at how well our parameterized halo models fit the data. We compare the resulting parameters in relation to one another and with respect to results from ΛCDM simulations.

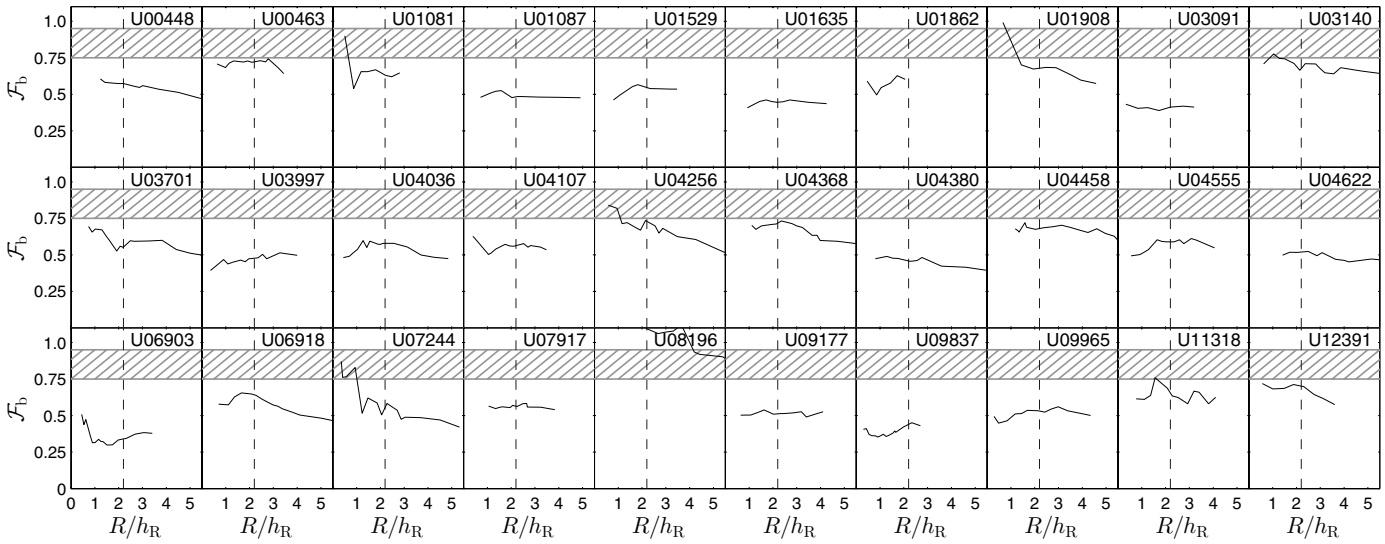

Fig. 13. Baryonic maximality of individual galaxies as a function of radius. Measurements within $R = R_{bulge}$ have been omitted. The shaded area shows $0.75 \leq \mathcal{F}_b \leq 0.95$, the defined fraction (Sackett 1997) a maximum disk should have at $R = 2.2h_R$ (vertical dashed line).

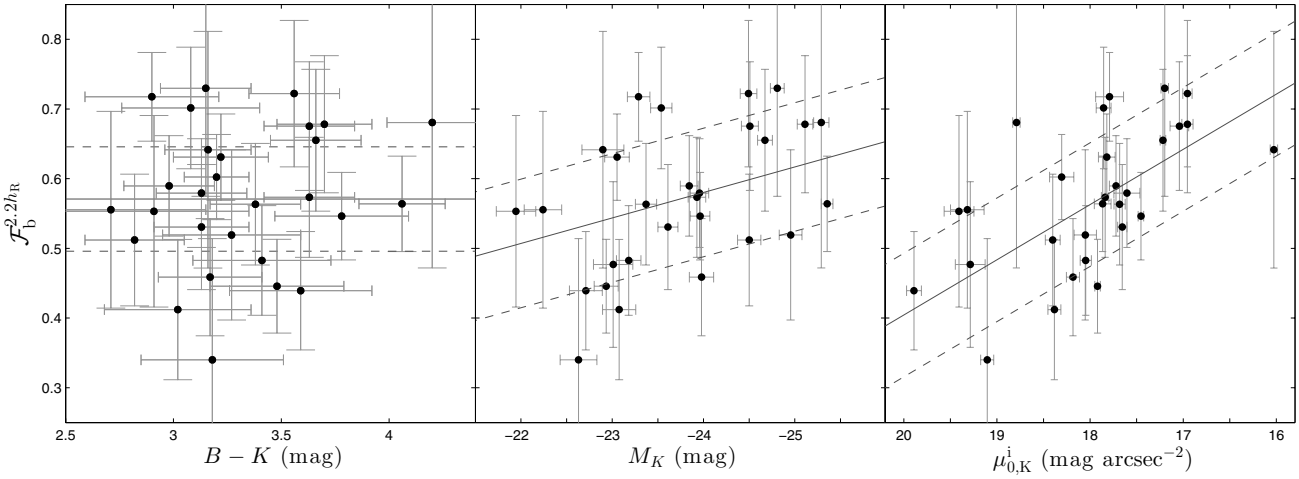

Fig. 14. Baryonic mass fraction measured at $2.2h_R$ versus $B-K$ color (*left*), absolute K-band magnitude (*middle*), and central surface brightness of the disk (*right*). Black dots with gray errorbars indicate measurements from individual galaxies. Black lines are linear fits to the data, showing that more luminous and higher-surface brightness galaxies have larger $\mathcal{F}_b^{2.2h_R}$. The lines in the *left panel* show the weighted average and scatter.

For individual galaxies, we find in general no significant difference between the quality of the pISO and NFW fits to our measurements of V_{DM}; however, for our entire sample, the pISO model tends to result in a lower χ^2 (Sect. 5.5). To further investigate any general differences between the shape of the pISO and NFW parameterization with respect to our data, we consider the V_{DM} measurements of all galaxies simultaneously. In Fig. 15, we plot all the measured dark-matter rotation curves in the same panel with the radius normalized to either R_C or $R_s = R_{200}/C$, and the velocity normalized to either V_∞^{pISO} or V_{max}^{NFW} (the velocity of the NFW rotation curve at ∼2.2 R_s). Measurements of V_{DM} inside of $R = 5''$ have been excluded. On top of the measured points, we plot the parameterized rotation curves, which were fitted to each individual galaxy separately.

The left panel of Fig. 15 shows all measured points compared to the pISO case. In general, the data follow the fits well, with a weighted scatter of 0.024 for all data points. The right panel shows the same as the left panel, except it adopts the NFW-halo parameterization. The weighted scatter of all data points compared to the NFW model is 0.027; only slightly larger than for the pISO case. In Martinsson (2011) we investigated how well the dark-matter rotation curves are fitted for galaxies with low or high $\mu^i_{0,K}$ and $\mathcal{F}_b^{2.2h_R}$. For both the pISO and the NFW cases, we find no dependencies on these parameters. In a few galaxies with a steep rise in the inner region of the dark-matter rotation curve (e.g., UGC 448 and UGC 3140; see Atlas), the NFW-halo model fails to follow the inner steep rise. For these galaxies, the pISO model is a better fit. The inner regions exhibit in general the largest residuals, with a scatter of 0.056 and 0.068 within $R = 0.9\ R_C$ and $R = 0.1\ R_s$ for the pISO and NFW fits, respectively. The measured V_{DM} are here systematically lower than the fitted NFW rotation curve. In the outer regions the NFW rotation curve begins to decline at $R/R_s \approx 2$, which is reached at a smaller radius in galaxies with a steep inner rise in the dark-matter rotation curve, whereas the observed dark-matter rotation curve stays flat. However, note that our measured dark-matter rotation curves are rather uncertain at both small and large R; uncertainties in the dynamical mass of the bulge and the possible

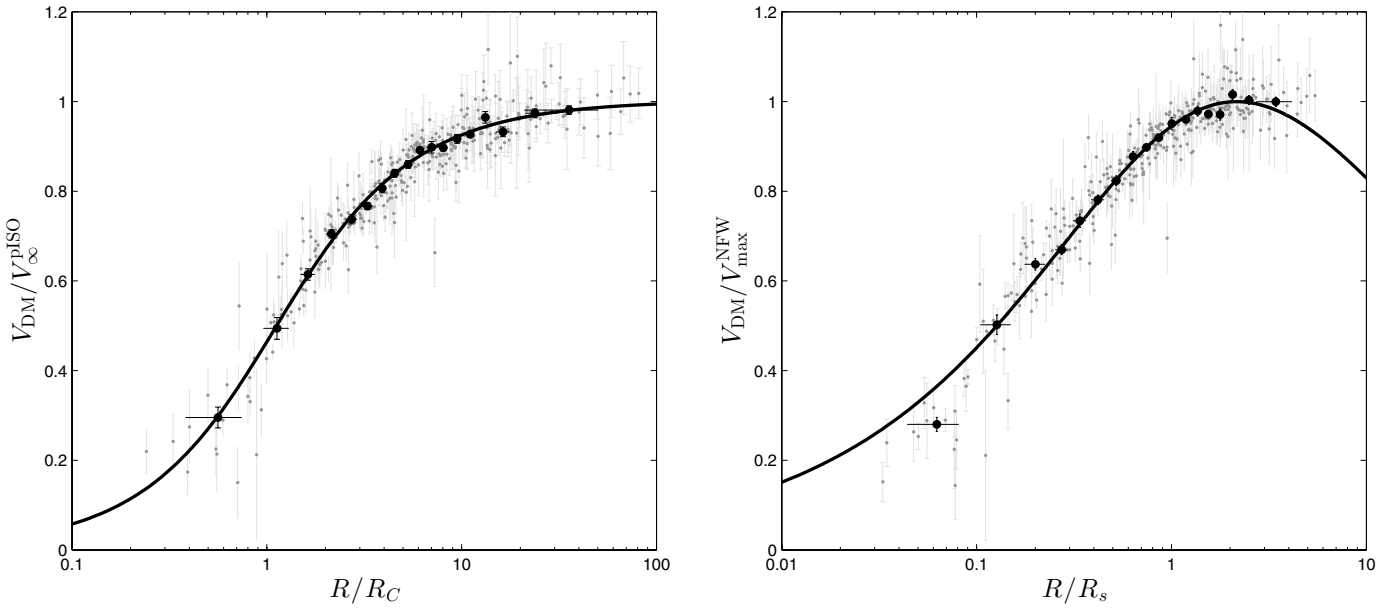

Fig. 15. All measured dark-matter rotation velocities plotted together and compared to the fitted models. *Left panel*: comparison to the pISO model. R and $V_{\rm DM}$ have been normalized with $R_{\rm C}$ and $V_{\infty}^{\rm pISO}$, respectively. *Right panel*: comparison to the NFW-halo model. Here, R and $V_{\rm DM}$ have been normalized with $R_{\rm s}$ and $V_{\rm max}^{\rm NFW}$, respectively. Gray points with light gray errorbars indicate individual $V_{\rm DM}$ measurements. The black filled circles show averages in radial bins containing 20 measurements each.

effect of adiabatic contraction may affect the inner measurements of $V_{\rm DM}$, while the outer measurements may be systematically in error for individual galaxies because we intentionally keep the observed rotation curves flat by introducing a linear inclination warp of the HI disk to "force" these galaxies onto the Tully-Fisher relation (Martinsson 2011).

7.1. Derived parameters

As a consequence of the submaximality of our galaxies, the dark-matter rotation curves rise quickly at small radii, with parameter values that differ significantly from what is found for the maximum-Υ_* cases. This behavior, and the inferred dark-matter distributions, can be compared to what has been found from numerical simulations.

In Fig. 16, we plot the two halo parameters from the dark-matter-halo fits against each other, for both the pISO and the NFW-halo parameterization. In addition to the nominal-Υ_* case, we also include the results from the maximum-Υ_* case for comparison. For the pISO fits, we find a strong correlation between ρ_0 and $R_{\rm C}$. This is expected given the strong covariance between the two parameters as seen in the formula $V_{\infty}^{\rm pISO} = \sqrt{4\pi G \rho_0 R_{\rm C}^2}$ and the relatively small range in dynamical masses of our galaxy sample, as indicated with the two lines in the figure showing constant $V_{\infty}^{\rm pISO}$. The spread along these lines is not explained by the measurement errors. We find that the maximum-Υ_* fits have larger $R_{\rm C}$ and smaller ρ_0. This is expected since the maximum-Υ_* decompositions result in a much shallower rise of the dark-matter rotation curve. For the NFW halo, we again find a correlation between the two parameters with a lower concentration for larger halo masses, and with the maximum-Υ_* case having much lower concentration than the nominal-Υ_* case. The median values and ranges of the fitted parameters are presented in Table 5.

We have compared our results with parameter values found by de Blok et al. (2008). Excluding the four least massive galaxies in their sample (leaving 13 galaxies similar to those in the PPak sample), and looking at the models with fixed stellar mass-to-light ratios derived using a Kroupa IMF, we find rather similar parameter values. However, there are some differences. In the case of fitting a pISO model, the core radius of our fitted halos are on average ~50% smaller, but with a ~65% larger central density. When fitting a NFW-halo model, the median value of the concentration parameter in the 13 galaxies from de Blok et al. (2008) is similar to what we find ($C = 9$ and $C = 11$, respectively), but with a much larger scatter.

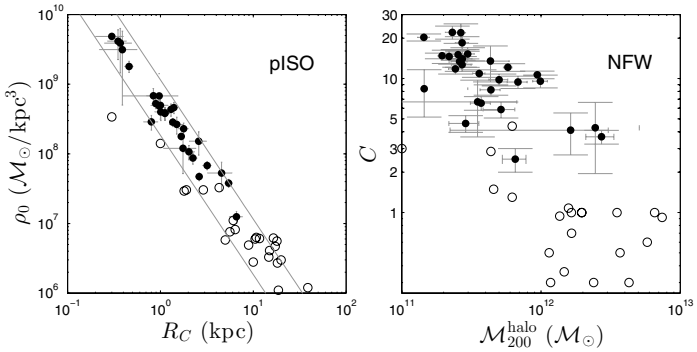

Fig. 16. *Left*: ρ_0 versus $R_{\rm C}$. The two gray lines indicate $V_{\infty}^{\rm pISO}$ = 100 km s^{-1} and 250 km s^{-1}; the range of $V_{\infty}^{\rm pISO}$ for the nominal-Υ_* case. *Right*: relation between the concentration (C) and mass ($\mathcal{M}_{200}^{\rm halo}$) of the NFW-halo profile. Filled and open circles indicate nominal-Υ_* and maximum-disk fits, respectively.

7.2. Comparison to cosmological simulations

Bullock et al. (2001) studied dark-matter-halo density profiles in a high-resolution N-body simulation with ΛCDM cosmology. They found similar values and scatter compared to what we find here for the nominal-Υ_* case, with $C \approx 10-20$ in our mass range. The negative slope in the $\mathcal{M}_{200}^{\rm halo} - C$ relation can be seen clearly

Table 5. Median dark-matter-halo parameters.

	pISO				NFW			
	ρ_0 (10^8 $M_\odot$/kpc^3)		R_C (kpc)		C		$\mathcal{M}_{200}^{halo}$ (10^{11} $M_\odot$)	
Case-I	**3.3**	(0.47–32)	**1.3**	(0.39–4.6)	**11**	(4.1–18)	**1.0**	(0.59–4.4)
Case-II	**0.06**	(0.03–0.30)	**10**	(1.9–18)	**1.0**	(0.30–3.0)	**4.1**	(1.2–16)

Notes. Parentheses give ranges of parameter values for 80% of the galaxies.

in their Fig. 4 (distinct halos) and, even stronger, in their Fig. 5 (subhalos). The concentrations found for our maximum-Υ_* fits are much lower than for the nominal-Υ_* case, with typical values around or lower than $C = 1$. As discussed by de Blok et al. (2008), the value of C indicates the amount of collapse the halo has undergone, where $C = 1$ indicates no collapse and a value of $C < 1$ is an unphysical result in the context of cold dark matter. There is also a lack of correlation between $\mathcal{M}_{200}^{halo}$ and C for the maximum-Υ_* case. This result implies that for the galaxies in our sample, a maximum-Υ_* solution is inconsistent with results from simulated NFW halos. However, for the nominal-Υ_* case, the shapes of our inferred dark-matter rotation curves are well fit with parameters in agreement with what has been found from dark-matter-only simulations. Furthermore, this result suggests that the baryonic matter in our sample of submaximal galaxies may have only a minor effect on the dark-matter distribution.

8. Discussion

In the previous sections, we presented results on the distribution of the baryonic matter and quantified the baryonic maximality. We derived the dark-matter rotation curves and compared results from the unique rotation-curve mass decompositions with the maximum-disk hypothesis. In this section, we further discuss the galaxy disk and total baryonic maximality (Sect. 8.1) and the arguments for and against maximal and submaximal disks (Sect. 8.2). We briefly discuss the difficulties in distinguishing between the pISO and NFW parameterizations of the dark-matter rotation curves (Sect. 8.3). Finally, we include a discussion on our adopted assumptions and the introduced uncertainties in our analysis (Sect. 8.4).

8.1. Disk and baryonic maximality

The "maximality" of a galaxy is often assessed on the basis of the stellar-disk mass fraction, $\mathcal{F}_{disk,*} = V_{disk,*}/V_c$, traditionally measured at $2.2h_R$, and including the total mass associated with the stellar disk (e.g., with a molecular-gas component assumed to have the same distribution as the stars). The most commonly adopted definition of a maximum disk was provided by Sackett (1997), who proposed $\mathcal{F}_{disk,*}^{2.2h_R} = 0.85 \pm 0.10$ to be an appropriate definition for maximum disks in galaxies of Hubble type similar to the Milky Way (Sb and Sc). The Sackett definition allows for small contributions from a bulge and a dark-matter halo with a non-hollow core, as well as a contribution from the HI gas, but the literature studies on which this number was based usually incorporated the molecular gas component in the stellar-disk mass distribution implicitly. In this paper, instead, we are considering the total baryonic mass fraction. In our analysis of the maximum-Υ_* case in Sect. 5.4, we define a galaxy to be maximal if $\mathcal{F}_b \sim 1$ in the inner region of the galaxy, keeping the contribution from the dark-matter halo minimal. We still compare our measured $\mathcal{F}_b^{2.2h_R}$ values with the definition of a maximum disk in Sackett (1997), but note that in general $\mathcal{F}_b^{2.2h_R} \geq \mathcal{F}_{disk,*}^{2.2h_R}$. This is certainly true for all galaxies in our sample. Thus, for our definition of the baryonic maximality, the fraction should be larger than the Sackett definition and closer to one. Indeed, in Sect. 5.4 we found that for the maximum-Υ_* case, calculated by maximizing the masses of the stellar bulges and disks as much as possibly allowed by the observed rotation curves, we measure an average and scatter of $\langle \mathcal{F}_{b,max}^{2.2h_R} \rangle = 0.92 \pm 0.08$. If we instead calculate the sample average of the ratio between the scaled stellar disk and the observed rotation curve at $2.2h_R$, we find it to be 0.84 ± 0.09, similar to what Sackett (1997) found. If we include the molecular gas into the stellar disk we get an average fraction of 0.87.

The sample average of $\mathcal{F}_b^{2.2h_R}$ found in this paper, $\langle \mathcal{F}_b^{2.2h_R} \rangle = 0.57 \pm 0.07$, is larger than what we found for the same sample of galaxies using a different approach in Paper V, $\langle F_{max}^{disk} \rangle = 0.47 \pm 0.08$. Although we are using the same sample of galaxies here and in Paper V, the maximality measurements presented are different in several ways. Values of F_{max}^{disk} presented in Paper V were based on the central vertical velocity dispersion of the disk stars ($\sigma_{z,0}$), excluding the bulge by extrapolating the fitted exponential increase of σ_z to the center. However, here $\mathcal{F}_b^{2.2h_R}$ is a measure of the baryonic maximality, with the stellar bulge included. We therefore expect $\mathcal{F}_b^{2.2h_R} > F_{max}^{disk}$. The difference between the two is dependent on B/D; the generally small bulges in our galaxy sample, with the average bulge contributing ~2% to the total rotation curve at $2.2h_R$, leads to an average difference of 0.02 between $\mathcal{F}_b^{2.2h_R}$ and F_{max}^{disk}. A fundamental procedural difference in the calculation of $\mathcal{F}_b^{2.2h_R}$ and F_{max}^{disk} is that the former is directly tied to the observed surface brightness profile of each galaxy, while in Paper V we instead used only one extrapolated value of the central stellar velocity dispersion. In Paper VI, we found that many galaxies have measured velocity dispersions in the outer disk which are larger than what is expected for an exponential decline. Therefore, it is possible that there is a systematic error introduced, such that the data points at larger radii lower the central velocity dispersion of the fit. However, the inner points are in general well fit by an exponential decline, with little influence from the outer data points which have larger errors. Thus, any systematic error should be small. To conclude, both random and systematic differences are expected between F_{max}^{disk} and $\mathcal{F}_b^{2.2h_R}$ due to differences in the methodology of deriving these quantities, and because these are intrinsically two different quantities.

8.2. Submaximal versus maximal disk

Related to the maximality discussed above, we will here discuss arguments for both submaximal and maximal-disk cases. It has been pointed out (e.g., by van Albada & Sancisi 1986) that there are several arguments to support the idea that disks in spiral galaxies are maximal. For example, the simplest way to explain why fitting a maximum disk works is that the disks actually are close to maximum. It has frequently been shown that the dynamical mass distribution follows the light distribution in the inner regions of galaxies (e.g., Kent 1986; Sancisi 2004; Noordermeer et al. 2007; Swaters et al. 2011; Fraternali et al. 2011), with a contribution from the stellar mass that can be scaled up to fully explain the shape of the inner part of the rotation curve within the radius typically reached by optical rotation curves. It has also been found that features in the rotation curve can be seen in the

Table 6. Parameterized dark-matter-halo parameters.

	Nominal-Υ_* (Case Ia & Ib)						Maximum-disk (Case IIa & IIb)					
			pISO		NFW		pISO			NFW		
UGC	$\overline{\Upsilon_*}$	R_Υ	R_C	$\log(\rho_0)$	C	$\log(\mathcal{M}_{200}^{halo})$	f_*^{iso}	R_C	$\log(\rho_0)$	f_*^{nfw}	C	$\log(\mathcal{M}_{200}^{halo})$
	$(M_\odot/L_{\odot,K})$	(h_R)	(kpc)	$(M_\odot\,kpc^{-3})$		$(M_\odot)$		(kpc)	$(M_\odot\,kpc^{-3})$			$(M_\odot)$
448	0.31 ± 0.21	1.5 ± 0.1	0.35 ± 0.08	9.62 ± 0.20	18.5 ± 2.0	11.43 ± 0.05	3.1	10.5	6.78	3.1	1.1	12.20
463	0.29 ± 0.17	1.3 ± 0.1	1.00 ± 0.21	8.70 ± 0.16	14.1 ± 1.9	11.44 ± 0.07	2.2	1.8	7.47	2.1	0.4	12.17
1081	0.40 ± 0.16	1.2 ± 0.1	1.75 ± 0.67	8.08 ± 0.25	6.7 ± 3.0	11.54 ± 0.40	2.2	1.9	7.48	2.2	1.5	11.66
1087	0.32 ± 0.13	0.9 ± 0.1	1.12 ± 0.14	8.58 ± 0.09	12.7 ± 1.4	11.43 ± 0.07	3.4	2.9	7.48	3.4	2.9	11.64
1529	0.29 ± 0.16	1.2 ± 0.1	0.37 ± 0.12	9.59 ± 0.27	22.1 ± 2.5	11.36 ± 0.05	3.7	5.0	6.76	3.7	10.0	10.22
1635	0.26 ± 0.12	1.1 ± 0.1	0.89 ± 0.08	8.72 ± 0.07	14.8 ± 0.7	11.29 ± 0.03	4.2	1.0	8.15	4.8	3.0	11.00
1862	0.56 ± 0.29	0.9 ± 0.1	0.80 ± 0.14	8.46 ± 0.10	8.4 ± 3.2	11.16 ± 0.46	2.6	0.3	8.53	2.6	16.0	9.61
1908	0.26 ± 0.18	1.3 ± 0.2	4.56 ± 1.35	7.72 ± 0.19	4.3 ± 2.3	12.39 ± 0.46	2.0	16.5	6.79	2.0	1.0	12.82
3091	0.23 ± 0.10	0.8 ± 0.2	1.12 ± 0.13	8.59 ± 0.09	13.4 ± 1.2	11.42 ± 0.06	6.2	5.6	6.88	5.9	0.9	12.13
3140	0.33 ± 0.14	1.1 ± 0.1	0.39 ± 0.17	9.50 ± 0.36	15.3 ± 1.7	11.47 ± 0.05	2.1	18.2	6.43	2.1	0.3	12.63
3701	0.85 ± 0.40	1.0 ± 0.1	2.62 ± 0.24	7.67 ± 0.06	4.6 ± 0.7	11.46 ± 0.11	2.2	6.4	6.91	2.2	1.3	11.79
3997	0.45 ± 0.19	0.8 ± 0.1	1.01 ± 0.14	8.60 ± 0.11	11.8 ± 1.0	11.39 ± 0.05	5.0	–	–	5.0	–	–
4036	0.29 ± 0.11	1.2 ± 0.1	1.50 ± 0.25	8.42 ± 0.12	9.8 ± 1.0	11.70 ± 0.07	3.2	15.0	6.61	3.2	0.5	12.57
4107	0.28 ± 0.14	1.1 ± 0.1	0.97 ± 0.12	8.69 ± 0.09	14.6 ± 1.7	11.34 ± 0.07	4.1	–	–	4.1	–	–
4256	0.15 ± 0.19	1.0 ± 0.1	5.43 ± 0.49	7.58 ± 0.06	3.7 ± 0.4	12.43 ± 0.10	3.0	18.0	6.75	3.0	0.9	12.87
4368	0.57 ± 0.34	1.5 ± 0.1	2.24 ± 0.25	7.94 ± 0.08	6.6 ± 0.8	11.57 ± 0.07	2.1	14.7	6.52	2.1	0.7	12.22
4380	0.27 ± 0.09	0.7 ± 0.2	1.78 ± 0.22	8.36 ± 0.09	9.4 ± 1.0	11.83 ± 0.07	4.3	17.2	6.67	4.3	0.6	12.76
4458	0.42 ± 0.24	1.1 ± 0.1	0.30 ± 0.10	9.69 ± 0.02	22.0 ± 3.7	11.42 ± 0.04	1.9	10.0	6.45	1.9	0.1	12.00
4555	0.35 ± 0.20	1.1 ± 0.1	0.84 ± 0.13	8.83 ± 0.12	15.1 ± 1.4	11.40 ± 0.05	3.1	10.0	6.45	3.1	0.3	12.07
4622	0.28 ± 0.17	1.2 ± 0.2	1.40 ± 0.14	8.67 ± 0.08	10.7 ± 0.7	11.97 ± 0.03	4.6	38.7	6.08	4.6	0.1	12.76
6903	0.24 ± 0.17	0.4 ± 0.1	3.19 ± 0.34	7.83 ± 0.06	4.1 ± 1.4	12.21 ± 0.38	8.1	6.1	7.05	8.1	1.0	12.22
6918	0.06 ± 0.24	1.2 ± 0.1	0.46 ± 0.05	9.26 ± 0.08	20.3 ± 1.2	11.16 ± 0.04	6.2	4.3	7.51	5.5	4.4	11.79
7244	0.41 ± 0.18	0.5 ± 0.1	6.60 ± 1.09	7.10 ± 0.08	2.5 ± 0.5	11.82 ± 0.08	1.6	10.8	6.80	1.6	1.0	12.29
7917	0.29 ± 0.33	1.5 ± 0.1	2.59 ± 0.55	8.18 ± 0.16	9.6 ± 1.0	12.00 ± 0.05	3.4	18.7	6.04	3.4	0.1	11.97
8196	0.94 ± 0.41	2.1 ± 0.2	15.50 ± 1.50	6.64 ± 0.05	1.0 ± 1.0	12.55 ± 0.13	1.0	15.5	6.64	1.0	1.0	12.55
9177	0.36 ± 0.26	1.3 ± 0.1	1.30 ± 0.14	8.64 ± 0.09	12.1 ± 0.8	11.76 ± 0.03	4.6	–	–	4.6	–	–
9837	0.32 ± 0.14	0.5 ± 0.1	1.68 ± 0.11	8.25 ± 0.05	8.2 ± 0.7	11.64 ± 0.07	8.0	8.9	6.69	8.0	0.5	12.06
9965	0.25 ± 0.12	0.9 ± 0.2	1.36 ± 0.11	8.45 ± 0.06	10.9 ± 0.7	11.56 ± 0.04	4.0	20.0	6.48	4.0	0.3	12.38
11 318	0.29 ± 0.20	1.2 ± 0.1	0.97 ± 0.58	8.83 ± 0.47	13.5 ± 4.0	11.64 ± 0.16	3.0	–	–	3.0	–	–
12 391	0.41 ± 0.19	1.2 ± 0.1	2.03 ± 0.31	8.03 ± 0.10	5.9 ± 0.8	11.71 ± 0.11	2.0	11.7	6.79	2.0	1.0	12.29

Notes. Table listing derived stellar mass-to-light ratios ($\overline{\Upsilon_*}$; Sect. 3.4), the effective radius at which $\overline{\Upsilon_*}$ was measured (R_Υ), fitted dark-matter-halo parameters (Sect. 5), and the scaling factors (f_*^{iso} & f_*^{nfw}) with which $\overline{\Upsilon_*}$ have to be multiplied to make the galaxy maximal.

light profile as well. However, these arguments in favor of a maximum disk can be disputed.

Even though the rotation curves of the galaxies in our sample can be decomposed rather convincingly using a maximum Υ_*, our submaximal-Υ_* cases result in significantly better fits (Sect. 5.5). Furthermore, in the context of Newtonian gravity, the extended, flat HI rotation curves require dark-matter halos to explain the non-declining outer part generally observed in spiral galaxies. If these observations indeed convince us of the existence of dark-matter halos, why should this dark matter be distributed in such a way that it is only required to explain the outer part of the rotation curves? With an all-over dominating dark-matter halo, the "conspiracy" (Bahcall & Casertano 1985) between the stellar disk and dark-matter halo to produce flat rotation curves weakens. Even though features in the observed rotation curve are often seen in the light profile, this only suggests that the gravitational potential of the visible stars or gas is non-negligible in the galaxy mid-plane; e.g., a bump in a non-dominant baryonic rotation curve that is added in quadrature to a smooth dominant dark-matter rotation curve may still be seen, especially in the inner regions where the baryons contribute most. We have two examples of this in our sample: UGC 4256 and UGC 6918 (see Atlas). Even though the rotation curves of these galaxies are dominated by V_{DM}, features in V_{mol} are still clearly seen in the observed rotation curves. Furthermore, the features seen in the rotation curves are often associated with non-axisymmetric structures such as spiral arms, i.e., perturbations on both velocity and surface brightness. This requires neither maximality nor submaximality.

A theoretical argument in favor of submaximal disks is presented in Amorisco & Bertin (2010). From constructed self-consistent models of nonspherical isothermal halos embedding a zero-thickness disk, they find a best-fit model that is significantly submaximal.

Observationally, one can infer that disk galaxies are submaximal given the lack of a surface-brightness dependence in the Tully-Fisher relation for a wide range of spiral galaxies (Zwaan et al. 1995; Courteau & Rix 1999; Courteau et al. 2003). Also barred galaxies, which are suspected to be close to maximal, show no offset from the Tully-Fisher relation. However, studies from kinematic observations have so far not reached a consensus. For example, Weiner et al. (2001) used fluid-dynamical models of gas flows in a barred galaxy to constrain its dynamical properties. They found that maximum-disk values are highly favored for this galaxy, and argued that the luminous matter dominates inside the optical radius of high surface brightness disk galaxies in general. Kranz et al. (2003) studied five high surface brightness late-type spiral galaxies using hydrodynamic gas simulations and draw the conclusion that high surface brightness galaxies possess maximal disks if their maximal

rotation velocities are larger than 200 km s^{-1}. If the maximal rotation velocity is less, the galaxies appear to have submaximal disks. Analyses of one barred, resonance-ring system (Byrd et al. 2006) and one gravitational-lens system (Dutton et al. 2011) indicate that these two galaxies are submaximal. However, in another lensed galaxy, Barnabè et al. (2012) found that the dark-matter fraction within 2.2 optical disk scale lengths (h_R) was only ∼28%, implying a maximum disk. Dutton et al. (2013) further investigated five gravitationally-lensed, bulge-dominated disk galaxies, and found that the disks of the galaxies are submaximal at $2.2h_R$, but due to their large bulges, these galaxies are still baryon dominated at this radius. Results from the kinematics of planetary nebulae in several nearby galaxies suggest that the maximality may depend on Hubble type (Herrmann & Ciardullo 2009). In conclusion, many different methods have resulted in many different results.

In addition to our own study, similar analysis of stellar-kinematic observations of normal spiral galaxies (e.g., Bottema 1993; Kregel et al. 2005; Herrmann & Ciardullo 2009) generally show that spiral galaxies are submaximal with disks that contribute ∼60 ± 10% to the observed rotation speed, with possible dependencies on morphological type, surface brightness, luminosity and color. The result presented in this paper is another strong argument against maximal disks, and it shows that normal, disk-dominated spiral galaxies are submaximal. To infer maximal disks on the basis of our stellar-kinematic measurements, we would on average have to increase the observed velocity dispersions by a factor of ∼2, or alternatively decrease h_z or k with a factor of 3.6 for the entire sample. Based on the available empirical evidence from edge-on galaxies (e.g., Kregel et al. 2002), this does not seem plausible.

In this paper, we compare our fitted NFW-halo parameters from both the submaximal and maximum-Υ_* cases with what has been found from numerical N-body simulations (Bullock et al. 2001). Interestingly, we find that the fitted parameters from the submaximal case show a C-$\mathcal{M}_{200}^{\rm halo}$ relation that is consistent with these simulations, with a concentration parameter typically between $C \sim 10$–20. On the other hand, in the maximum-Υ_* case the fitted concentration parameters are much lower, ($C \sim 1$), and show little correlation with $\mathcal{M}_{200}^{\rm halo}$. The dark-matter-halo parameters derived from the maximum-Υ_* decompositions are not consistent with these simulations.

8.3. The dark-matter distribution

The flatness of the outer part of rotation curves suggests a halo with a dark-matter density distribution declining as $\rho \propto R^{-2}$. The inner slope is still debated. The NFW and similar shapes of the dark-matter halo which have cuspy density profiles with a central slope of $\rho \propto R^{-1}$ to $\rho \propto R^{-1.5}$, have repeatedly been found in dark-matter-only numerical simulations (e.g., Navarro et al. 1996, 1997; Moore et al. 1999; Klypin et al. 2001; Diemand et al. 2005). Observationally, however, a core-like density distribution is often inferred (de Blok et al. 2001; Swaters et al. 2003a,b; Kuzio de Naray et al. 2008, 2009; de Blok 2010; Oh et al. 2011).

Generally, it is thought (e.g., Blumenthal et al. 1986; Gnedin et al. 2004) that the baryons in the inner regions will tend to contract the halo while it is forming. The uncontracted halo in dark-matter-only simulations would then be more extended and have a lower concentration than in observed galaxies. This contraction of the dark-matter halo could be an issue when we fit our models to the data; however, for our light-weight disks we suspect this will only have a mild effect. Several processes may also occur that would instead expand the halo (see Sect. 1). Recent results from, e.g., Barnabè et al. (2012) and Dutton et al. (2013) show that massive spiral galaxies have dark-matter distributions consistent with an unmodified NFW profile. In summary, there is no clear consensus on what can be expected for the inner slope of the dark-matter density distribution due to uncertainties in the baryon physics of galaxy formation. In this paper, we fit pISO and NFW models to our data. Fitting the dark-matter halo with alternative parameterizations to account for the uncertainty in the inner slope, e.g., using Einasto profiles (Einasto 1979; Chemin et al. 2011), will be deferred to a forthcoming paper.

In general, the differences between our fitted pISO and NFW rotation curves are miniscule; both fits have similar χ^2. In Sect. 7, we stacked data from all galaxies to investigate whether the pISO or NFW model fit the data better on average. Although we find slightly less scatter for the pISO-model fit, these results have little statistical significance, mainly due to limitations in our data close to the center and outside the optical disk where the pISO and NFW models tend to differ most. To better distinguish between pISO and NFW-halo distributions we recommend the following improvement at large and small radii for future observations.

Because inner regions often display large gradients in velocity, corrections for beam smearing are large and dependent on assumptions about the unresolved flux and velocity distribution. Corrections can be minimized with observations taken at sufficient physical resolution to resolve the inner rotation-curve rise. The influence of baryonic matter is also highest in the inner regions, primarily due to the presence of bulge or inner-disk components which may have systematically different Υ_* than the outer disk. Direct, dynamical assessment of these innermost mass components would reduce systematic errors in this part of the baryonic rotation curve. Alternatively, observing pure-disk (bulgeless) galaxies might remove this extra complexity, but would naturally lead to an increased bias towards very late-type galaxies. However, chaotic motions in the innermost regions of such systems (Swaters et al. 2003b) may nullify potential advantages of this strategy.

In the outer regions, robust rotation curves require a detailed assessment of both inclination and position-angle warps. Inclination warps are difficult to constrain for nearly face-on galaxies, even with the availability of deep 21-cm aperture-synthesis observations (Martinsson 2011). Galaxies at higher inclination (∼45° to 60°) are required to properly measure inclination warps free of assumptions about the asymptotic shape of the rotation curve. Such high inclination would complicate the measurement of σ_z, but this is mitigated by the relations found in this paper, namely the calibration of Υ_*, and better knowledge of the SVE (presented in future papers of this series).

8.4. Uncertainties and assumptions

The steps in this paper, which have taken us from our observational data (stellar and gas line-of-sight kinematics, NIR, 24-μm and 21-cm imaging) to rotation-curve mass decompositions, include many systematic uncertainties as discussed in great detail in Paper II. Here we revisit the most significant ones.

Throughout our analysis, we have adopted a constant shape of the stellar velocity ellipsoid (SVE) for all galaxies. Fortunately, as part of our survey strategy (Paper I), the resulting uncertainties in the conversion from $\sigma_{\rm LOS}$ to σ_z are limited by the nearly face-on orientation of our galaxy sample. As discussed by Herrmann & Ciardullo (2009), from both observations and theoretical works on the physics of disk scattering, we do not

expect α, which is the dominant contributor to the uncertainties in our deprojection of $\sigma_{\rm LOS}$ to σ_z, to be larger than one. If we assume $\alpha = 1$ then the calculated $\mathcal{F}_{\rm b}$ will certainly be larger; however, we would still find that a majority of the galaxies in our sample are submaximal, with an average $\langle \mathcal{F}_{\rm b}^{2.2h_R} \rangle = 0.65$ when excluding UGC 8196, and with only 6 out of 29 galaxies larger than 0.75. In Paper IV, the shape of the SVE was derived directly from the data for one of our galaxies (UGC 463). We found that it has $\alpha = 0.48 \pm 0.09$ and $\beta = 1.04 \pm 0.22$. Even though these values differ from what we have adopted for this paper, α is still well within the errors, and the measured β differs only 1.5σ from our assumed value. The shape of the SVE for the remaining galaxies in the sample will be revisited in a later paper of the DMS series, where a recalculation of σ_z will be performed and the effect on earlier results will be examined.

Another contribution to the systematic errors comes from uncertainties in the vertical density distribution. It is possible that the distribution parameter (k) differs among and within galaxies. If k is systematically higher than the adopted value, e.g., with a vertical isothermal sech^2 distribution instead of the adopted exponential distribution, our nominal calculations produce an overestimate of $\Sigma_{\rm dyn}$. This would imply that we overestimate $\mathcal{F}_{\rm b}$. If k is systematically lower than the adopted value, we would instead underestimate $\mathcal{F}_{\rm b}$. Among the vertical mass distributions suggested by van der Kruit (1988), we have chosen a value of $k = 1.5$, maximizing $\Sigma_{\rm dyn}$ and $\mathcal{F}_{\rm b}$. In some cases, the effective value of k could be lower; e.g., when the galaxy has a massive thin gas disk. However, the effect from a dark-matter halo (see below) would instead increase k, canceling the effect of the massive gas disk (Paper IV).

Since we observe nearly face-on galaxies, it is impossible to measure the vertical scale height h_z. Instead, we calculate h_z from h_R, using the relation found from edge-on galaxies as described in Paper II. This introduces a significant systematic error (25%) within a galaxy; however, these errors are expected to be random when considering the sample as a whole.

Direct kinematic measurements of the disk inclination has been proven to be difficult for our nearly-face-on galaxies (Martinsson 2011; Paper VI; Andersen & Bershady 2013), and we have adopted inclinations using the inverse Tully-Fisher relation (Paper VI). The uncertainties from these estimated inclinations, mainly introduced as systematic errors in the observed circular speed measurements, are again expected to be random for the sample.

The only known systematic uncertainty for the survey as a whole is the estimated 7% uncertainty on the Hubble constant (H_0; Paper II). An error on H_0 results in an error on the derived distances, which would propagate to both the derived scale (h_R, h_z) and luminosity (M_K) of a galaxy. This would affect our measurement of $\mathcal{F}_{\rm b}$ in the sense that an error on h_z propagates to $V_{\rm b}$ (via $\Sigma_{\rm dyn}$), and an error on M_K propagates to $V_{\rm c}$ (via $i_{\rm TF}$). Although $V_{\rm b}$ and $V_{\rm c}$ change in opposite direction (e.g., if H_0 is smaller, then $V_{\rm b}$ gets smaller and $V_{\rm c}$ gets larger), thereby maximizing the error on $\mathcal{F}_{\rm b}$, the systematic uncertainty on $\mathcal{F}_{\rm b}$ due to the uncertainty on H_0 is only 5%.

Additional uncertainties are introduced by our limited accounting of all the baryonic components. We have only considered the four (presumably) dominant baryonic contributors to the total potential of the galaxy; the stellar bulge, stellar disk, atomic-gas disk, and molecular-gas disk. Our somewhat simplistic one-dimensional bulge-disk decompositions (Paper VI) could introduce some errors, both due to an erroneous assumption of the mass distribution, and a possibly different Υ_* for the bulge compared to the disk. We have limited the uncertainties from the bulge by excluding kinematic measurements inside $R_{\rm bulge}$ (Sect. 2.2), e.g., when calculating $\overline{\Upsilon_*}$. The understanding of the bulge is critical to the inner shape of the dark-matter rotation curves. However, at larger radii (e.g., at $2.2h_R$), the uncertainties from our bulge decompositions are negligible for most of the galaxies in our sample.

We have assumed that the stellar halo contains so little mass as to be dynamically negligible. This is also a valid argument for neglecting the contribution of the mass surface density of the dust in the disk, $\Sigma_{\rm dust}$, which has been observed to have typical ratios $\Sigma_{\rm dust}/\Sigma_{\rm HI} = 0.01$–$0.1$ (Magrini et al. 2011). However, dust may affect our measurements of Υ_* due to extinction, but since we observe close-to face-on galaxies in the NIR, this effect should be small. We further assume that there is no hidden H_2 gas, but that it is traced by the 24-μm emission. Finally, we do not include a thick disk component because, as mentioned in Paper II, the resulting differences in k and h_z tend to cancel when calculating $\Sigma_{\rm dyn}$.

When calculating $\Sigma_{\rm dyn}$ using Eq. (1), we include an infinite, plan-parallel, self-gravitating, isolated disk. For a disk embedded in a dark-matter halo, we expect σ_z will increase for a given $\Sigma_{\rm dyn}$ (Bottema 1993). This, again, results in estimates of Υ_* that are upper limits. The shape of the halo is unknown, but is here assumed to be spherical. There have been studies showing that the dark-matter halo might be highly oblate or prolate (e.g., Amorisco & Bertin 2010; Vera-Ciro et al. 2011). This would further increase σ_z.

9. Summary and conclusions

We have presented rotation-curve mass decompositions of 30 spiral galaxies. From our stellar-kinematic observations we measure vertical velocity dispersions of the stars in the galaxy disks (σ_z). These are used to calculate the disk's dynamical mass surface density ($\Sigma_{\rm dyn}$) from the relation $\Sigma_{\rm dyn} = \sigma_z^2/(\pi G k h_z)$, where we assume a constant disk scale height (h_z) calculated from the disk scale length (h_R), and an exponential vertical distribution of the disk mass and luminosity ($k = 1.5$). Together with measured atomic-gas mass surface densities from 21-cm radio synthesis observations, and molecular-gas mass surface densities estimated from 24-μm *Spitzer* observations, we derive the stellar mass surface density. Using near-infrared 2MASS photometry, we calculate the mass-to-light ratio of the stellar disk (Υ_*), and with the assumption of a constant Υ_* with radius, we derive the stellar-bulge and stellar-disk mass surface densities from the observed surface brightness profiles. The rotation curves of the baryonic components are calculated from their radial mass surface density profiles. These are used together with HI and Hα circular-speed measurements to derive the structural parameters of the dark-matter halo, modeled as either a pISO or NFW halo. We consider two different models for the mass content of the baryonic components; Case I, with mass surface densities dynamically derived directly from our kinematic and photometric observations, and Case II, with scaled-up stellar bulge and disk masses which disregards our dynamical mass-density estimates and instead is designed to contribute maximally to the total mass (a maximum-Υ_* case).

Our derived gas-mass fractions have been compared to results in the recent literature. These agree fairly well, except that we find systematically higher gas-mass fractions. This is most likely due to different methods used to derive the stellar masses.

For individual galaxies, Υ_* has systematic errors that are on average ~70%, mainly due to the uncertainty in h_z when

converting σ_z to $\Sigma_{\rm dyn}$, and the uncertainty in the subtraction of the molecular gas from $\Sigma_{\rm dyn}$. All galaxies have radially-averaged K-band $\overline{\Upsilon_*}$ consistent with being equal. The error-weighted sample average and scatter is $\langle\overline{\Upsilon_*}\rangle = 0.31 \pm 0.07$. On average, we find a Υ_* that is a factor of 3.6 lower than required by the maximum-disk hypothesis. This factor ranges between 1.6 to 8.1, with 20 of the galaxies having values in the range 2.1–4.6. In general, for the galaxies in our sample, the dark-matter halo dominates the potential at almost all radii.

We find the ratio of the baryonic to total rotation velocity, $\mathcal{F}_{\rm b} = V_{\rm b}/V_{\rm c}$, to be nearly constant between 1–6h_R within a galaxy, ranging from ∼0.4–0.7 among individual galaxies. This rather constant $\mathcal{F}_{\rm b}$ arises due to the atomic gas taking over at larger radii where the stellar-disk contribution is declining. The result has a consequence for measuring the maximality; for a comparison of the maximality between different galaxies, it is not critical to measure it at exactly $R_{\rm max}^{\rm disk} \approx 2.2h_R$, and averaging over a band in radius, e.g., around $R = (2.2 \pm 0.5)h_R$, could be a way to obtain measurements with smaller errors.

All galaxies in the sample for which we have reliable measurements are submaximal. On average, $\mathcal{F}_{\rm b}^{2.2h_R} = 0.57 \pm 0.07$, with a weak trend of larger $\mathcal{F}_{\rm b}^{2.2h_R}$ for more luminous galaxies, in agreement with our result in Paper V, but also with a trend of larger $\mathcal{F}_{\rm b}^{2.2h_R}$ for galaxies with higher central surface brightness.

The dark-matter rotation curves tend to be marginally better fit with a pISO than a NFW halo; however, due to limitations in our data both in the central and outer regions of the galaxies, this result has little statistical significance. The shapes of our inferred dark-matter rotation curves in the nominal-Υ_* case are well fit with parameters in agreement with what has been found from dark-matter-only simulations. This result suggests that the baryonic matter in our sample of galaxies has had only a minor effect on the dark-matter distribution. However, when fitting a NFW halo in the maximum-Υ_* case, we find a concentration parameter that is too low compared to the simulations.

A number of improvements may be made to the analysis presented in this paper. With SparsePak, we have observed the stellar kinematics of 12 additional galaxies that, when combined with the PPak data, will increase our sample by more than a third and broaden our parameter space further. Inclusion of our deep optical ($UBVRI$) and near-infrared (JHK) data from the KPNO 2.1-m telescope will dramatically improve our surface photometry. Work is ongoing to determine the SVE shape in individual galaxies, with one of the goals being to reduce the systematic errors introduced from deprojecting $\sigma_{\rm LOS}$ to σ_z. Future analysis will benefit from an improved understanding of the relation between h_R and h_z, taking advantage of ongoing surveys of edge-on galaxies. In future papers, we will extend the analysis of the measured dark-matter distribution, e.g., to establish any correlation with the HI distribution.

In this paper, we have assumed Newtonian gravity. However, it would be interesting to investigate if the theory of modified Newtonian dynamics (MOND; Milgrom 1983) can produce convincing results using submaximal disks. Until then, we conclude that with our assumed Newtonian gravity, the results presented in this paper indicate that the dark matter in spiral galaxies is not only needed to explain the non-declining HI rotation curves in the outer regions, but is also required to explain the rotation curves overall.

Acknowledgements. First, we wish to thank the referee for useful comments and suggestions. T.P.K.M. and M.A.W.V. acknowledge financial support provided by NOVA, the Netherlands Research School for Astronomy, and travel support from the Leids Kerkhoven-Bosscha Fonds. Support for this work has also been provided by the National Science Foundation (NSF) via grants AST-0307417 and AST-0607516 (M.A.B. and K.B.W.), OISE-0754437 (K.B.W.), and AST-1009491 (M.A.B.). K.B.W. is also supported by grant 614.000.807 from the Netherlands Organisation for Scientific Research (NWO). R.A.S. and M.A.B. acknowledge support from NASA/Spitzer grant GO-30894. This publication makes use of data products from the Two Micron All Sky Survey, which is a joint project of the University of Massachusetts and the Infrared Processing and Analysis Center/California Institute of Technology, funded by the National Aeronautics and Space Administration and the National Science Foundation. This work is based in part on observations made with the *Spitzer* Space Telescope, which is operated by the Jet Propulsion Laboratory, California Institute of Technology under a contract with NASA.

References

Amorisco, N. C., & Bertin, G. 2010, A&A, 519, 47
Andersen, D., & Bershady, M. 2013, ApJ, in press
Andersen, D. R., Bershady, M. A., Sparke, L. S., et al. 2006, ApJS, 166, 505
Andersen, D. R., Walcher, C. J., Böker, T., et al. 2008, ApJ, 688, 990
Bahcall, J. N., & Casertano, S. 1984, ApJ, 284, L35
Bahcall, J. N., & Casertano, S. 1985, ApJ, 293, L7
Barnabè, M., Dutton, A. A., Marshall, P. J., et al. 2012, MNRAS, 423, 1073
Begeman, K. G. 1987, Ph.D. Thesis, Kapteyn Institute
Begeman, K. G. 1989, A&A, 223, 47
Begeman, K. G., Broeils, A. H., & Sanders, R. H. 1991, MNRAS, 249, 523
Bendo, G. J., Wilson, C. D., Warren, B. E., et al. 2010, MNRAS, 402, 1409
Bershady, M. A., Andersen, D. R., Harker, J., Ramsey, L. W., & Verheijen, M. A. W. 2004, PASP, 116, 565
Bershady, M. A., Andersen, D. R., Verheijen, M. A. W., et al. 2005, ApJS, 156, 311
Bershady, M. A., Verheijen, M. A. W., Swaters, R. A., et al. 2010a, ApJ, 716, 198
Bershady, M. A., Verheijen, M. A. W., Westfall, K. B., et al. 2010b, ApJ, 716, 234
Bershady, M. A., Martinsson, T. P. K., Verheijen, M. A. W., et al. 2011, ApJ, 739, L47
Blumenthal, G. R., Faber, S. M., Flores, R., & Primack, J. R. 1986, ApJ, 301, 27
Bolatto, A. D., Leroy, A. K., Rosolowsky, E., Walter, F., & Blitz, L. 2008, ApJ, 686, 948
Bosma, A. 1978, Ph.D. Thesis, Groningen Univ.
Bosma, A. 1981a, AJ, 86, 1791
Bosma, A. 1981b, AJ, 86, 1825
Bottema, R. 1993, A&A, 275, 16
Broeils, A. H., & Courteau, S. 1997, in Dark and Visible Matter in Galaxies and Cosmological Implications, eds. M. Persic, & P. Salucci, ASP Conf. Ser., 117, 74
Bullock, J. S., Kolatt, T. S., Sigad, Y., et al. 2001, MNRAS, 321, 559
Byrd, G. G., Freeman, T., & Buta, R. J. 2006, AJ, 131, 1377
Carignan, C., & Freeman, K. C. 1985, ApJ, 294, 494
Catinella, B., Schiminovich, D., Kauffmann, G., et al. 2010, MNRAS, 403, 683
Chemin, L., de Blok, W. J. G., & Mamon, G. A. 2011, AJ, 142, 109
Conroy, C., Gunn, J. E., & White, M. 2009, ApJ, 699, 486
Contini, T., Considere, S., & Davoust, E. 1998, A&AS, 130, 285
Courteau, S., & Rix, H.-W. 1999, ApJ, 513, 561
Courteau, S., Andersen, D. R., Bershady, M. A., MacArthur, L. A., & Rix, H.-W. 2003, ApJ, 594, 208
Dame, T. M., Hartmann, D., & Thaddeus, P. 2001, ApJ, 547, 792
de Blok, W. J. G. 2010, Adv. Astron., 2010
de Blok, W. J. G., McGaugh, S. S., & Rubin, V. C. 2001, AJ, 122, 2396
de Blok, W. J. G., Walter, F., Brinks, E., et al. 2008, AJ, 136, 2648
de Grijs, R., & Peletier, R. F. 1997, A&A, 320, L21
de Grijs, R., & van der Kruit, P. C. 1996, A&AS, 117, 19
de Jong, R. S. 1996, A&A, 313, 377
de Vaucouleurs, G., de Vaucouleurs, A., Corwin, Jr., H. G., et al. 1991, Third Reference Catalogue of Bright Galaxies, eds. N. G. Roman, G. de Vaucouleurs, A. de Vaucouleurs, H. G. Jr. Corwin, R. J. Buta, G. Paturel, & P. Fouqué (New York: Springer-Verlag)
Diemand, J., Zemp, M., Moore, B., Stadel, J., & Carollo, C. M. 2005, MNRAS, 364, 665
Doyle, M. T., Drinkwater, M. J., Rohde, D. J., et al. 2005, MNRAS, 361, 34
Dutton, A. A., Brewer, B. J., Marshall, P. J., et al. 2011, MNRAS, 417, 1621
Dutton, A. A., Treu, T., Brewer, B. J., et al. 2013, MNRAS, 428, 3183
Einasto, J. 1979, in The Large-Scale Characteristics of the Galaxy, ed. W. B. Burton, IAU Symp., 84, 451
El-Zant, A., Shlosman, I., & Hoffman, Y. 2001, ApJ, 560, 636
Fraternali, F., Sancisi, R., & Kamphuis, P. 2011, A&A, 531, 64
Gnedin, O. Y., Kravtsov, A. V., Klypin, A. A., & Nagai, D. 2004, ApJ, 616, 16

Governato, F., Zolotov, A., Pontzen, A., et al. 2012, MNRAS, 422, 1231
Herrmann, K. A., & Ciardullo, R. 2009, ApJ, 705, 1686
Kauffmann, G., Heckman, T. M., White, S. D. M., et al. 2003, MNRAS, 341, 33
Kelz, A., Verheijen, M. A. W., Roth, M. M., et al. 2006, PASP, 118, 129
Kent, S. M. 1986, AJ, 91, 1301
Klypin, A., Kravtsov, A. V., Bullock, J. S., & Primack, J. R. 2001, ApJ, 554, 903
Kranz, T., Slyz, A., & Rix, H.-W. 2003, ApJ, 586, 143
Kregel, M., van der Kruit, P. C., & de Grijs, R. 2002, MNRAS, 334, 646
Kregel, M., van der Kruit, P. C., & Freeman, K. C. 2005, MNRAS, 358, 503
Kuzio de Naray, R., McGaugh, S. S., & de Blok, W. J. G. 2008, ApJ, 676, 920
Kuzio de Naray, R., McGaugh, S. S., & Mihos, J. C. 2009, ApJ, 692, 1321
Leroy, A. K., Walter, F., Brinks, E., et al. 2008, AJ, 136, 2782
Leroy, A. K., Walter, F., Bigiel, F., et al. 2009, AJ, 137, 4670
Magrini, L., Bianchi, S., Corbelli, E., et al. 2011, A&A, 535, A13
Maraston, C. 2005, MNRAS, 362, 799
Martinsson, T. P. K. 2011, Ph.D. Thesis, Univ. of Groningen
Martinsson, T. P. K., Verheijen, M. A. W., Westfall, K. B., Bershady, M. A., & Schechtman-Rook, A. 2013, A&A, in press
Milgrom, M. 1983, ApJ, 270, 365
Moore, B., Quinn, T., Governato, F., Stadel, J., & Lake, G. 1999, MNRAS, 310, 1147
Navarro, J. F., Frenk, C. S., & White, S. D. M. 1996, ApJ, 462, 563
Navarro, J. F., Frenk, C. S., & White, S. D. M. 1997, ApJ, 490, 493
Noordermeer, E., van der Hulst, J. M., Sancisi, R., Swaters, R. S., & van Albada, T. S. 2007, MNRAS, 376, 1513
Oh, S.-H., de Blok, W. J. G., Brinks, E., Walter, F., & Kennicutt, Jr., R. C. 2011, AJ, 141, 193
Ostriker, J. P., & Caldwell, J. A. R. 1979, in The Large-Scale Characteristics of the Galaxy, ed. W. B. Burton, IAU Symp., 84, 441
Paladino, R., Murgia, M., Helfer, T. T., et al. 2006, A&A, 456, 847
Pontzen, A., & Governato, F. 2012, MNRAS, 421, 3464
Read, J. I., & Gilmore, G. 2005, MNRAS, 356, 107
Regan, M. W., Thornley, M. D., Vogel, S. N., et al. 2006, ApJ, 652, 1112
Rix, H., & Zaritsky, D. 1995, ApJ, 447, 82
Sackett, P. D. 1997, ApJ, 483, 103
Saintonge, A., Kauffmann, G., Kramer, C., et al. 2011, MNRAS, 415, 32
Sancisi, R. 2004, in Dark Matter in Galaxies, eds. S. Ryder, D. Pisano, M. Walker, & K. Freeman, IAU Symp., 220, 233
Sanders, R. H. 1996, ApJ, 473, 117
Sanders, R. H., & Verheijen, M. A. W. 1998, ApJ, 503, 97
Schmidt, M. 1985, in The Milky Way Galaxy, eds. H. van Woerden, R. J. Allen, & W. B. Burton, IAU Symp., 106, 75
Skrutskie, M. F., Cutri, R. M., Stiening, R., et al. 2006, AJ, 131, 1163
Sofue, Y., & Rubin, V. 2001, ARA&A, 39, 137
Sofue, Y., Tutui, Y., Honma, M., et al. 1999, ApJ, 523, 136
Swaters, R. A., Madore, B. F., van den Bosch, F. C., & Balcells, M. 2003a, ApJ, 583, 732
Swaters, R. A., Verheijen, M. A. W., Bershady, M. A., & Andersen, D. R. 2003b, ApJ, 587, L19
Swaters, R. A., Sancisi, R., van Albada, T. S., & van der Hulst, J. M. 2011, ApJ, 729, 118
Tully, R. B., & Fisher, J. R. 1977, A&A, 54, 661
van Albada, T. S., & Sancisi, R. 1986, Roy. Soc. London Philos. Trans. Ser. A, 320, 447
van Albada, T. S., Bahcall, J. N., Begeman, K., & Sancisi, R. 1985, ApJ, 295, 305
van der Hulst, J. M., Terlouw, J. P., Begeman, K. G., Zwitser, W., & Roelfsema, P. R. 1992, in Astronomical Data Analysis Software and Systems I, eds. D. M. Worrall, C. Biemesderfer, & J. Barnes, ASP Conf. Ser., 25, 131
van der Kruit, P. C. 1988, A&A, 192, 117
van der Kruit, P. C., & Freeman, K. C. 1984, ApJ, 278, 81
van der Kruit, P. C., & Freeman, K. C. 1986, ApJ, 303, 556
van der Kruit, P. C., & Searle, L. 1981, A&A, 95, 105
Vera-Ciro, C. A., Sales, L. V., Helmi, A., et al. 2011, MNRAS, 416, 1377
Verheijen, M. A. W. 2001, ApJ, 563, 694
Verheijen, M. A. W., Bershady, M. A., Andersen, D. R., et al. 2004, Astron. Nachr., 325, 151
Véron-Cetty, M.-P., & Véron, P. 2006, A&A, 455, 773
Vogelaar, M. G. R., & Terlouw, J. P. 2001, in Astronomical Data Analysis Software and Systems X, eds. F. R. Harnden Jr., F. A. Primini, & H. E. Payne, ASP Conf. Ser., 238, 358
Weiner, B. J., Sellwood, J. A., & Williams, T. B. 2001, ApJ, 546, 931
Westfall, K. B. 2009, Ph.D. Thesis, Univ. of Wisconsin–Madison
Westfall, K. B., Bershady, M. A., & Verheijen, M. A. W. 2011a, ApJS, 193, 21
Westfall, K. B., Bershady, M. A., Verheijen, M. A. W., et al. 2011b, ApJ, 742, 18
Young, J. S., & Scoville, N. Z. 1991, ARA&A, 29, 581
Zwaan, M. A., van der Hulst, J. M., de Blok, W. J. G., & McGaugh, S. S. 1995, MNRAS, 273, L35

Pages 21 to 52 are available in the electronic edition of the journal at http://www.aanda.org

Appendix A: The Atlas

A.1. Content of the Atlas

In this appendix we present data and results for individual galaxies. The next subsection (Sect. A.2) provides some notes on the individual galaxies. In Sect. A.3, an Atlas page is provided for each galaxy. Each page is divided into two columns, each with four panels. The left column demonstrates the progression from the observed surface brightness (μ_K) and vertical velocity dispersions of the disk stars (σ_z) to mass surface densities (Σ) and mass-to-light ratios (Υ). The right column provides four rotation-curve mass decompositions.

The top panel in the left column shows the surface brightness profile. Gray dots represent the observed K-band surface brightness derived in Paper VI. The dashed line shows the fitted bulge. This bulge has been subtracted from the total surface brightness to obtain the light profile of the disk (black errorbars). The second panel shows the measured σ_z (errorbars), azimuthally averaged in 5″ wide rings. The dashed line indicates the exponential fit to the individual-fiber data (Paper VI). The third panel shows the derived mass surface density of the disk ($\Sigma_{\rm dyn}$) and its three component; stars (Σ_*), atomic gas ($\Sigma_{\rm atom}$) and molecular gas ($\Sigma_{\rm mol}$). The open circles indicate $\Sigma_{\rm dyn}$, calculated directly from the measured σ_z. The filled dots with errorbars show the calculated Σ_* (where the gas has been subtracted from $\Sigma_{\rm dyn}$). The dotted and dash-dotted lines show measured $\Sigma_{\rm atom}$ and $\Sigma_{\rm mol}$, respectively. The black dashed line shows $\Sigma_*^{\rm disk}$, calculated from the surface brightness (above) and the weighted average stellar mass-to-light ratio (below). The dark gray dashed line, falling of most rapidly with radius, indicates $\Sigma_*^{\rm bulge}$, calculated with the same mass-to-light ratio as the disk. The bottom panel shows the calculated dynamical ($\Upsilon_{\rm dyn}$; open circles) and stellar (Υ_*; filled circles with errorbars) mass-to-light ratios. The solid and dashed lines show the weighted average of Υ_* and $\Upsilon_{\rm dyn}$, respectively. The arrow on the x-axis indicates $2.2h_R$. In all figures, the light gray shaded region indicates the region excluded from any analysis, typically the "bulge" region, delimited by the radius $R_{\rm bulge}$ at which the light from the bulge contributes 10% to the total light. We have excluded any points within this region when calculating the average Υ. In all panels, the darker gray areas around the measured points indicate systematic errors.

The right column shows four different rotation-curve decompositions. Note that the panels in this column have different radial scaling than the panels in the left column. The observed Hα and HI rotation curves are indicated with filled and open dots, respectively. The rotation curves of the stellar bulge (dark gray dashed line), stellar disk (black dashed line), molecular gas (dash-dotted line) and atomic gas (dotted line) have been calculated from the mass surface densities shown in the left column, as described in Sect. 5.1. The solid gray line indicates the fitted dark-matter rotation curve. The solid black line is the quadrature sum of the various components. From top to bottom, the four panels in the right column show the rotation-curve mass decomposition results when using the nominal Υ_* with a fitted pISO dark-matter halo (Case Ia); the nominal Υ_* with a fitted NFW dark-matter halo (Case Ib); a maximum disk (scaled-up Υ_*) with a fitted pISO dark-matter halo (Case IIa); and a maximum disk with a fitted NFW dark-matter halo (Case IIb). The arrow in the bottom panel indicates $2.2h_R$, the theoretical radius of maximum rotation speed of an infinitely-thin exponential disk.

A.2. Notes on individual galaxies

Here, we present a few notes on the individual galaxies. See Paper VI for more detailed notes on the data products of the individual galaxies from PPak, for comments on [OIII] emission, stellar and [OIII] kinematics, kinematic flaring, known supernovae within the galaxies, and for notes on close field stars. See Martinsson (2011) for more comments on the HI observations of the individual galaxies, and for notes on close companion galaxies (detected in HI).

UGC 448: IC 43. High-quality kinematics, with regular stellar and gas kinematics. Significant bulge with second highest bulge-to-disk ratio in the sample ($B/D = 0.32$). The rotation curve rises quite sharply. HI rotation curve corrected for an inclination warp (Martinsson 2011). A small bar and significant spiral structure are visible morphologically, but exhibit little kinematic influence.
UGC 463: NGC 234. High-quality kinematics. PPak and SparsePak data studied in detail in Paper IV. Strong, three-arm spiral structure with minor streaming motions.
UGC 1081: NGC 575, IC 1710. Strongly barred galaxy. Bright field star within the PPak field-of-view. A Type-II break exists in $\mu_K(R)$ at roughly $1h_R$ (approximately the same as the bar length). The mass surface density profile of the atomic gas is estimated using the results in Martinsson (2011).
UGC 1087: "Ringing" present in $\mu_K(R)$ associated with the azimuthal coherence of the tightly wound spiral arms. HI rotation curve corrected for an inclination warp (Martinsson 2011).
UGC 1529: IC 193. High-quality kinematics. Sc galaxy, rather typical of our sample, apart from the high inclination ($i_{\rm TF} = 39°$). The mass surface density profile of the atomic gas is estimated using the results in Martinsson (2011).
UGC 1635: IC 208. A Type-II break in $\mu_K(R)$ occurs at $\sim 1h_R$ with a corresponding dip in the [OIII] and Hα rotation curves; any dynamical association between these features is unknown. Gas poor.
UGC 1862: Unique among our sample: It has the lowest luminosity, $M_K = -21.0$, one magnitude fainter than the second least luminous galaxy (UGC 3701). Two Type-II breaks exist in $\mu_K(R)$ (at ∼23″ and ∼60″), but no indication of a bulge component; inner break is caused by the spiral arms. Appears to have a rather large bar. Data within $R = 2\farcs5$ are excluded in the kinematic analysis, to avoid beam-smearing effects particularly strong in the center. The only galaxy in the sample for which the rotation curve does not reach $R = 2.2h_R$. The mass surface density profile of the atomic gas is estimated using the results in Martinsson (2011).
UGC 1908: NGC 927, Mrk 593. Barred galaxy with a weak Type-II break in $\mu_K(R)$ at $\sim 1h_R$. Classified as a Starburst Nucleus Galaxy (SBNG), but its nucleus has an ambiguous activity classification between H_2 and LINER (Contini et al. 1998). The mass surface density profile of the atomic gas is estimated using the results in Martinsson (2011).
UGC 3091: Since the bulge/disk fitting routine resulted in a non-existing bulge, the excess light in the central region is interpreted as an inner disk. As with UGC 1862, $\sigma_{\rm LOS}$ and σ_z data within $R = 2\farcs5$ are excluded from our analysis. The mass surface density profile of the atomic gas is estimated using the results in Martinsson (2011).
UGC 3140: NGC 1642. Very close to face on with $i_{\rm TF} = 14°$. Nicely defined spiral structure but slightly lopsided. The μ_K profile breaks to a more extended disk (larger scale length) at $R \sim 16''$. There is a small offset between the HI and Hα rotation curves (Sect. 4.1), possibly due to

HI asymmetries. HI rotation curve corrected for an inclination warp (Martinsson 2011).

UGC 3701: Second lowest disk surface brightness in our sample. Some ringing in the μ_K profile due to the spiral arms. Rotation curve rises slowly. HI rotation curve corrected for an inclination warp (Martinsson 2011).

UGC 3997: Classified as Im by RC3 with low surface brightness. There is a small offset between the HI and Hα rotation curves (Sect. 4.1), maybe due to the warp in position angle, corrected for in the HI rotation curve (Martinsson 2011) but not in the Hα rotation curve.

UGC 4036: NGC 2441. Observations are dominated by ring-like structure, probably due to weak bar. Streaming motions likely affect the observed rotation curve.

UGC 4107: High-quality kinematics. Well-defined three-arm spiral structure. Type-II break in $\mu_K(R)$ at $R \sim 20''$.

UGC 4256: NGC 2532. Two close companions ~4′ to the north connected by an HI bridge (Martinsson 2011). Interaction has likely produced the bright arm toward the east and the lopsidedness of the galaxy. High star-formation rate with very bright [OIII] emission associated with visible star-formation regions (Paper VI). One of two galaxies in the sample with a molecular gas mass which is larger than the stellar mass. Note that the bump feature in the modeled molecular-gas rotation curve can also be seen in the observed rotation curve, and that the submaximal cases fit this feature better than the maximum-Υ_* cases. There is a small offset between the HI and Hα rotation curves (Sect. 4.1), maybe due to its kinematic lopsidedness.

UGC 4368: NGC 2575. Highest inclination in the sample ($i_{\rm TF} = 45°$). High-quality stellar kinematics. Type-II breaks in $\mu_K(R)$ at $R \sim 16''$ and $R \sim 30''$.

UGC 4380: Low-inclination galaxy ($i_{\rm TF} = 13.^\circ8$) with a small apparent size and scale length. Stellar-kinematic data have limited radial extent. HI rotation curve corrected for an inclination warp (Martinsson 2011).

UGC 4458: NGC 2599, Mrk 389. Earliest morphological type in our sample (Sa), with the largest bulge-to-disk ratio ($B/D = 0.72$). Some spiral structure visible at large radii, but very smooth morphology otherwise. HI rotation curve declines from 350 km s^{-1} to 250 km s^{-1}. The bulge dominates all stellar-kinematic data; $\overline{\Upsilon_*}$ derived from the last measured point only.

UGC 4555: NGC 2649. Strong spiral structure affects $\mu_K(R)$. High-quality stellar-kinematic data.

UGC 4622: The most distant galaxy in the sample ($V_{\rm sys} = 12830$ km s^{-1}; $D = 178$ Mpc). Stellar kinematics limited to $R < 15''$. Type-II break in $\mu_K(R)$ at $R \sim 15''$. Fourth highest bulge-to-disk ratio ($B/D = 0.16$). HI rotation curve corrected for an inclination warp (Martinsson 2011).

UGC 6903: Barred galaxy with rather low surface brightness. Poorest quality of stellar-kinematic data in our sample (one hour observation with PPak). Strong dip in $\mu_K(R)$ at $R \sim 20''$.

UGC 6918: NGC 3982. High-surface-brightness member of the Ursa Major cluster. Very high-quality kinematic data. Classified as a Seyfert 1.9 (Véron-Cetty & Véron 2006). Warped and lopsided extension to the HI gas (Martinsson 2011); PPak kinematics are regular. Included in DMS pilot sample as presented in early publications (Verheijen et al. 2004; Bershady et al. 2005; Westfall 2009). Type-II break in $\mu_K(R)$ at $R \sim 1h_R$; $\sigma_{\rm LOS}$ transitions to a shallower slope at this radius. The galaxy with the highest molecular gas-to-stellar mass ratio in the sample; together with UGC 4256 the only galaxy with higher molecular-gas mass than stellar mass. Like UGC 4256, this galaxy also shows a bump feature in the calculated molecular gas rotation curve which can be seen in the observed rotation curve. HI rotation curve corrected for an inclination warp (Martinsson 2011).

UGC 7244: NGC 4195. Barred galaxy, modeled assuming no bulge; inner excess in $\mu_K(R)$ ($R \leq 8''$) interpreted as an inner disk. As with UGC 1862, we exclude $R < 2.''5$ from our analysis. Stellar-kinematic measurements only reach $R \sim 20''$. The receding part of the HI rotation curve rises steeper than the approaching side (Martinsson 2011). This is not seen in the Hα rotation curve, and results in some offsets between the HI and Hα rotation curves (Sect. 4.1). In optical images (Paper I), this galaxy looks rather peculiar, with an offset bar and bent spiral arms.

UGC 7917: NGC 4662. High-quality stellar kinematics. Gas-poor in the center, resulting in no measured Hα and HI kinematics in that region. Excluded kinematic data at $R < 1h_R$ (shaded region in the Atlas) to remove bar-associated regions. Type-II break in $\mu_K(R)$ at $R \sim 25''$. Fifth highest bulge-to-disk ratio ($B/D = 0.14$).

UGC 8196: NGC 4977. Early-type spiral (SAb). Third highest bulge-to-disk ratio in the sample ($B/D = 0.24$). Gas-poor (Martinsson 2011, Paper VI). HI rotation curve corrected for an inclination warp (Martinsson 2011). Low-surface-brightness, extended disk with strong spiral structure not probed by our kinematics. Rather complex $\mu_K(R)$, transitions to a shallower slope at $R \sim 10''$, which may be an extent of the bulge not accounted for in our bulge-disk decomposition. Has a non-physical measurement of the maximality and is generally excluded from the results in this paper.

UGC 9177: Well-defined spiral structure affecting $\mu_K(R)$. High inclination ($i_{\rm TF} = 40°$) and high-quality rotation curves. Measurements of $\sigma_{\rm LOS}$ limited to $R < 25''$.

UGC 9837: Stellar data has a limited radial extent. Weak morphological bar does not affect the kinematics. Shallower slope in $\mu_K(R)$ beyond $\sim 1h_R$. Regular HI kinematics.

UGC 9965: IC 1132. Very nearly face-on ($i_{\rm TF} = 12°$) with strong spiral structure visible in $\mu_K(R)$. Bulgeless galaxy; as with UGC 1862, we exclude data within $R = 2.''5$ in the kinematic analysis. HI rotation curve corrected for an inclination warp (Martinsson 2011).

UGC 11318: NGC 6691. Barred galaxy. Lowest inclination in the sample ($i_{\rm TF} = 5.^\circ8$), yielding a very low-amplitude projected rotation curve. Type-II break in $\mu_K(R)$ at $\sim 1h_R$.

UGC 12391: NGC 7495. Type-II break in $\mu_K(R)$ at $R \sim 25''$. The mass surface density profile of the atomic gas is estimated using the results in Martinsson (2011).

A.3. Atlas

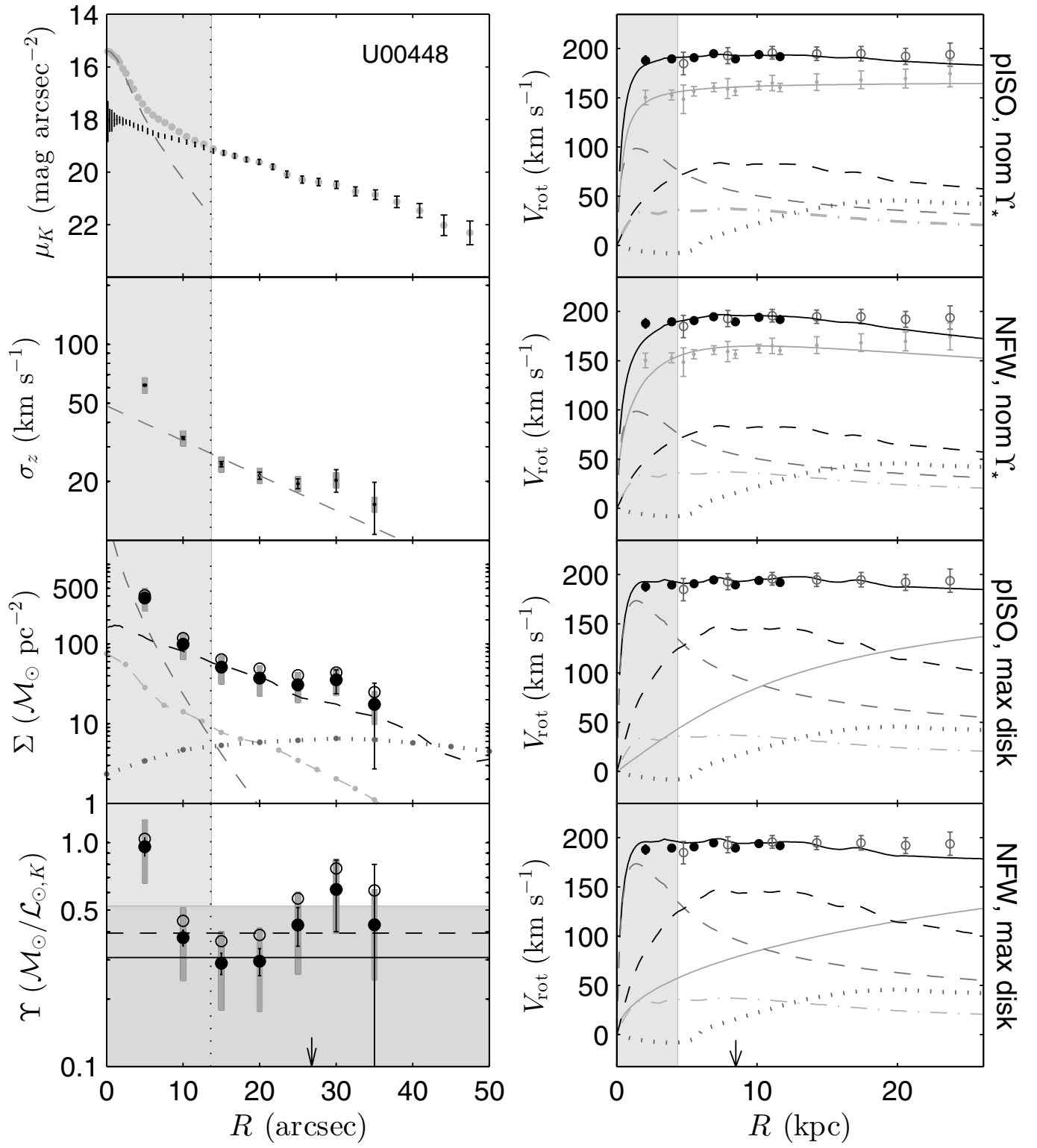
U00448
μ_K (mag arcsec^{-2})
σ_z (km s^{-1})
Σ ($\mathcal{M}_\odot$ pc^{-2})
Υ ($\mathcal{M}_\odot/\mathcal{L}_{\odot,K}$)
R (arcsec)
$V_{\rm rot}$ (km s^{-1})
pISO, nom Υ_*
NFW, nom Υ_*
pISO, max disk
NFW, max disk
R (kpc)

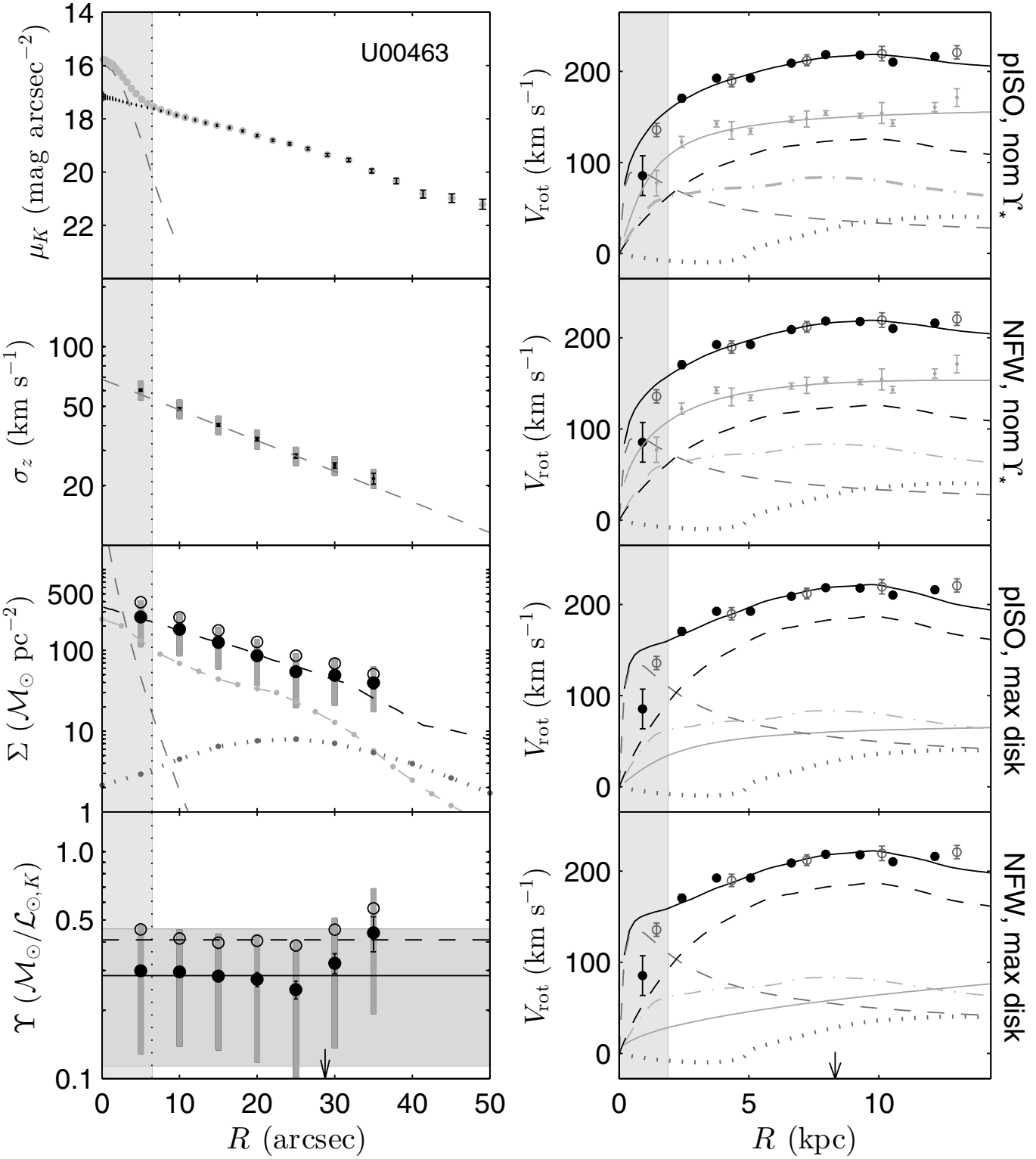
U00463
μ_K (mag arcsec^{-2})
σ_z (km s^{-1})
Σ ($\mathcal{M}_\odot$ pc^{-2})
Υ ($\mathcal{M}_\odot/\mathcal{L}_{\odot,K}$)
R (arcsec)
$V_{\rm rot}$ (km s^{-1})
R (kpc)
pISO, nom Υ_*
NFW, nom Υ_*
pISO, max disk
NFW, max disk

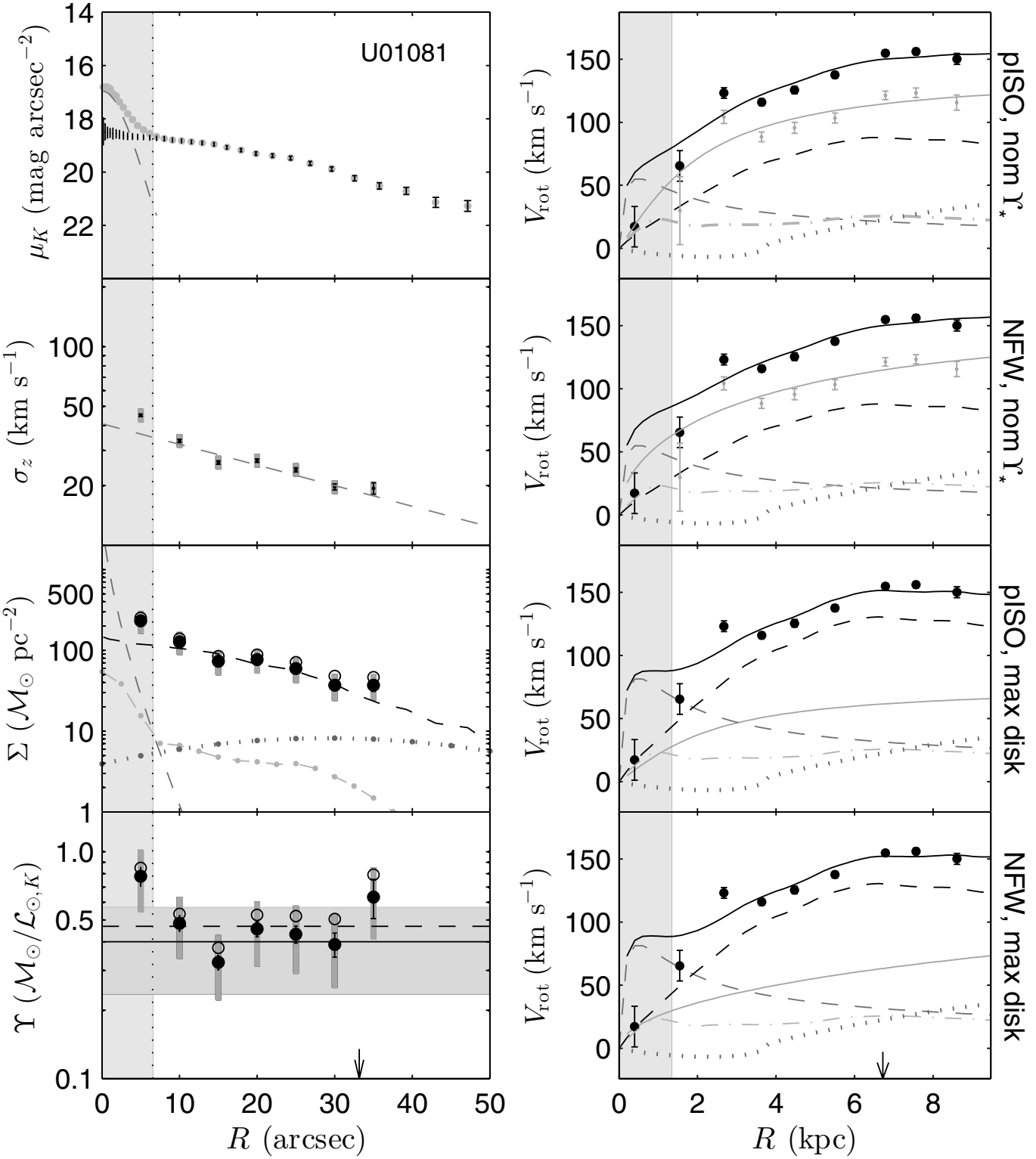
U01081
μ_K (mag arcsec^{-2})
σ_z (km s^{-1})
Σ ($\mathcal{M}_\odot$ pc^{-2})
Υ ($\mathcal{M}_\odot/\mathcal{L}_{\odot,K}$)
R (arcsec)
$V_{\rm rot}$ (km s^{-1})
pISO, nom Υ_*
NFW, nom Υ_*
pISO, max disk
NFW, max disk
R (kpc)

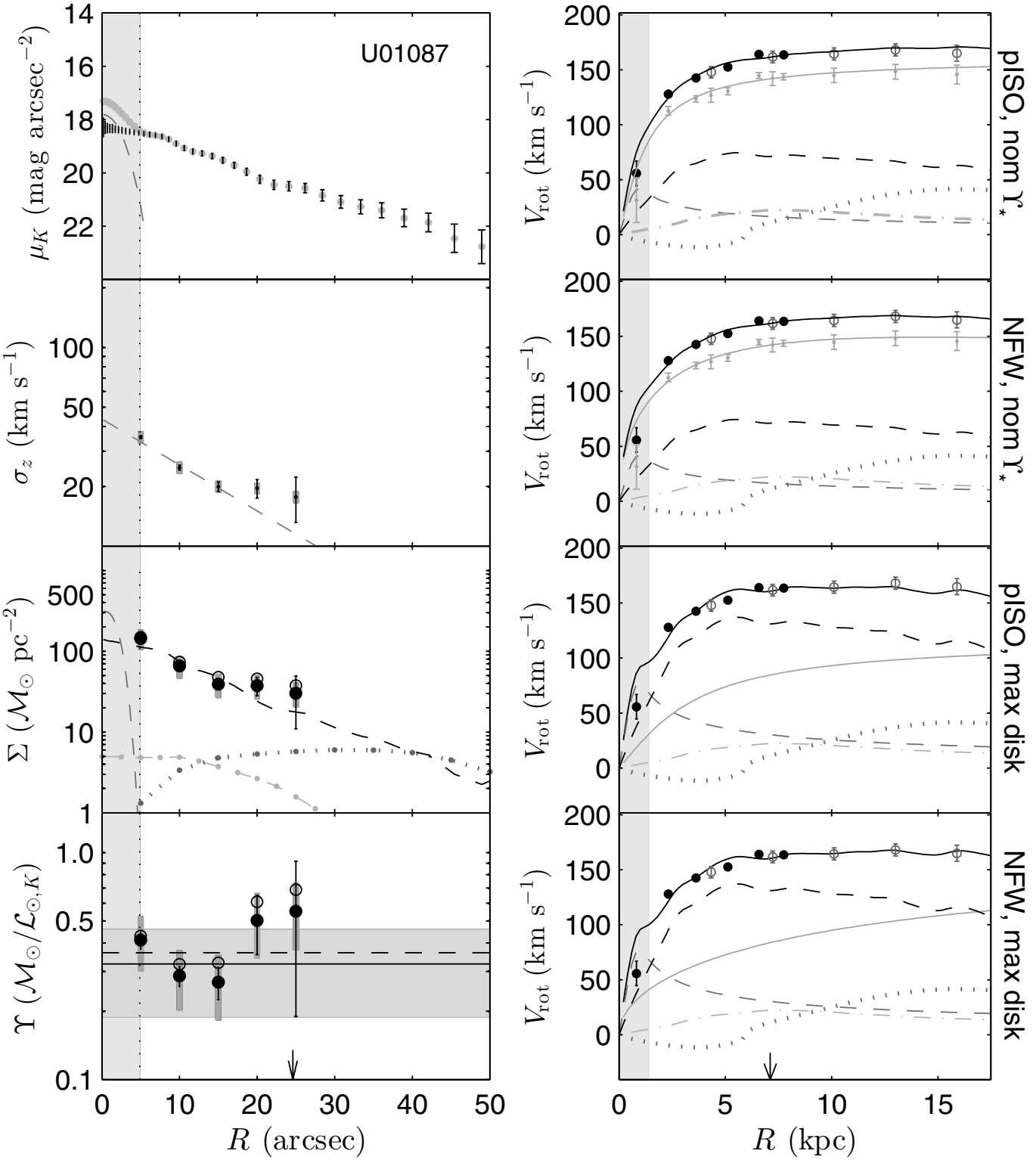
U01087
μ_K (mag arcsec^{-2})
σ_z (km s^{-1})
Σ ($\mathcal{M}_\odot$ pc^{-2})
Υ ($\mathcal{M}_\odot/\mathcal{L}_{\odot,K}$)
R (arcsec)
$V_{\rm rot}$ (km s^{-1})
pISO, nom Υ_*
NFW, nom Υ_*
pISO, max disk
NFW, max disk
R (kpc)

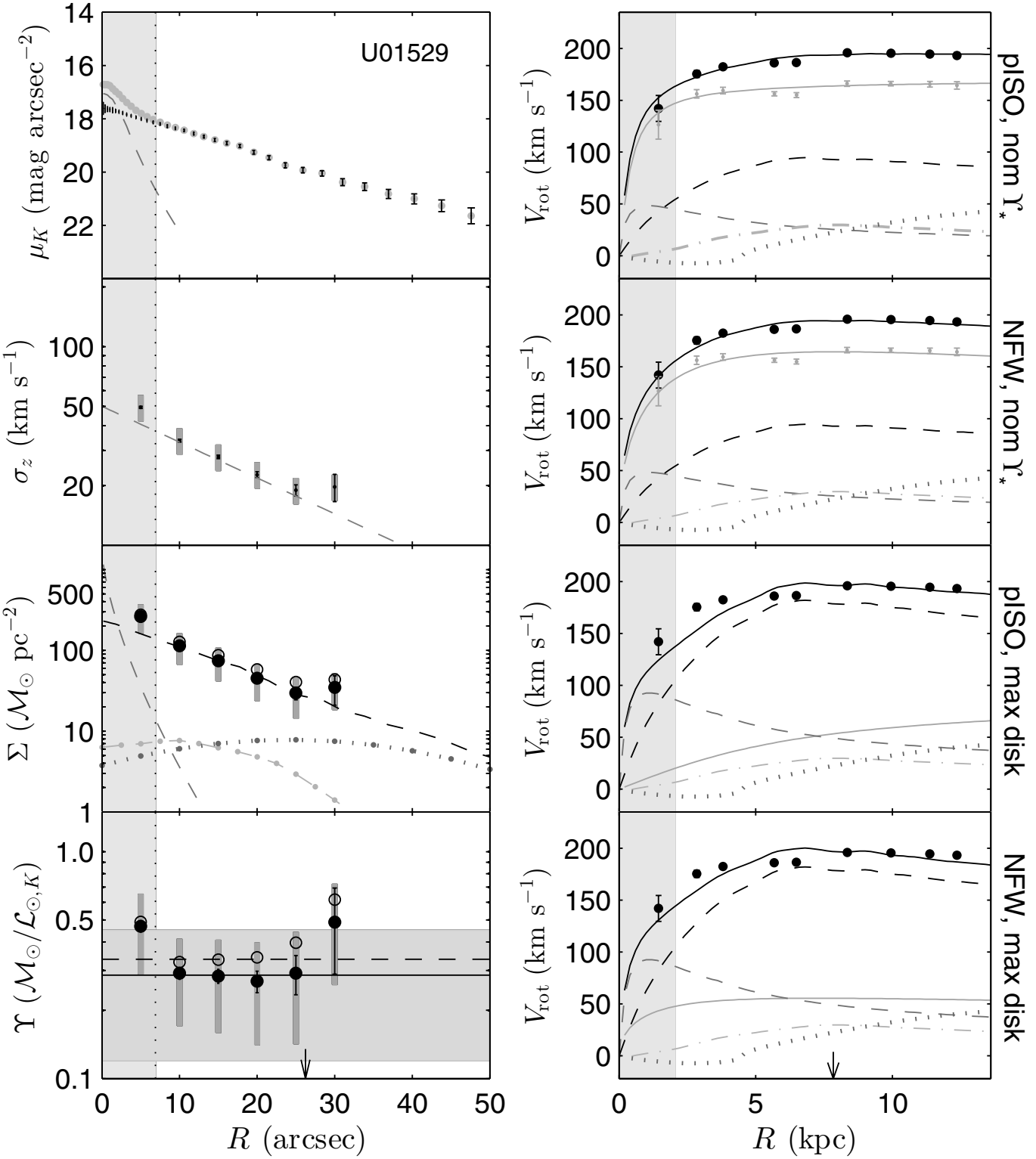
U01529
μ_K (mag arcsec^{-2})
σ_z (km s^{-1})
Σ ($\mathcal{M}_\odot$ pc^{-2})
Υ ($\mathcal{M}_\odot/\mathcal{L}_{\odot,K}$)
R (arcsec)
$V_{\rm rot}$ (km s^{-1})
plSO, nom Υ_*
NFW, nom Υ_*
plSO, max disk
NFW, max disk
R (kpc)

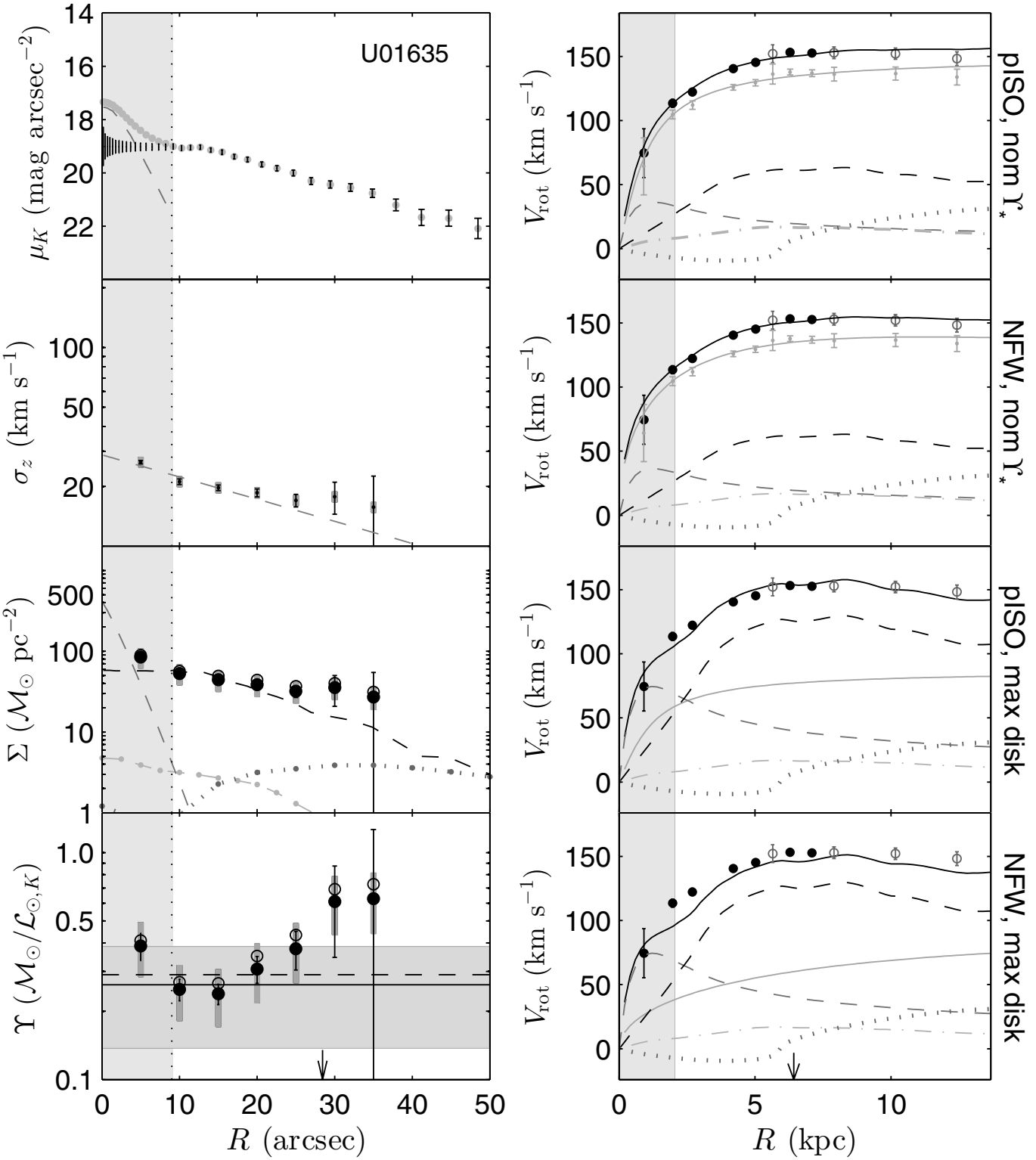
U01635
μ_K (mag arcsec^{-2})
σ_z (km s^{-1})
Σ ($\mathcal{M}_\odot$ pc^{-2})
Υ ($\mathcal{M}_\odot/\mathcal{L}_{\odot,K}$)
R (arcsec)
$V_{\rm rot}$ (km s^{-1})
R (kpc)
pISO, nom Υ_*
NFW, nom Υ_*
pISO, max disk
NFW, max disk

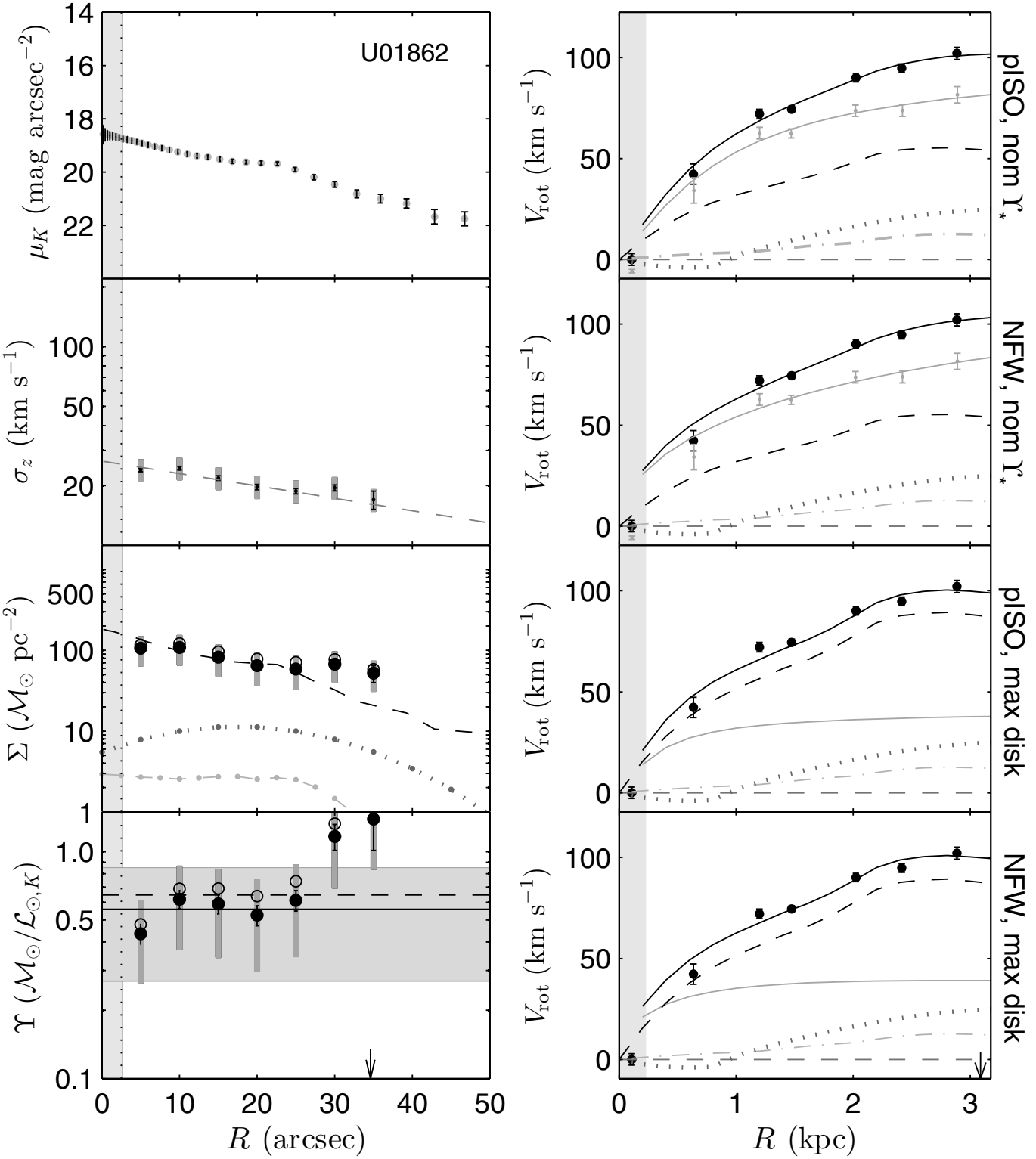
U01862
μ_K (mag arcsec^{-2})
σ_z (km s^{-1})
Σ ($\mathcal{M}_\odot$ pc^{-2})
Υ ($\mathcal{M}_\odot/\mathcal{L}_{\odot,K}$)
R (arcsec)
$V_{\rm rot}$ (km s^{-1})
plSO, nom Υ_*
NFW, nom Υ_*
plSO, max disk
NFW, max disk
R (kpc)

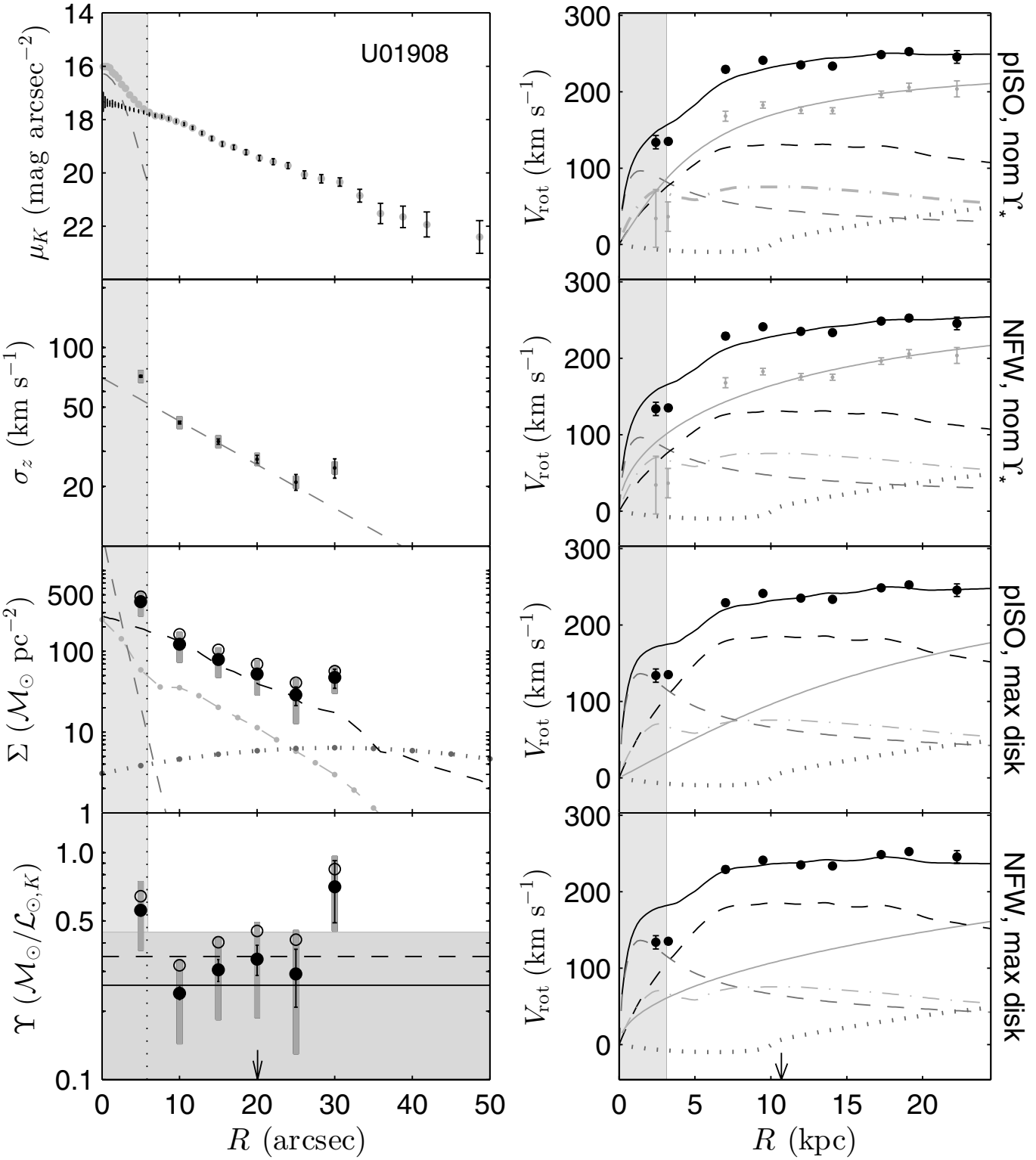
U01908
μ_K (mag arcsec^{-2})
σ_z (km s^{-1})
Σ ($\mathcal{M}_\odot$ pc^{-2})
Υ ($\mathcal{M}_\odot/\mathcal{L}_{\odot,K}$)
R (arcsec)
$V_{\rm rot}$ (km s^{-1})
pISO, nom Υ_*
NFW, nom Υ_*
pISO, max disk
NFW, max disk
R (kpc)

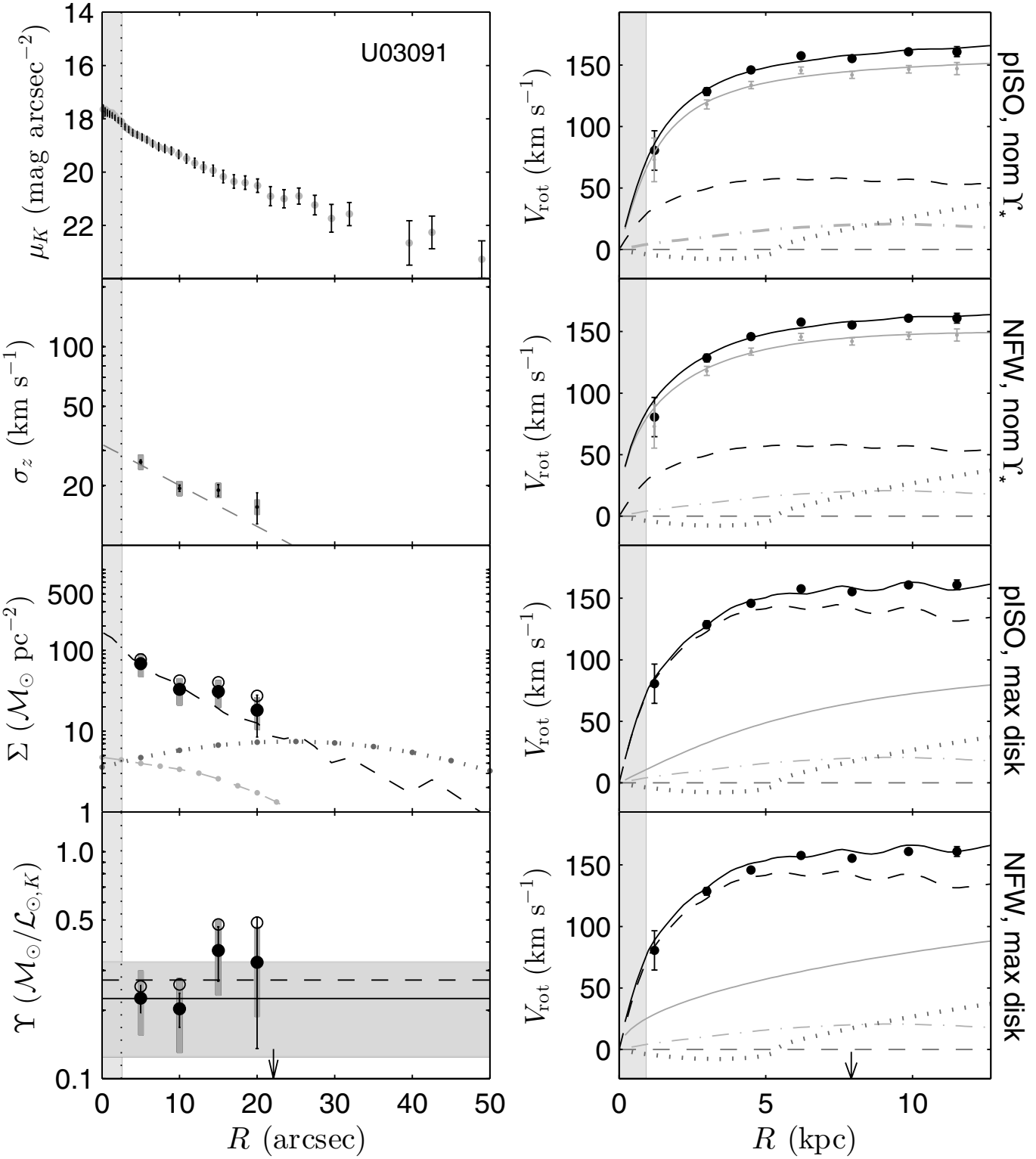
U03091
μ_K (mag arcsec^{-2})
σ_z (km s^{-1})
Σ ($\mathcal{M}_\odot$ pc^{-2})
Υ ($\mathcal{M}_\odot/\mathcal{L}_{\odot,K}$)
R (arcsec)
$V_{\rm rot}$ (km s^{-1})
pISO, nom Υ_*
NFW, nom Υ_*
pISO, max disk
NFW, max disk
R (kpc)

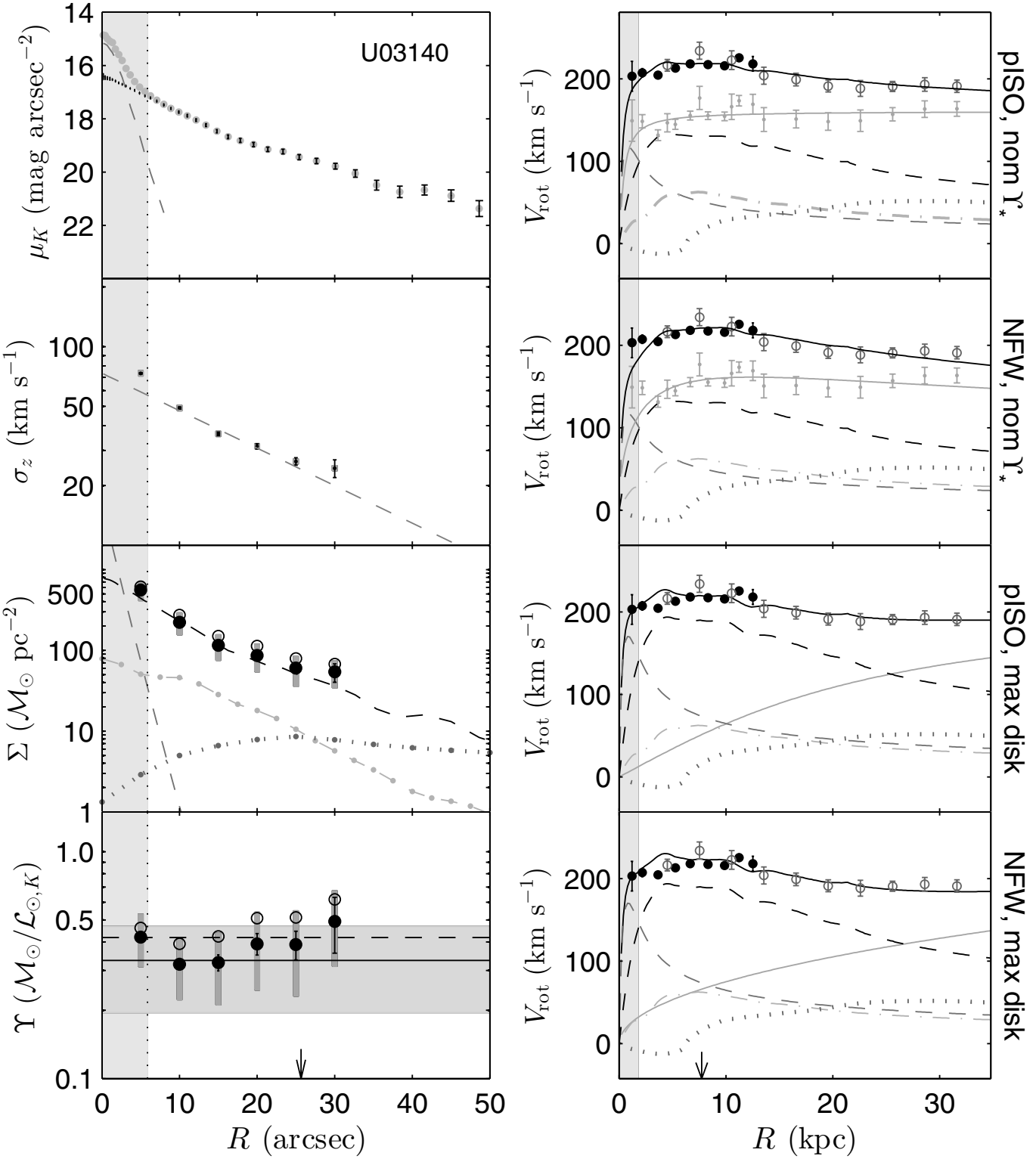
U03140
μ_K (mag arcsec^{-2})
σ_z (km s^{-1})
Σ ($\mathcal{M}_\odot$ pc^{-2})
Υ ($\mathcal{M}_\odot/\mathcal{L}_{\odot,K}$)
R (arcsec)
$V_{\rm rot}$ (km s^{-1})
pISO, nom Υ_*
NFW, nom Υ_*
pISO, max disk
NFW, max disk
R (kpc)

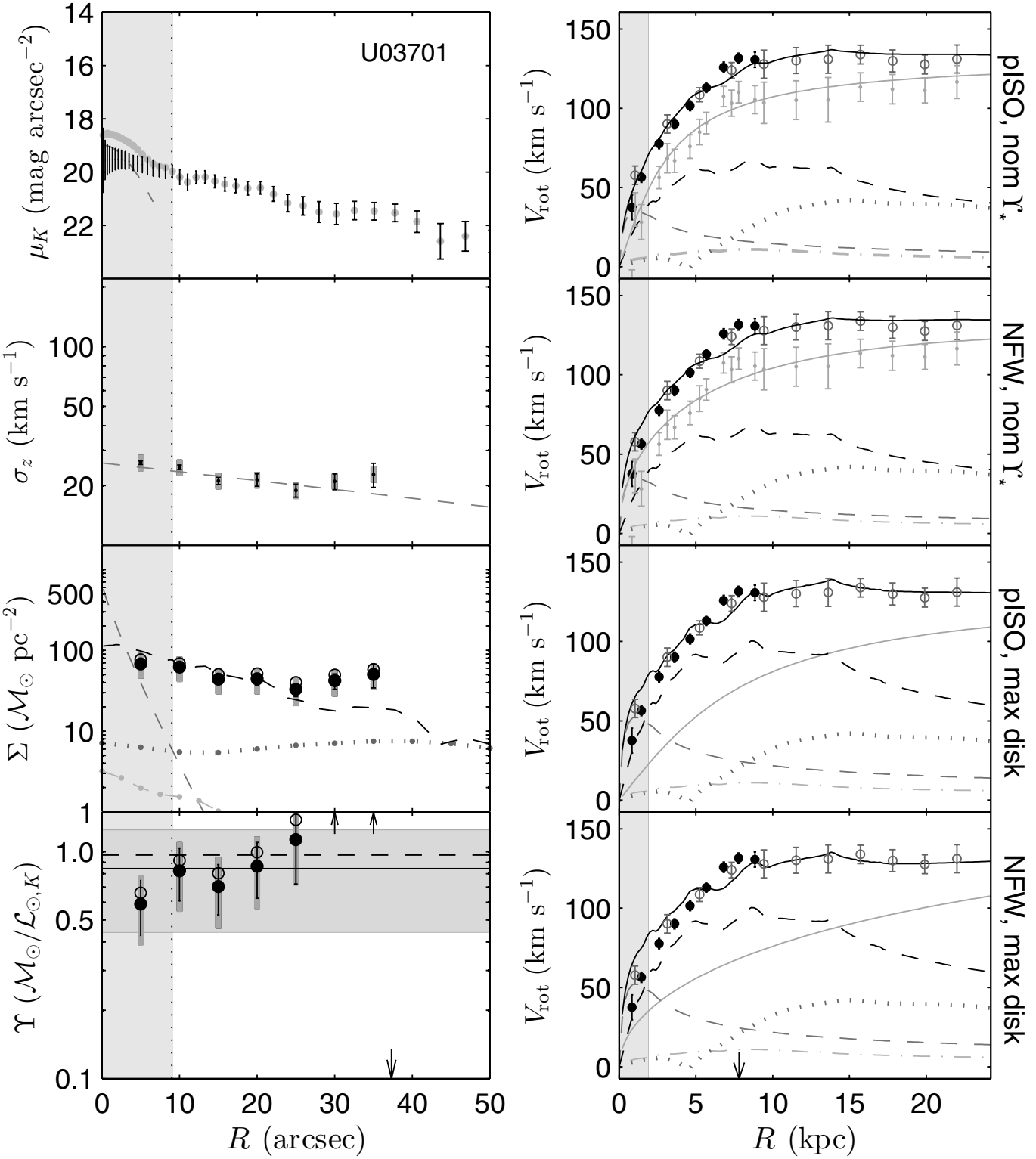
U03701
μ_K (mag arcsec^{-2})
σ_z (km s^{-1})
Σ ($\mathcal{M}_\odot$ pc^{-2})
Υ ($\mathcal{M}_\odot/\mathcal{L}_{\odot,K}$)
R (arcsec)
$V_{\rm rot}$ (km s^{-1})
pISO, nom Υ_*
NFW, nom Υ_*
pISO, max disk
NFW, max disk
R (kpc)

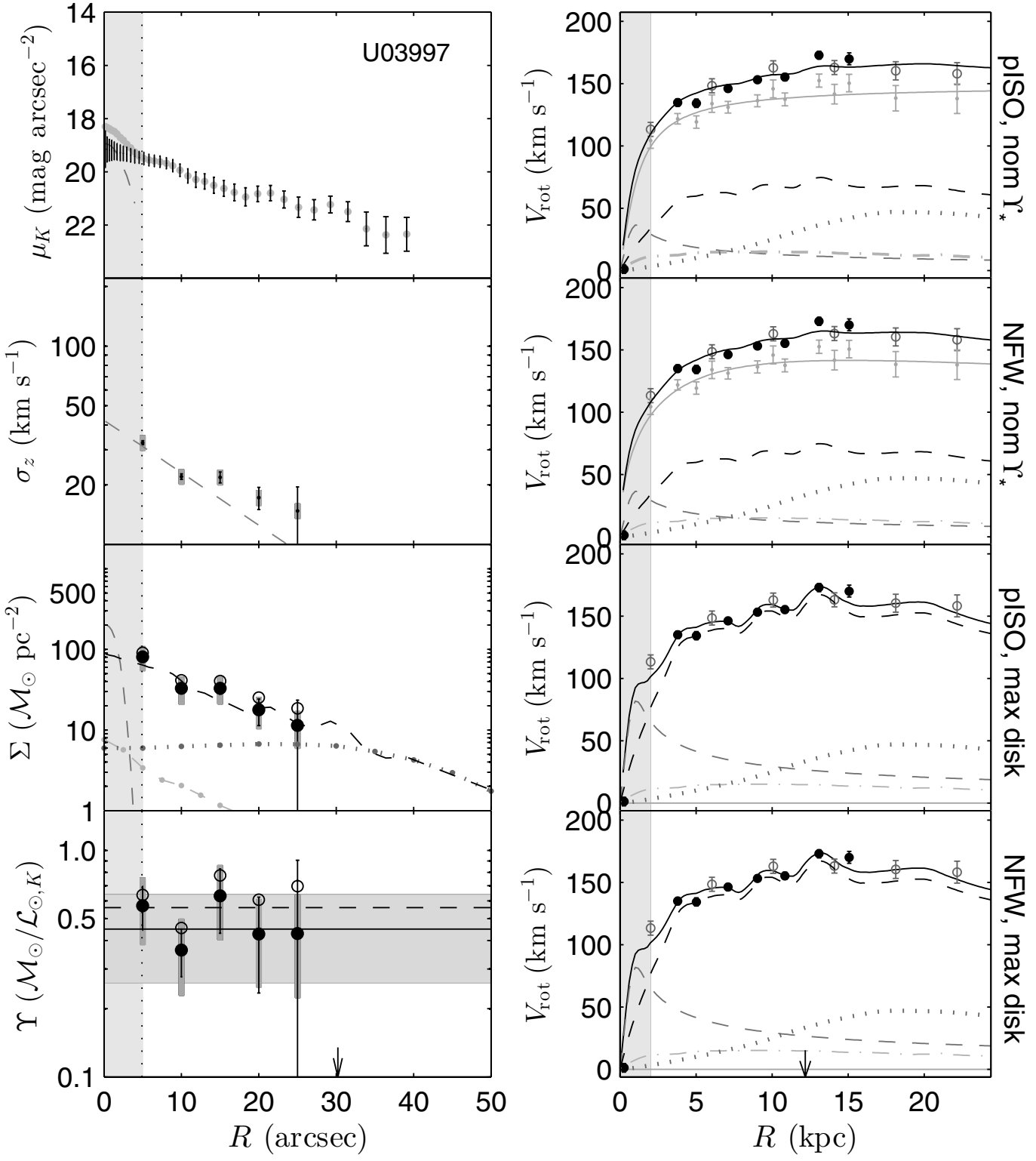
U03997
μ_K (mag arcsec^{-2})
σ_z (km s^{-1})
Σ ($\mathcal{M}_\odot$ pc^{-2})
Υ ($\mathcal{M}_\odot/\mathcal{L}_{\odot,K}$)
R (arcsec)
$V_{\rm rot}$ (km s^{-1})
R (kpc)
pISO, nom Υ_*
NFW, nom Υ_*
pISO, max disk
NFW, max disk

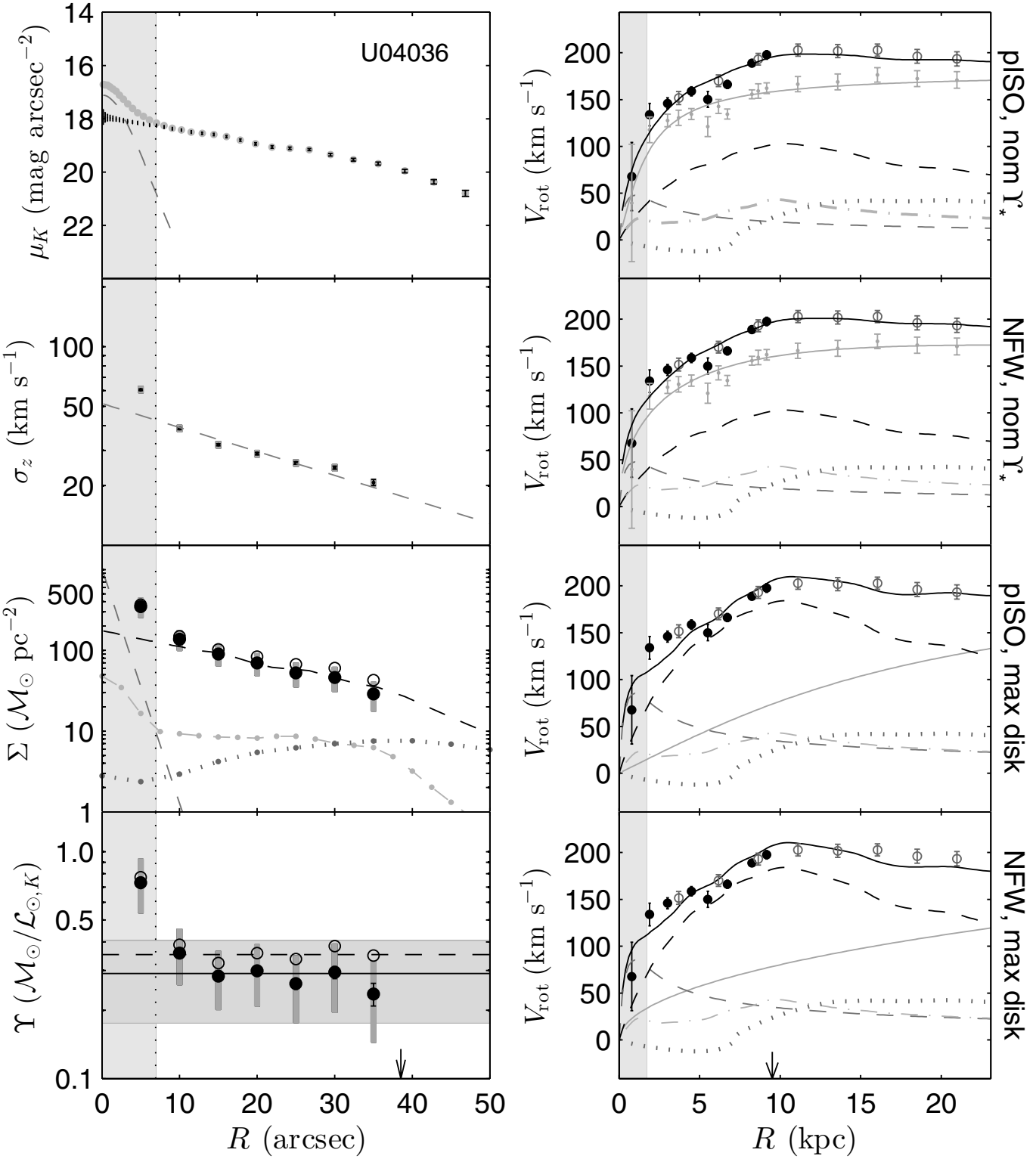
U04036
μ_K (mag arcsec^{-2})
σ_z (km s^{-1})
Σ ($\mathcal{M}_\odot$ pc^{-2})
Υ ($\mathcal{M}_\odot/\mathcal{L}_{\odot,K}$)
R (arcsec)
$V_{\rm rot}$ (km s^{-1})
pISO, nom Υ_*
NFW, nom Υ_*
pISO, max disk
NFW, max disk
R (kpc)

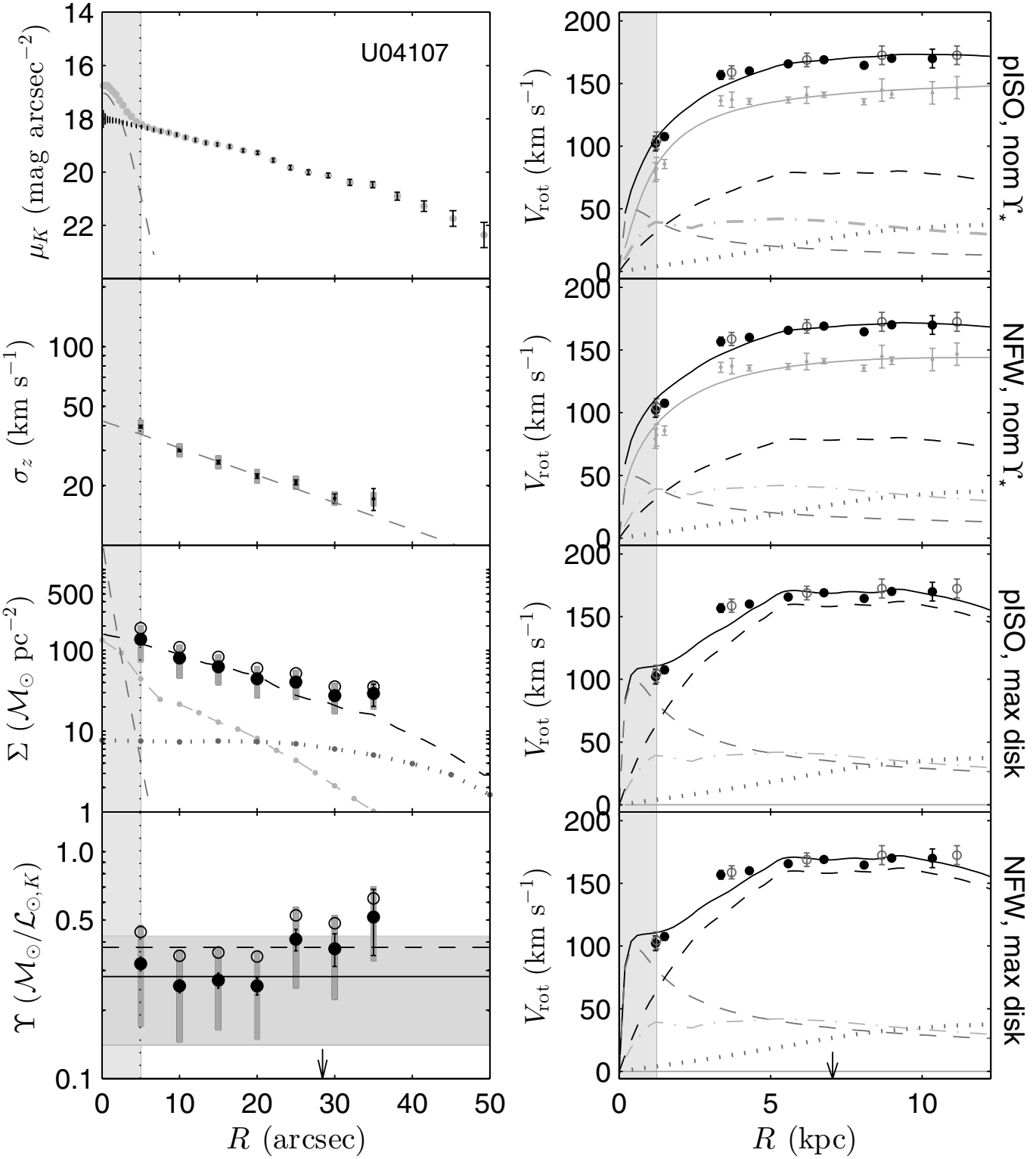
U04107
μ_K (mag arcsec^{-2})
σ_z (km s^{-1})
Σ ($\mathcal{M}_\odot$ pc^{-2})
Υ ($\mathcal{M}_\odot/\mathcal{L}_{\odot,K}$)
R (arcsec)
$V_{\rm rot}$ (km s^{-1})
R (kpc)
pISO, nom Υ_*
NFW, nom Υ_*
pISO, max disk
NFW, max disk

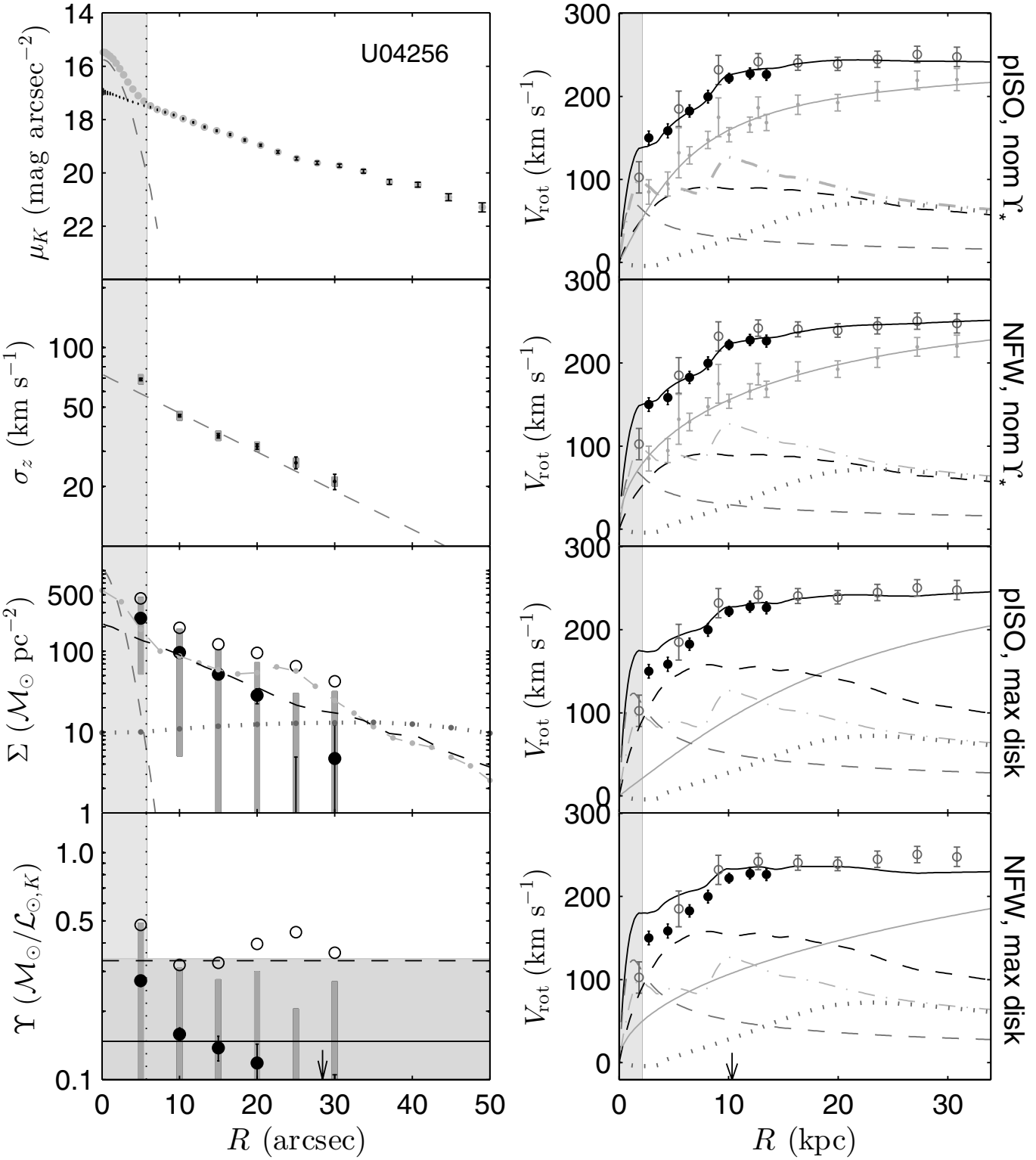
U04256
μ_K (mag arcsec^{-2})
σ_z (km s^{-1})
Σ ($\mathcal{M}_\odot$ pc^{-2})
Υ ($\mathcal{M}_\odot/\mathcal{L}_{\odot,K}$)
R (arcsec)
$V_{\rm rot}$ (km s^{-1})
pISO, nom Υ_*
NFW, nom Υ_*
pISO, max disk
NFW, max disk
R (kpc)

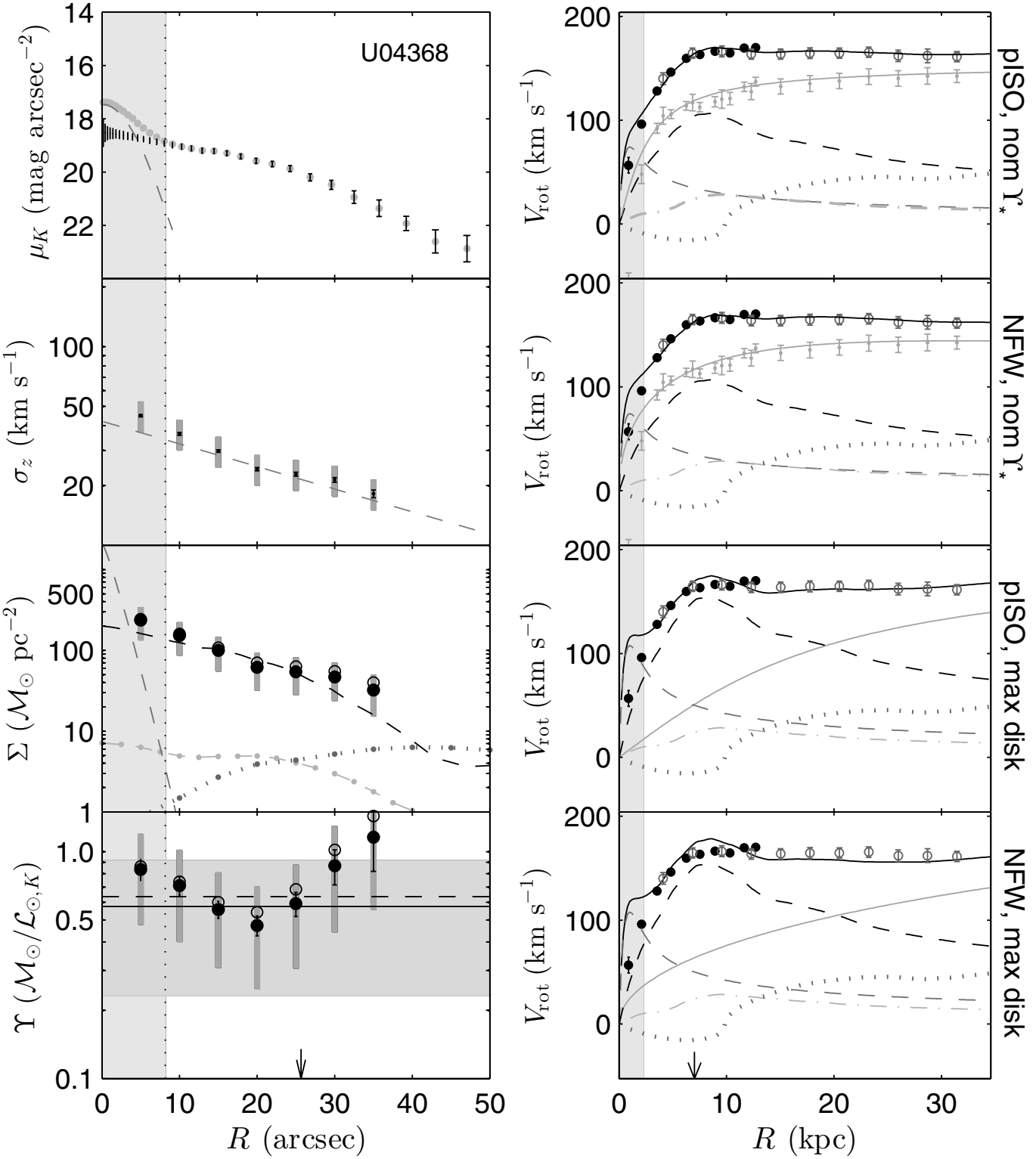
U04368
μ_K (mag arcsec^{-2})
σ_z (km s^{-1})
Σ ($\mathcal{M}_\odot$ pc^{-2})
Υ ($\mathcal{M}_\odot/\mathcal{L}_{\odot,K}$)
R (arcsec)
$V_{\rm rot}$ (km s^{-1})
pISO, nom Υ_*
NFW, nom Υ_*
pISO, max disk
NFW, max disk
R (kpc)

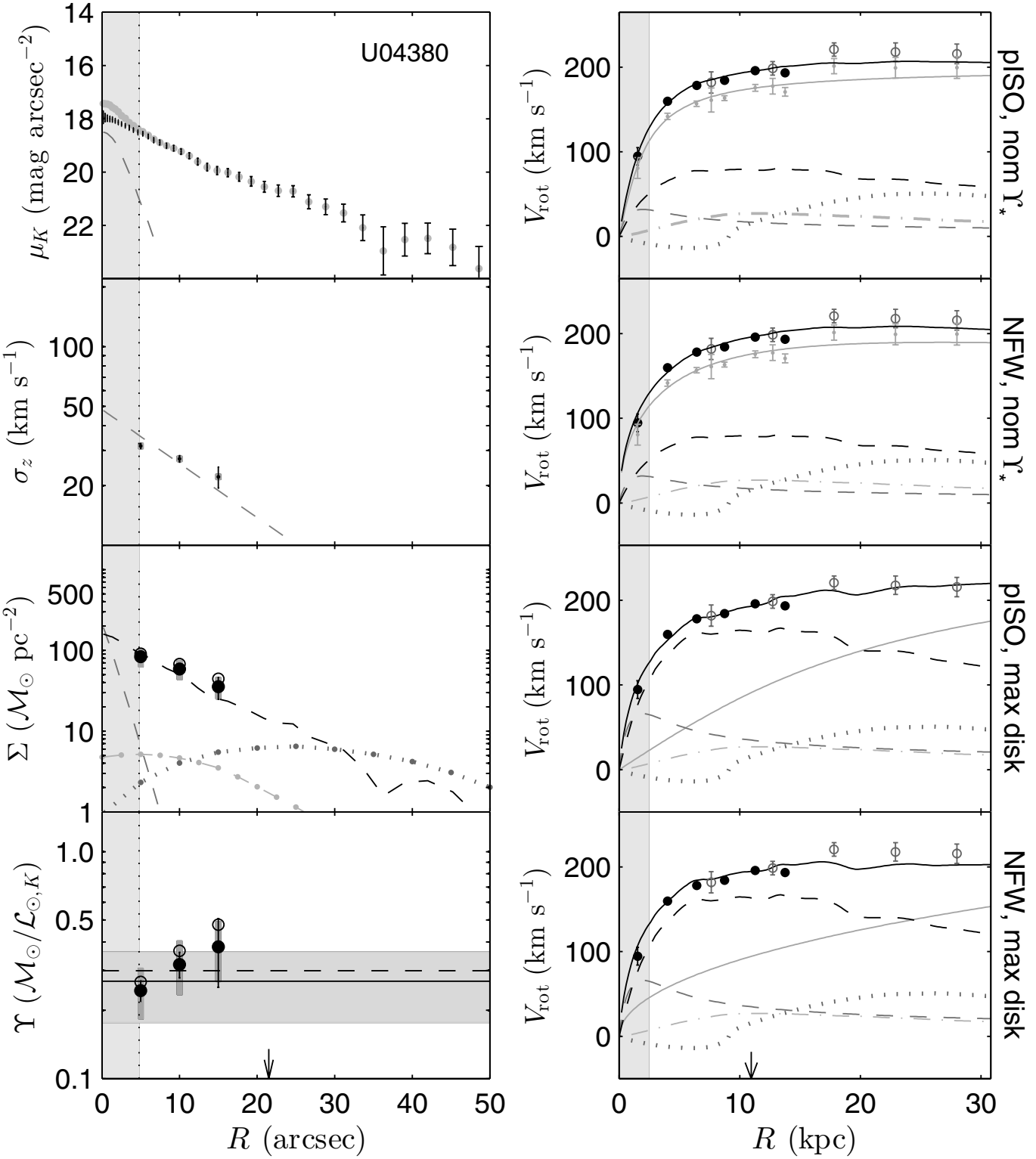
U04380
μ_K (mag arcsec^{-2})
σ_z (km s^{-1})
Σ ($\mathcal{M}_\odot$ pc^{-2})
Υ ($\mathcal{M}_\odot/\mathcal{L}_{\odot,K}$)
R (arcsec)
$V_{\rm rot}$ (km s^{-1})
pISO, nom Υ_*
NFW, nom Υ_*
pISO, max disk
NFW, max disk
R (kpc)

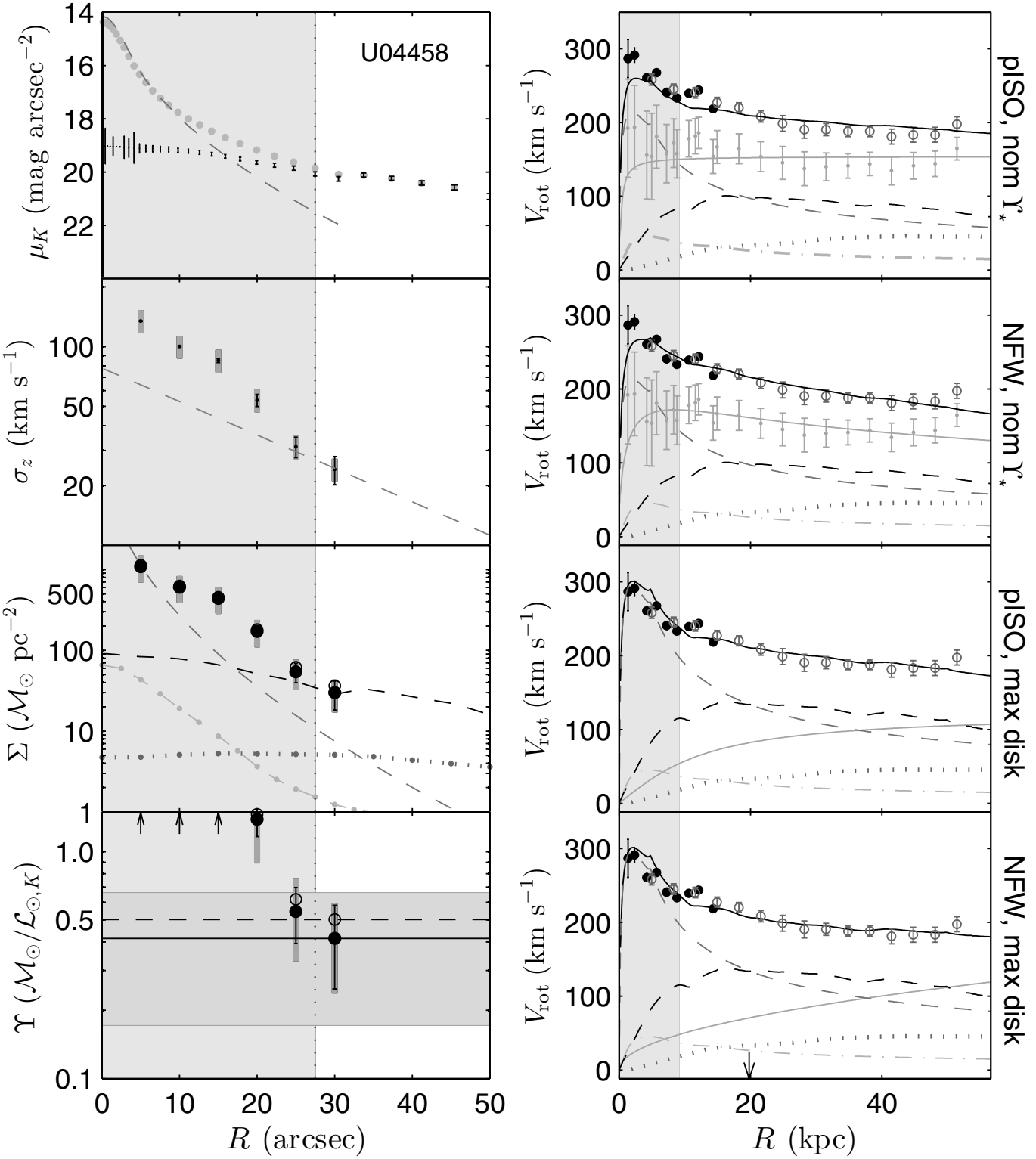
U04458
μ_K (mag arcsec^{-2})
σ_z (km s^{-1})
Σ ($\mathcal{M}_\odot$ pc^{-2})
Υ ($\mathcal{M}_\odot/\mathcal{L}_{\odot,K}$)
R (arcsec)
$V_{\rm rot}$ (km s^{-1})
R (kpc)
pISO, nom Υ_*
NFW, nom Υ_*
pISO, max disk
NFW, max disk

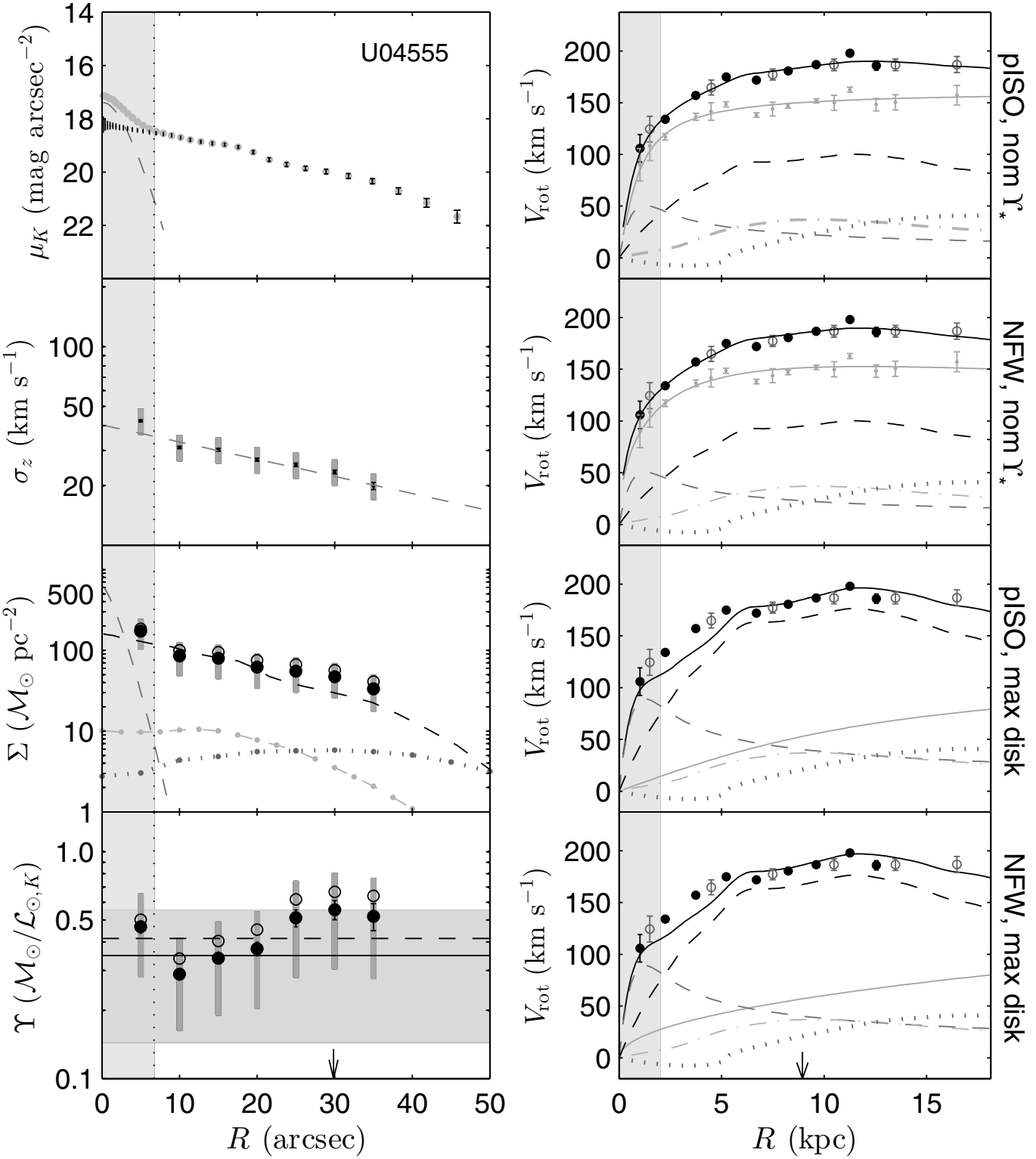
U04555
μ_K (mag arcsec^{-2})
σ_z (km s^{-1})
Σ ($\mathcal{M}_\odot$ pc^{-2})
Υ ($\mathcal{M}_\odot/\mathcal{L}_{\odot,K}$)
R (arcsec)
$V_{\rm rot}$ (km s^{-1})
pISO, nom Υ_*
NFW, nom Υ_*
pISO, max disk
NFW, max disk
R (kpc)

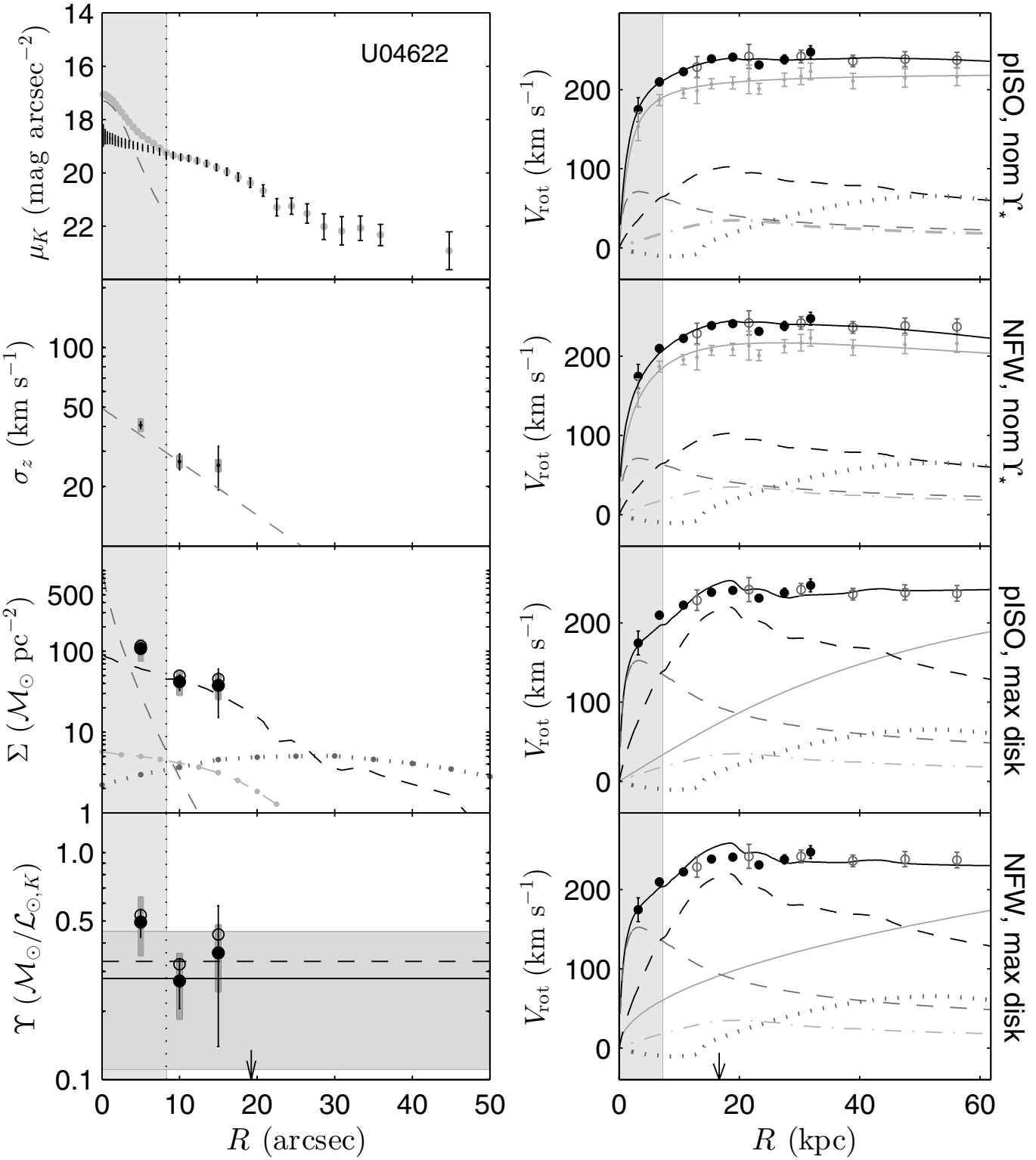
U04622
μ_K (mag arcsec^{-2})
σ_z (km s^{-1})
Σ ($\mathcal{M}_\odot$ pc^{-2})
Υ ($\mathcal{M}_\odot/\mathcal{L}_{\odot,K}$)
R (arcsec)
$V_{\rm rot}$ (km s^{-1})
R (kpc)
pISO, nom Υ_*
NFW, nom Υ_*
pISO, max disk
NFW, max disk

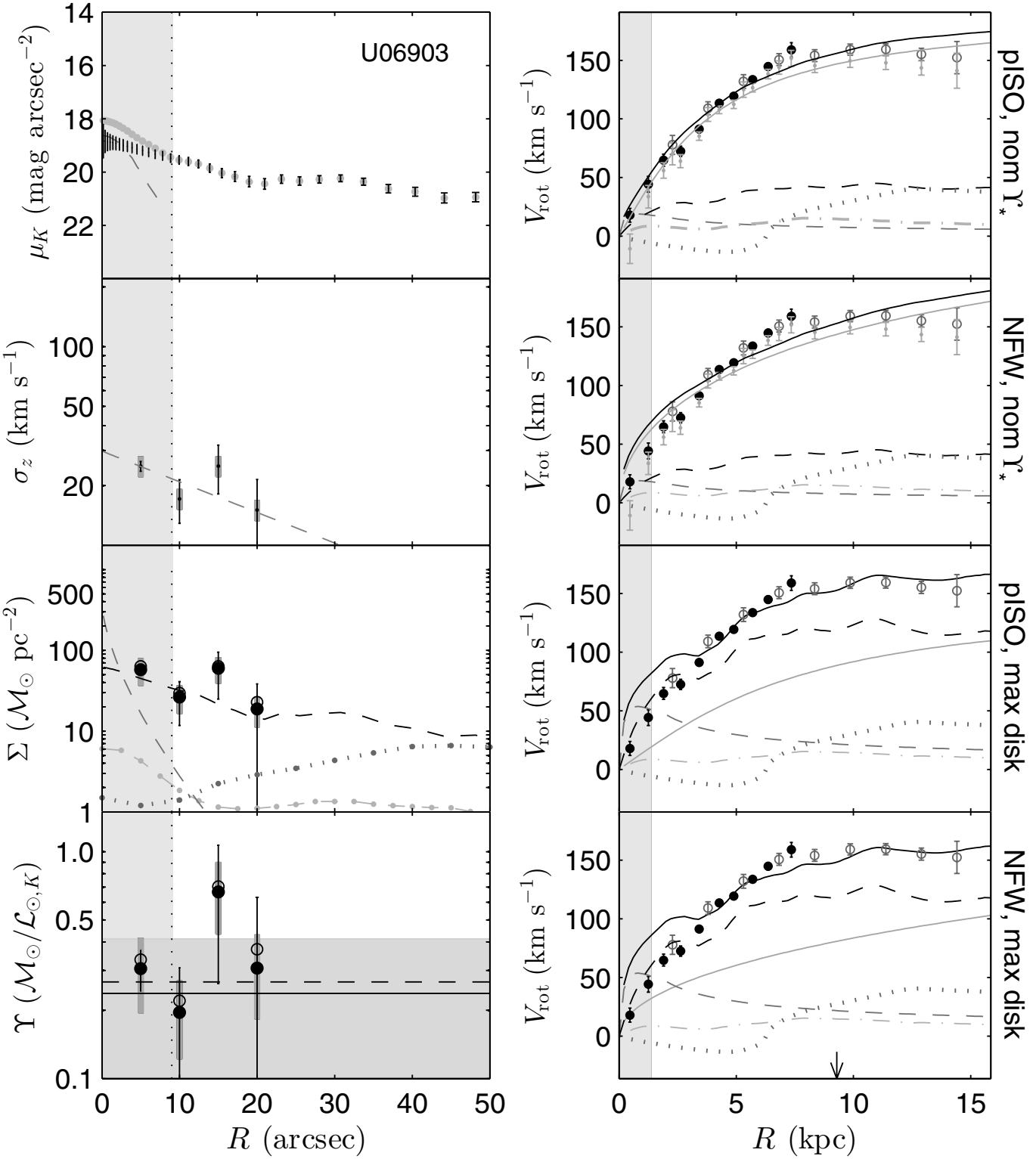
U06903
μ_K (mag arcsec^{-2})
σ_z (km s^{-1})
Σ ($\mathcal{M}_\odot$ pc^{-2})
Υ ($\mathcal{M}_\odot/\mathcal{L}_{\odot,K}$)
R (arcsec)
$V_{\rm rot}$ (km s^{-1})
pISO, nom Υ_*
NFW, nom Υ_*
pISO, max disk
NFW, max disk
R (kpc)

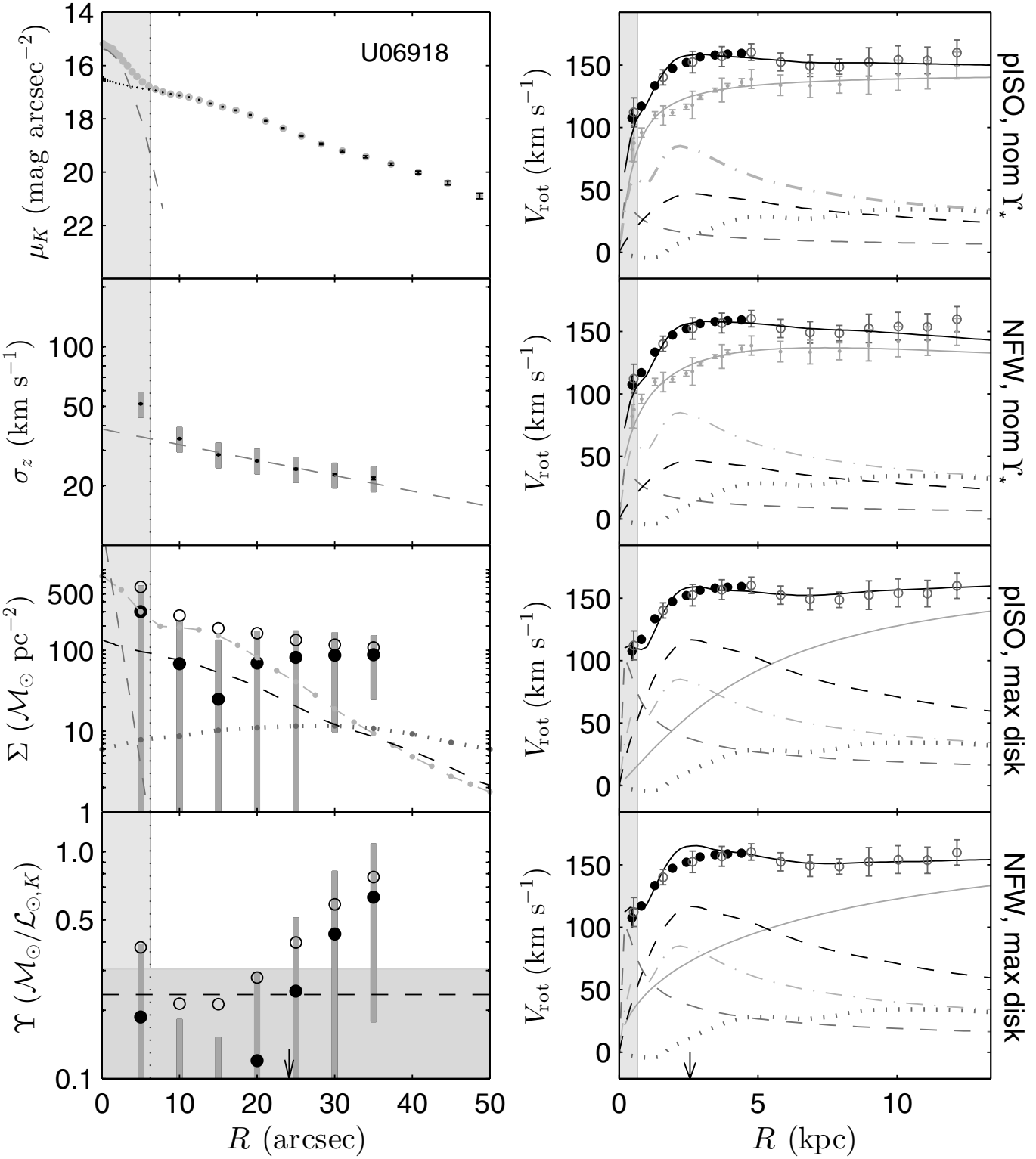
U06918
μ_K (mag arcsec^{-2})
σ_z (km s^{-1})
Σ ($\mathcal{M}_\odot$ pc^{-2})
Υ ($\mathcal{M}_\odot/\mathcal{L}_{\odot,K}$)
R (arcsec)
$V_{\rm rot}$ (km s^{-1})
R (kpc)
pISO, nom Υ_*
NFW, nom Υ_*
pISO, max disk
NFW, max disk

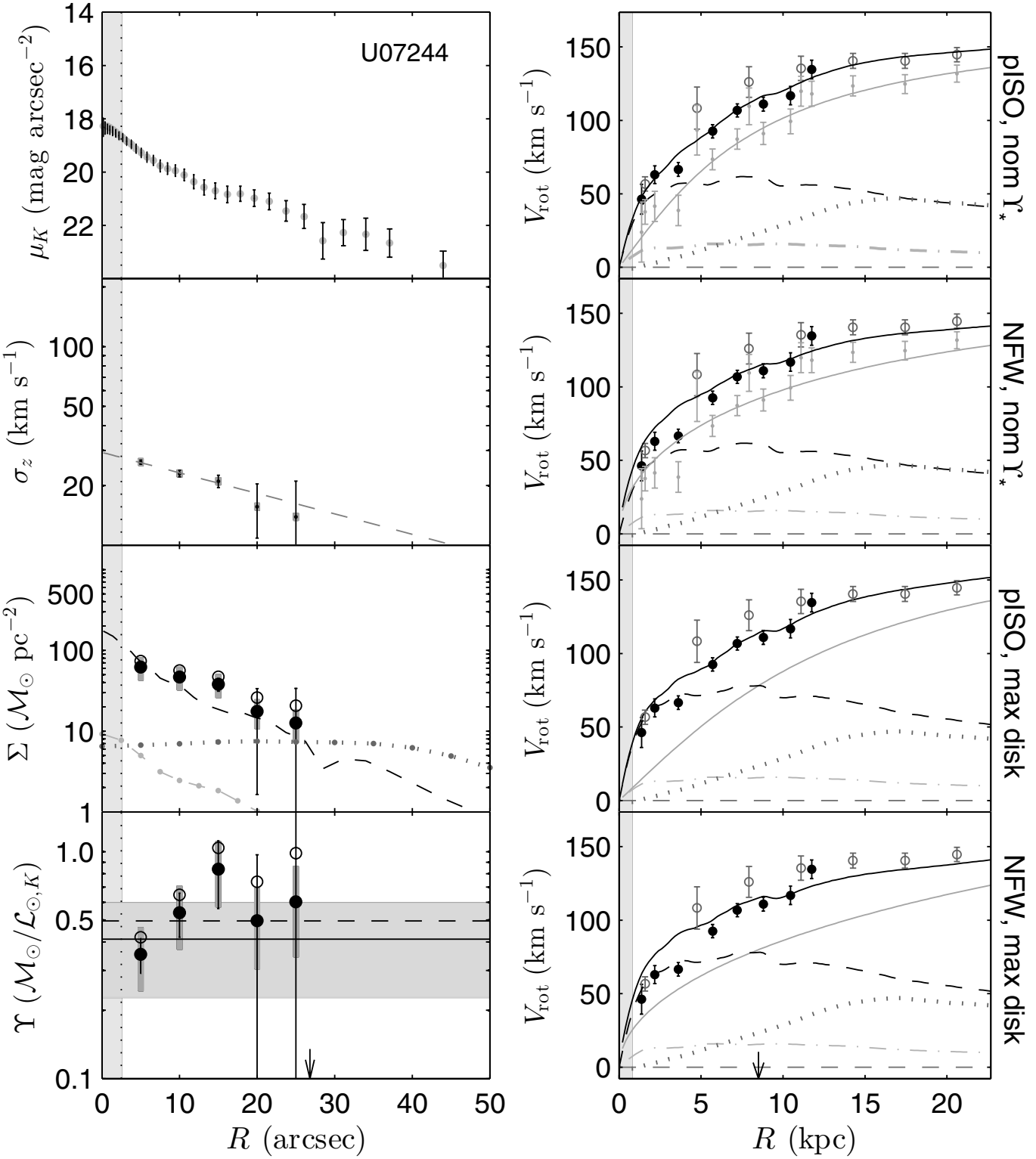
U07244
μ_K (mag arcsec^{-2})
σ_z (km s^{-1})
Σ ($\mathcal{M}_\odot$ pc^{-2})
Υ ($\mathcal{M}_\odot/\mathcal{L}_{\odot,K}$)
R (arcsec)
$V_{\rm rot}$ (km s^{-1})
pISO, nom Υ_*
NFW, nom Υ_*
pISO, max disk
NFW, max disk
R (kpc)

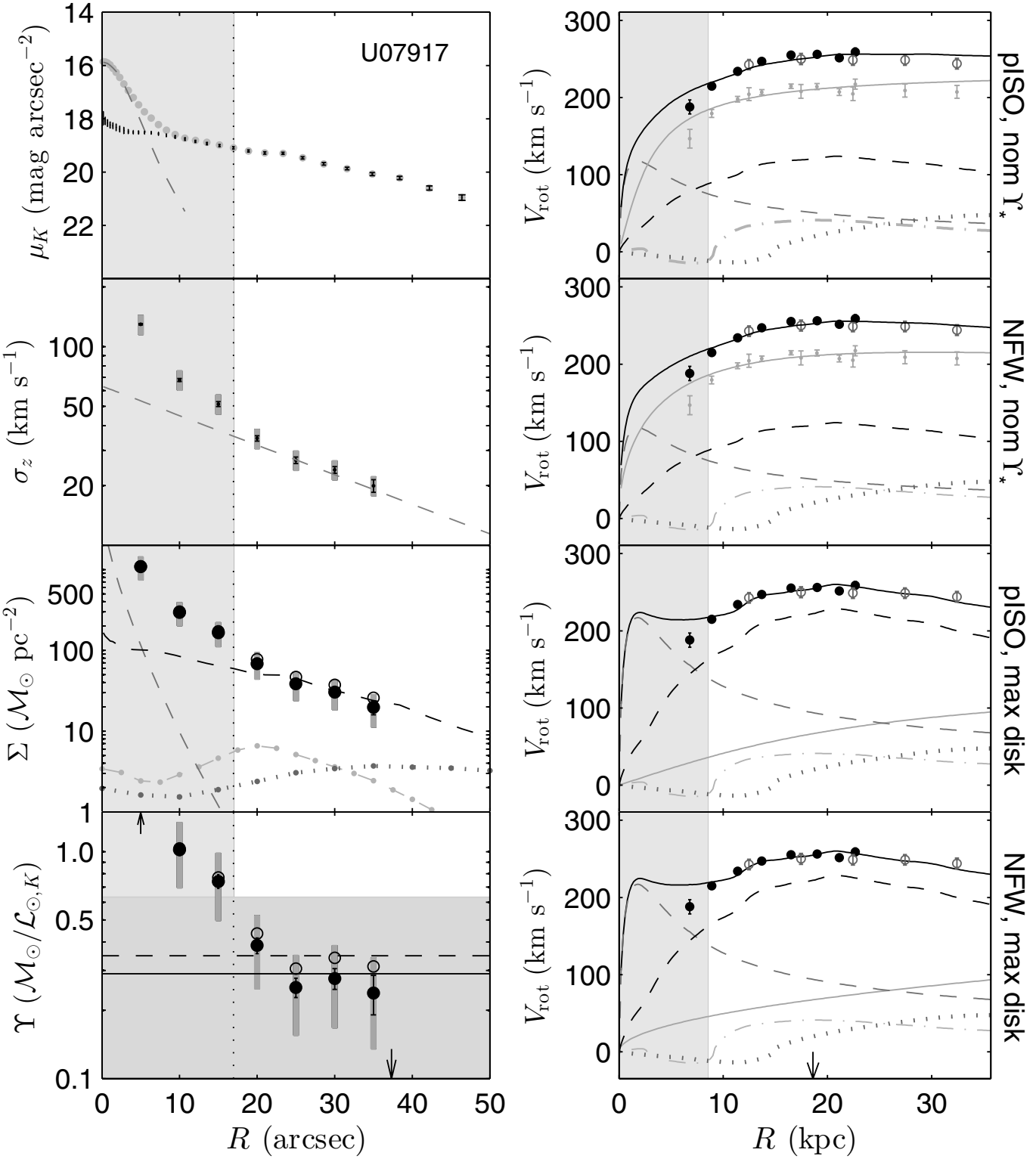
U07917
μ_K (mag arcsec^{-2})
σ_z (km s^{-1})
Σ ($\mathcal{M}_\odot$ pc^{-2})
Υ ($\mathcal{M}_\odot/\mathcal{L}_{\odot,K}$)
R (arcsec)
$V_{\rm rot}$ (km s^{-1})
pISO, nom Υ_*
NFW, nom Υ_*
pISO, max disk
NFW, max disk
R (kpc)

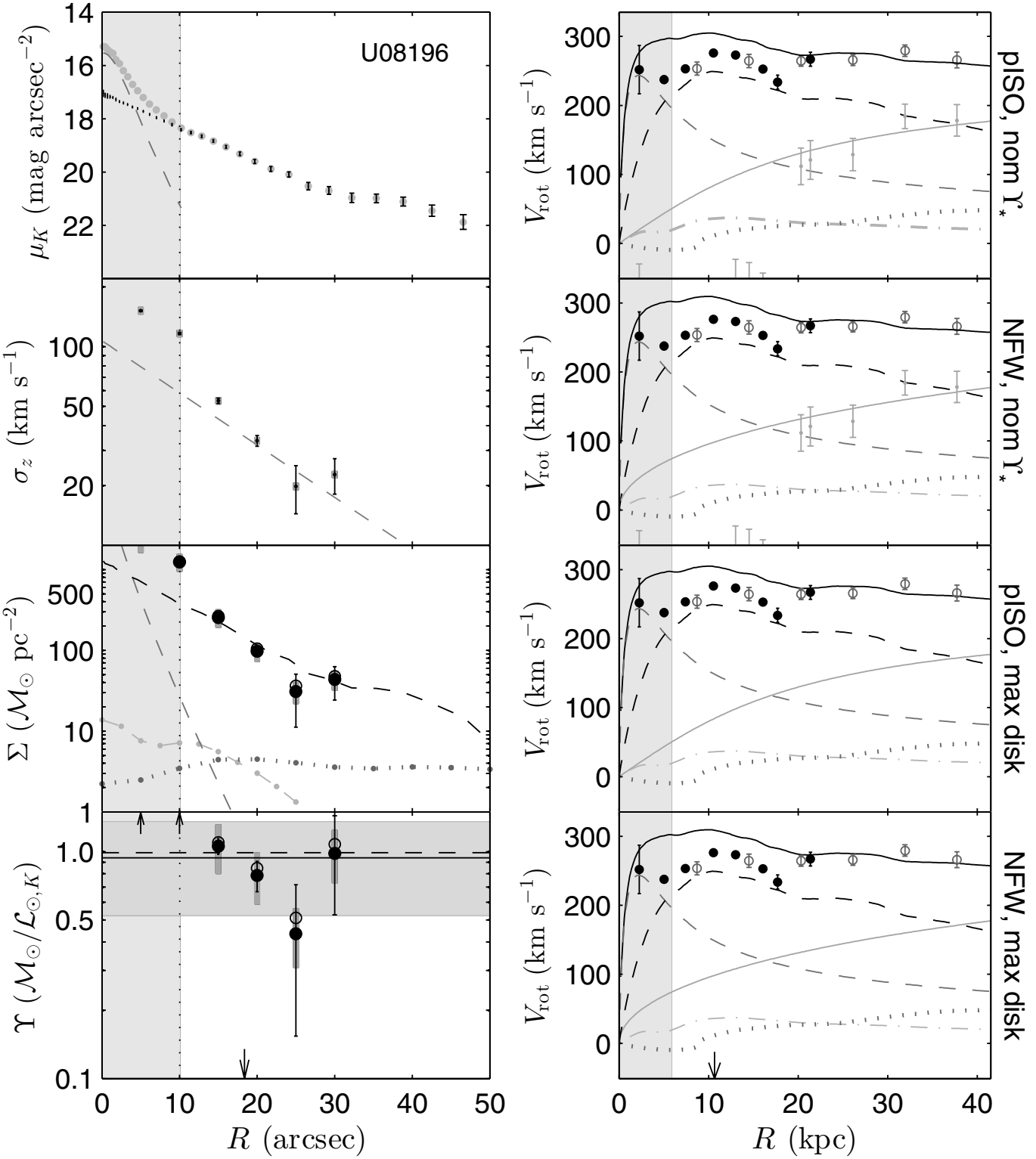
U08196
μ_K (mag arcsec^{-2})
σ_z (km s^{-1})
Σ ($\mathcal{M}_\odot$ pc^{-2})
Υ ($\mathcal{M}_\odot/\mathcal{L}_{\odot,K}$)
R (arcsec)
$V_{\rm rot}$ (km s^{-1})
pISO, nom Υ_*
NFW, nom Υ_*
pISO, max disk
NFW, max disk
R (kpc)

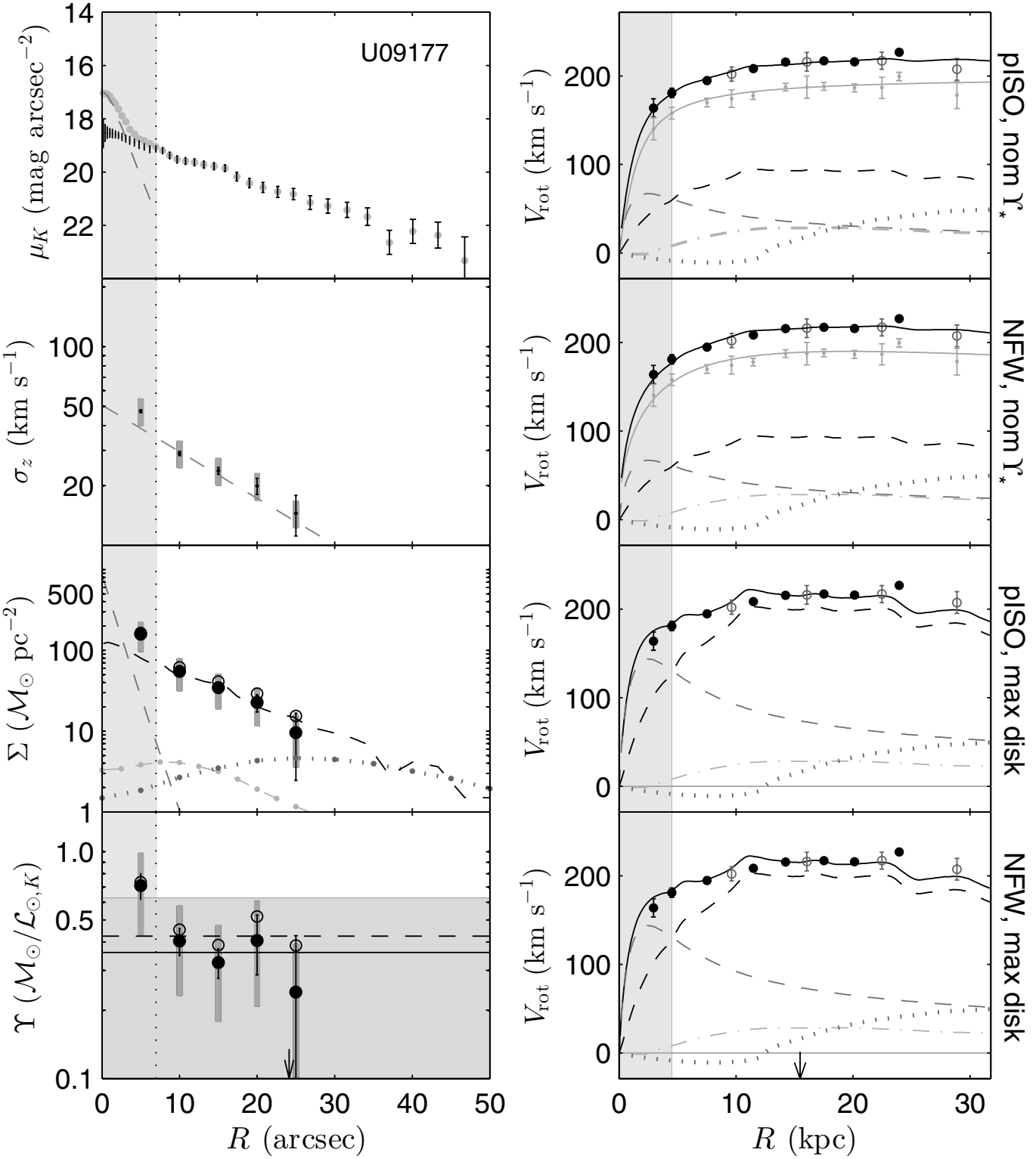
U09177
μ_K (mag arcsec^{-2})
σ_z (km s^{-1})
Σ ($\mathcal{M}_\odot$ pc^{-2})
Υ ($\mathcal{M}_\odot/\mathcal{L}_{\odot,K}$)
R (arcsec)
$V_{\rm rot}$ (km s^{-1})
R (kpc)
pISO, nom Υ_*
NFW, nom Υ_*
pISO, max disk
NFW, max disk

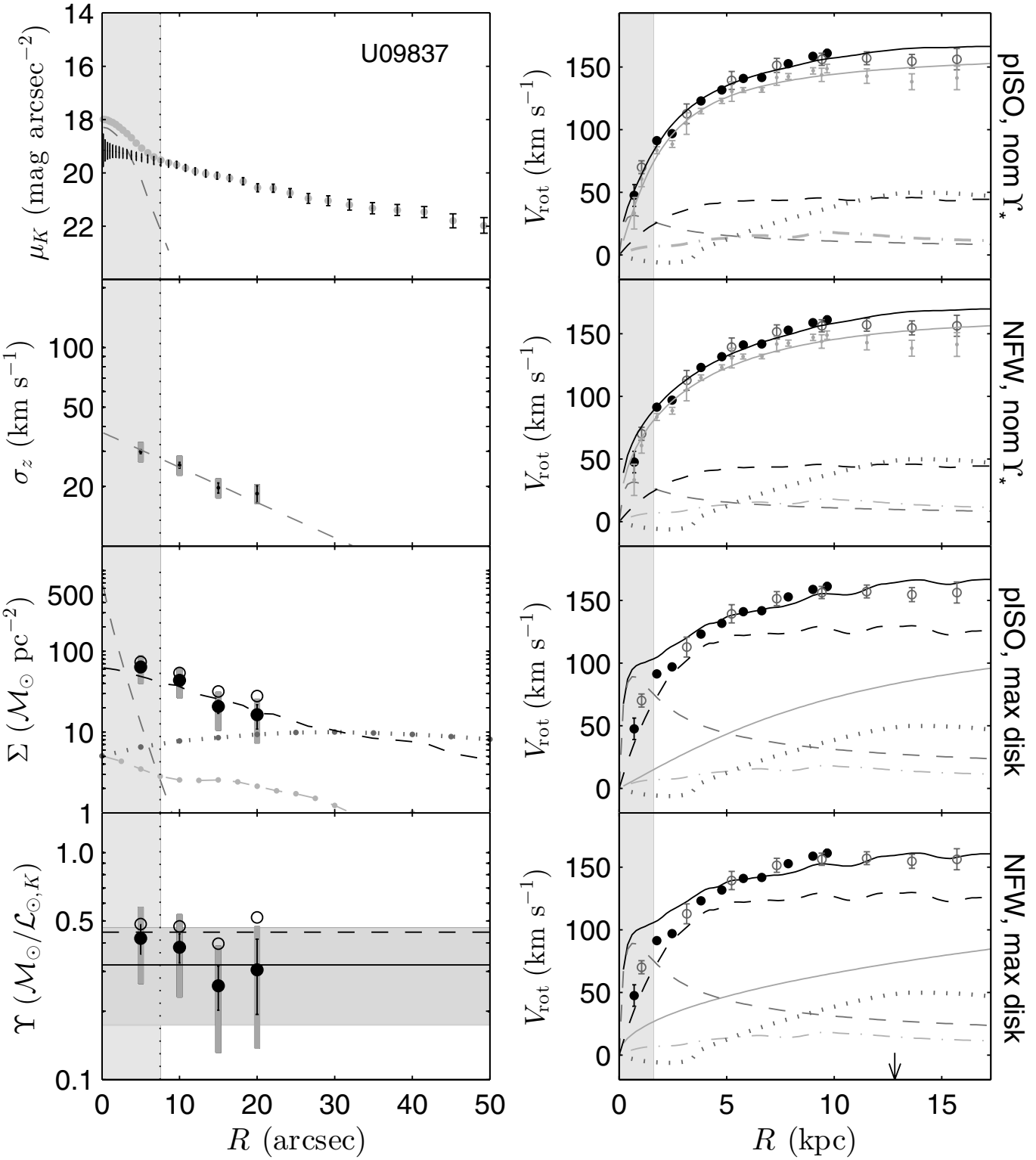
U09837
μ_K (mag arcsec^{-2})
σ_z (km s^{-1})
Σ ($\mathcal{M}_\odot$ pc^{-2})
Υ ($\mathcal{M}_\odot/\mathcal{L}_{\odot,K}$)
R (arcsec)
$V_{\rm rot}$ (km s^{-1})
pISO, nom Υ_*
NFW, nom Υ_*
pISO, max disk
NFW, max disk
R (kpc)

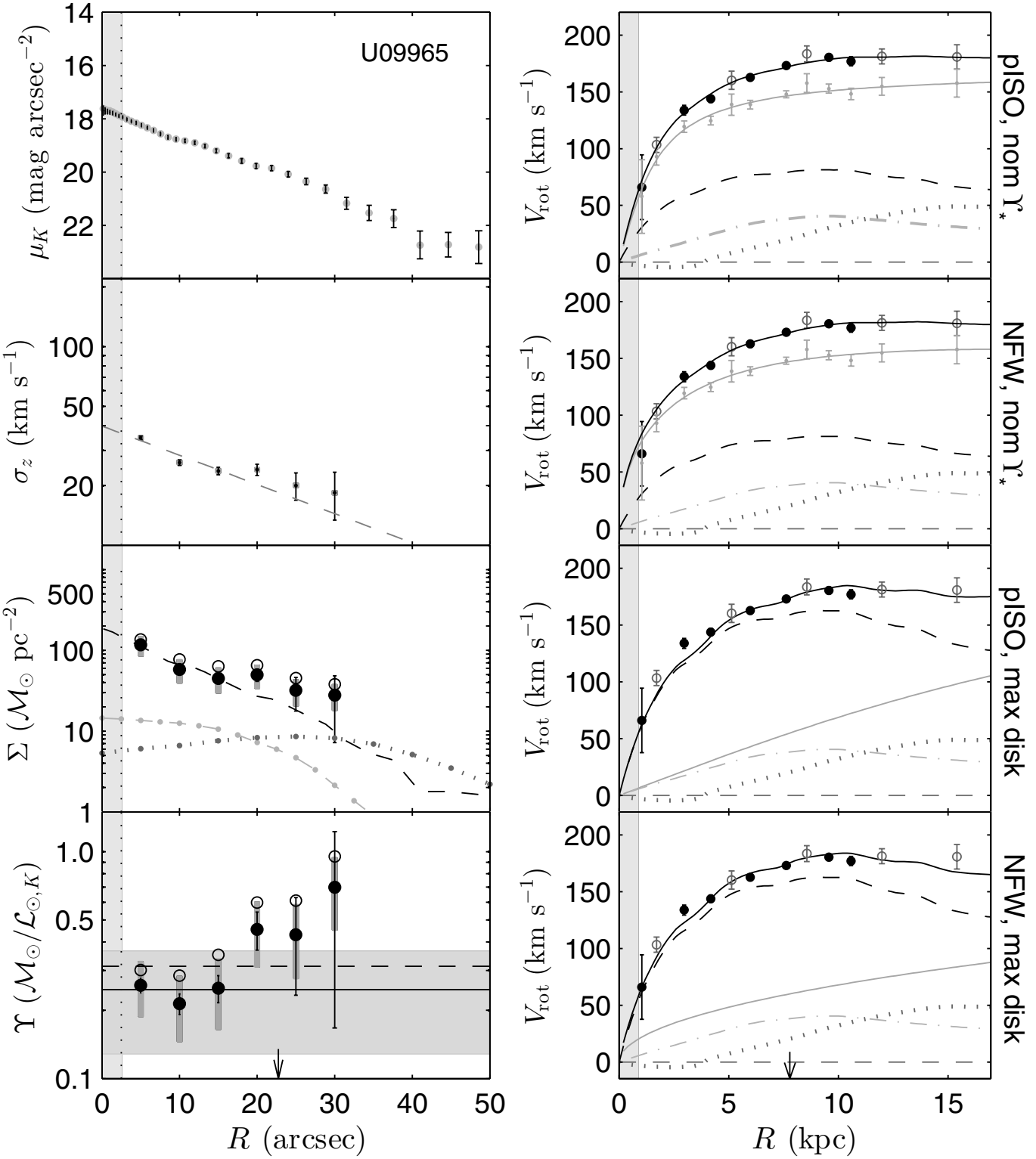
U09965
μ_K (mag arcsec^{-2})
σ_z (km s^{-1})
Σ ($\mathcal{M}_\odot$ pc^{-2})
Υ ($\mathcal{M}_\odot/\mathcal{L}_{\odot,K}$)
R (arcsec)
$V_{\rm rot}$ (km s^{-1})
R (kpc)
pISO, nom Υ_*
NFW, nom Υ_*
pISO, max disk
NFW, max disk

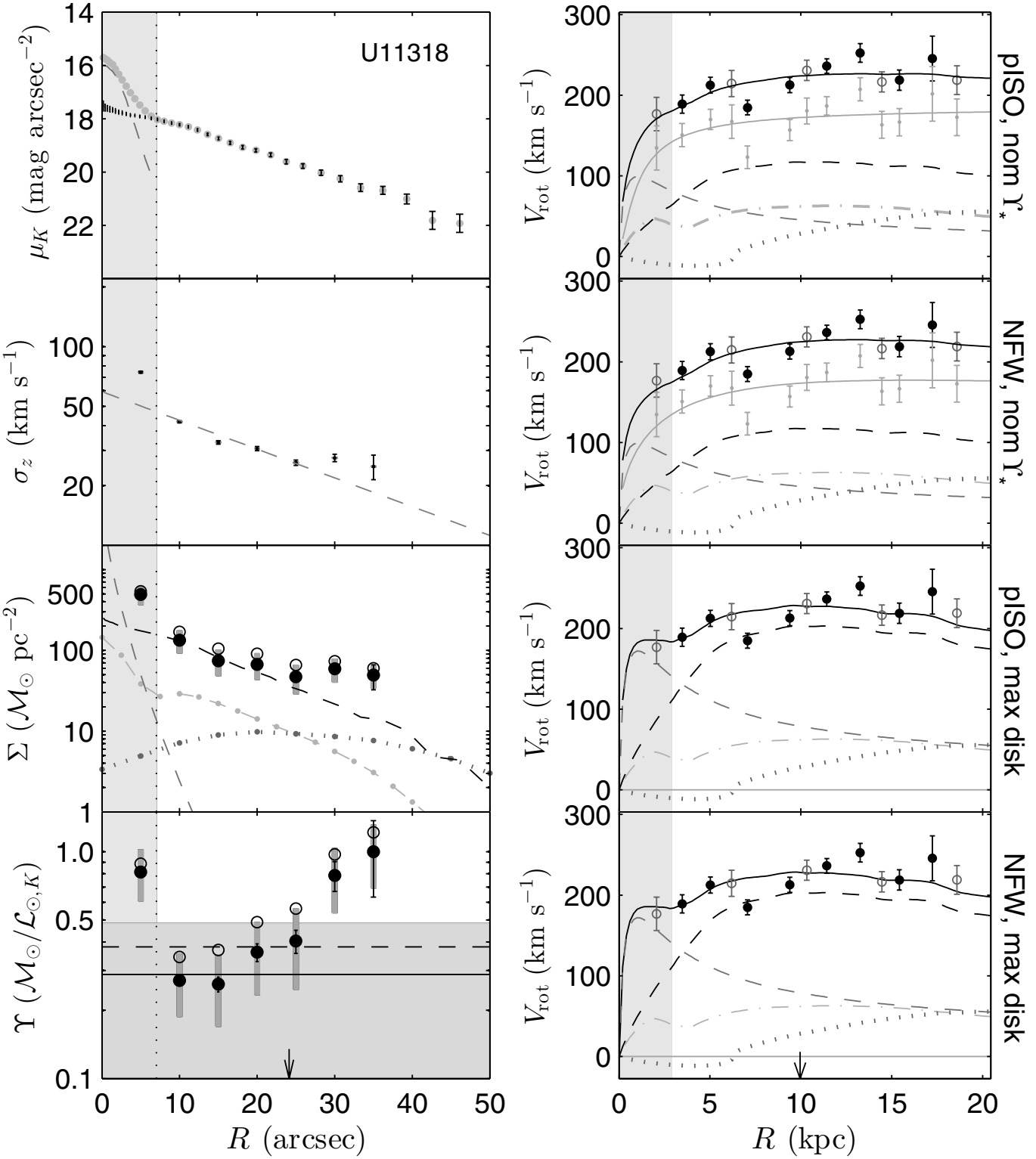
U11318
μ_K (mag arcsec^{-2})
σ_z (km s^{-1})
Σ ($\mathcal{M}_\odot$ pc^{-2})
Υ ($\mathcal{M}_\odot/\mathcal{L}_{\odot,K}$)
R (arcsec)
$V_{\rm rot}$ (km s^{-1})
pISO, nom Υ_*
NFW, nom Υ_*
pISO, max disk
NFW, max disk
R (kpc)

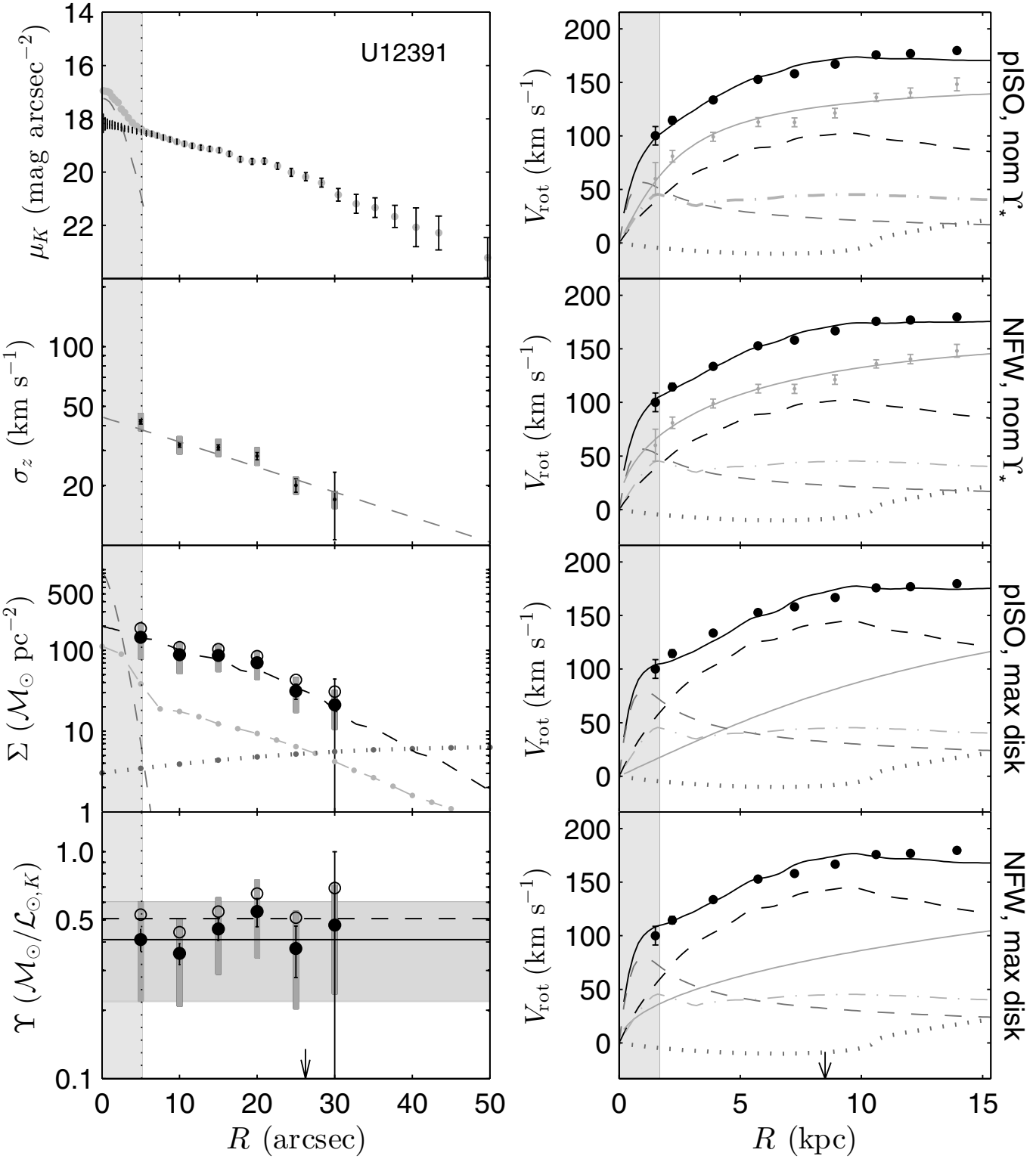
U12391
μ_K (mag arcsec^{-2})
σ_z (km s^{-1})
Σ ($\mathcal{M}_\odot$ pc^{-2})
Υ ($\mathcal{M}_\odot/\mathcal{L}_{\odot,K}$)
R (arcsec)
$V_{\rm rot}$ (km s^{-1})
pISO, nom Υ_*
NFW, nom Υ_*
pISO, max disk
NFW, max disk
R (kpc)